Montanuniversität Leoben

Doctoral Thesis

Investigation of interface properties of barrier metals on dielectric substrates

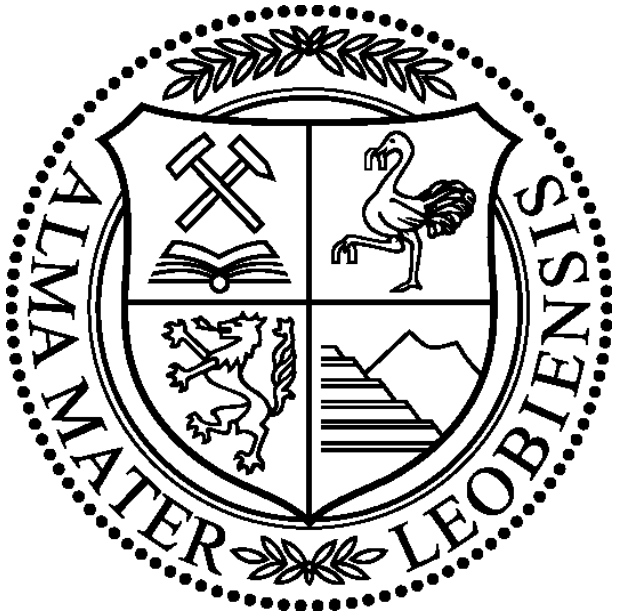

Bernhard Völker

Leoben, September 14

Part of this work was jointly funded by the Austrian Research Promotion Agency (FFG, Project No. 831163) and the Carinthian Economic Promotion Fund (KWF, contract KWF-1521|22741|34186).

KAI - Kompetenzzentrum Automobil- und Industrieelektronik GmbH
Technologiepark Villach
Europastrasse 8
9524 Villach
Austria
https://k-ai.at

Affidavit

I declare in lieu and oath, that I wrote this thesis and performed the associated research by myself, using only literature cited in this volume

Leoben, September 2014

Acknowledgement

First and foremost, I would like to thank Prof. Gerhard Dehm for giving me the opportunity to write this thesis and for the excellent scientific supervision.

Further I thank Dr. Walther Heinz, from KAI, for his support and supervision. Dr. Roman Roth, from Infineon Technologies AG, I like to thank for the encouragement of this work, all his support and discussions.

I also would like to express my gratitude to DI Josef Fugger and Mag. Elisabeth Regittnig at the KAI for all their support.
Additionally, I like to thank Dr. Thomas Detzel, Dr. Kurt Matoy, Dr. Jörg-Martin Batke and DI Thomas Fischer from Infineon Technologies AG, for all their support and interest in this work.
I am also grateful for the help of Prof. Christina Scheu and Dr. Sriram Venkatesan who were of tremendous help with the TEM measurements.
Dr. Thomas Schöberl, from ESI, I would like to thank for his help with the AFM measurements.

Furthermore, I wanted to acknowledge Dr. Megan Cordill and Prof. Reinhard Pippan, from the ESI, for their support, advice and the fruitful discussions about the topics on hand.
To all my colleagues and friends, I would like to say thank you for the good time and may there be more to come.

A special ”Thank you” I want to send to my office colleague Dr. Stefan Wurster, who endured me for the last couple of years, without showing any signs of resignation. He was a tremendous help and we had a lot of fruitful discussion.

Last but not least I would like to give all my gratitude to my family, my parents, Walter and Elfriede, and my little brother Andreas, without whom I would have never had the chance to be where I am today.

Abstract

In semiconductor devices interfaces play an important role. A typical interface occurring in semiconductor devices is the interface between dielectric and metal, which is necessary to guarantee the functionality of the device. Usually, the interface is between a metal or metal-based material, e.g. W, W(Ti) and TiN, and a silicate glass. The glass can be doped with different elements, e.g. boron and/or phosphorous. This type of interface is usually a rather weak one and prone to failure during service, because of the occurring thermo-mechanical stresses. It is important to understand the interfaces and compare the interfacial adhesion of different interfaces. Furthermore, it is necessary to test samples as close to the device size as possible.

In this study, the interfaces between different metallizations on as-deposited and annealed borophosphpsilicate glass (BPSG) were investigated. 4-point-bending (4PB) experiments were used to perform the mechanical characterization; Auger electron spectroscopy (AES) and atomic force microscopy (AFM) were applied to identify and characterize the fracture surface of the 4PB samples. Energy dispersive X-ray spectroscopy (EDX) in the transmission electron microscope (TEM) was employed to analyse the chemical composition of intact interfaces. Another method that was further developed to characterize the mechanical properties of the interfaces was an in-situ TEM submicron-sized bending beam approach.

The BPSG films revealed different mechanical behaviour after different process steps. The as-deposited BPSG showed a pronounced effect on the adhesion of W with 20 at% Ti (from here on W(Ti)) with and without a Ti interlayer. When the W(Ti) was directly applied on the as-deposited BPSG the evaluated interface energy release rate was half of the one which was achieved if a Ti interlayer was deposited in between the W(Ti) and the as-deposited BPSG. This difference, for the two systems with and without Ti interlayer, disappeared, when annealed BPSG is used, instead of the as-deposited one. There the Ti interlayer did not have any further beneficial effect. The variation of the Ti content between 15 to 25 at% in the W layer showed no pronounced effect on the adhesion of W(Ti) on annealed BPSG. All studied cases of different Ti contents in the W(Ti) layer gave almost the same interface energy release rate, which was the same as for a pure Ti layer on annealed BPSG. It was also possible to reveal that the Ti incorporated in the W layer promoted the adhesion significantly compared to a pure W layer on annealed BPSG. The EDX measurements in the TEM on an intact interface indicated a Ti enrichment at the interface between W(Ti) and annealed BPSG. The main reason for this finding is a 400 °C anneal at the end of the sample production. The AES and AFM investigations of the fracture surface of the 4PB samples revealed Ti residues on the

BPSG fracture surfaces of all material systems containing Ti. These residues seem to be Ti-based particles which were ripped out of the metallization side of the interface of interest.

The chosen interfaces to investigate the influence of the sample size on interfacial adhesion were Cu and W(Ti) on annealed BPSG, respectively. For the Cu/BPSG interface the 4PB experiments indicated a weaker interface than for the W(Ti)/BPSG. In-situ 4PB experiments in the scanning electron microscope (SEM) at the Cu/BPSG system enabled the identification of the failing interface without using any additional methods, like AES, on the fracture surfaces of the 4PB samples. In addition, in-situ TEM micro-bending beam experiments showed, taking the difference in sample dimension into account, good agreement with the macroscopic 4PB tests, for the Cu/BPSG system. In case of the W(Ti)/BPSG samples the interface was too strong to be tested with the proposed in-situ TEM bending beam setup.

This study shed some light on selected interfaces between metals and BPSG. Furthermore, it was revealed that it is possible to compare the results of different methods over several length scales. This provides the possibility to test semiconductor structures nearer to the device size and it will be possible to combine very localized chemical and mechanical information of the interface.

Zusammenfassung

In Halbleiterbauteilen erfüllen Grenzflächen eine wichtige Rolle. Eine wichtige Art von Grenzfläche, die in solchen Bauteilen auftritt, ist jene zwischen Dielektrikum, z.B. ein Glas auf Silikat-Basis, und Metallen bzw. Materialien auf Metall-Basis, z.B. W, W(Ti) und TiN. Bei dem Glas kann es sich auch um ein dotiertes Glas handeln, welches z.B. mit Bor oder Phosphor dotiert wird um die gewünschten Eigenschaften einzustellen. Die Grenzfläche zwischen Metallen und Glas ist deswegen von großer Bedeutung, da sie die Funktionalität des Bauteils sicherstellt.

Im Betrieb des Bauteils wird oft beobachtet, dass die oben genannte Grenzfläche versagt. Der Grund dafür sind die auftretenden thermo-mechanischen Spannungen. Deshalb ist es notwendig die Haftung und den Aufbau solcher Grenzflächen zu verstehen, um mögliche Verbesserungen vorzunehmen. Des Weiteren ist es auch notwendig die Grenzfläche so nahe wie möglich an der eigentlichen Größe wie sie im Bauteil auftritt zu testen.

In dieser Arbeit wurden Grenzflächen zwischen verschiedenen Metallen und geglühtem und nicht geglühtem Bor-Phosphor dotiertem Glas (BPSG) untersucht. Die mechanische Charakterisierung erfolgte mittels der 4-Punkt-Biege (4PB) Methode, die Bruchflächen der 4PB Proben wurden mit Augerelektronenspektroskopie (AES) und Rasterkraftmikroskopie (AFM) untersucht. Intakte Grenzflächen wurden hinsichtlich ihrer chemischen Zusammensetzung mittels energiedispersiver Röntgenspektroskopie (EDX) im Transmissionselektronenmikroskop (TEM) untersucht worden.

Der Herstellungszustand des BPSG zeigt einen großen Einfluss auf die Haftung von W, welches mit 20 at% Ti dotiert wurde (danach als W(Ti) bezeichnet) mit und ohne einer Ti Zwischenschicht. Auf nicht geglühtem BPSG zeigt die Ti-Zwischenschicht eine deutliche Verbesserung der Haftung. Die Energiefreisetzungsrate liegt fast doppelt so hoch als im Vergleich zu W(Ti) direkt auf BPSG. Wenn jedoch geglühtes BPSG verwendet wird, hat die Ti-Zwischenschicht keinerlei Einfluss auf die Haftung von W(Ti).

Wird der Ti-Gehalt im W zwischen 15-25 at% variiert, zeigt diese Variation keinen Einfluss auf die Haftung von W(Ti) auf geglühtem BPSG. Vergleicht man die Haftung der verschiedenen W(Ti)-Schichten mit jener von reinem Ti auf geglühtem BPSG, so zeigt sich, dass alle dieselbe Grenzflächenhaftung besitzen. Hingegen verbessert das Ti in der W-Schicht die Haftung im Vergleich zu einer reinen W-Schicht deutlich. In der Untersuchung einer intakten Grenzfläche konnte gezeigt werden, dass sich Ti an der Grenzfläche zwischen W(Ti) und BPSG anreichert. Der Hauptgrund für diese Anreicherung scheint eine Wärmebehandlung bei 400 °C am Ende der Probenpräparation zu sein.

Die an den Bruchflächen der 4PB Proben durchgeführten AES und AFM Messungen zeigten für alle Metallschichten, welche Ti enthielten, Ti Reste auf der BPSG Seite der Bruchfläche. Diese Ti-Reste scheinen von Partikeln auf Ti-Basis zu kommen, welche aus der Bruchfläche des Metalls heraus gerissen wurden und auf der BPSG-Seite haften blieben.

Der Einfluss der Probengröße auf die Haftung wurde an den Grenzflächen von Cu und W(Ti) auf geglühtem BPSG, durchgeführt. Hierzu wurden makroskopische 4PB Experimente durchgeführt. Diese zeigten eine schwächere Grenzfläche für das Cu-System, als für das W(Ti)-System. Zusätzliche in-situ 4PB Versuche an Cu/BPSG im SEM ermöglichten die Identifikation der versagenden Grenzfläche ohne zusätzliche Untersuchung der 4PB Bruchflächen nach dem Versuch, durch Methoden wie AES. Um die Grenzflächen im mikroskopischen Maßstab zu testen, wurden in-situ TEM Biegebalken hergestellt. Diese zeigten, unter Berücksichtigung der unterschiedlichen Probengeometrien, eine gute Übereinstimmung zu den 4PB Ergebnissen für das Cu/BPSG System. Es wurde auch versucht die Biegebalkenversuche an dem System W(Ti)/BPSG durchzuführen. Die Grenzfläche dieses Systems scheint jedoch zu stark für einen erfolgreichen Einsatz des verwendeten Versuchsaufbau zu sein.

Es war möglich die Grenzflächen zwischen verschiedenen Metallen und BPSG genauer zu charakterisieren und es konnte gezeigt werden, dass die Resultate von makroskopischen und mikroskopischen Experimenten unter gewissen Randbedingungen verglichen werden können. Dies ermöglicht es Halbleiterbauelemente nahe an der eigentlichen Strukturgröße zu testen und die Resultate können mit anderen makroskopischen Experimenten verglichen werden. Dies ermöglicht die Kombination von lokalen mechanischen und chemischen Eigenschaften der Grenzfläche.

"Do, or do not. There is no try."

Yoda, The Empire Strikes Back (1980)

Table of Contents

1. Introduction

Interfaces play an important role in a number of applications, such as protective coatings, fibre-reinforced composites, semiconductor devices, just to name a few examples. In semiconductor devices, interfaces are necessary to guarantee the functionality of the device. A number of different interfaces occur in semiconductor devices, for instance between metal-metal, metal-semiconductor, semiconductor-dielectric or dielectric-metal and often occur between conducting layers, like Cu or Al, and insulating dielectrics or as interface between diffusion barriers, like W, W(Ti) or TiN, and the dielectric layer. The dielectric is in most cases a silicate based glass. The interfaces between metal and dielectric have been reported in different studies [1–9]. It is frequently observed that the metal-dielectric interface is weak. During device production or operation, failure is often observed at such interfaces. That is the reason why it is essential to understand the fracture behaviour of these interfaces and how to improve the interfacial adhesion.

To increase the strength of the metal-dielectric interface different approaches have been suggested in literature: Russel et al. [10] suggested to introduce alloying additions such as Ti or Cr into Cu films to improve the metal-dielectric interface strength. It is also possible to use adhesion promoting interlayers [6,10–14]. Another possibility to enhance interfacial adhesion is ion-beam irradiation [15–20]

There are many different methods to experimentally determine the interfacial adhesion [3,6,21–31]. Depending on which method is used, different restrictions have to be followed and different results can be obtained. For instance, some methods can only give qualitative values, others only work for bi-layered material systems, while another group of testing techniques enables to determine quantitatively interface energy release rates of multilayer systems. Thus, it is necessary to know the interface of interest and the materials which are included, to choose the proper experimental method to get a satisfying result.

The 4-point-bending (4PB) technique according to Ma et al. [3], described in more detail in the subsequent sections, belongs to the quantitative approach for a mechanical characterization of interfaces. Amongst others are nanoindentation with and without superlayer [24–26], double cantilever beam [28,29] and micro-bending beams [30,31] which are also able to test multilayer systems and return an interface energy release rate. A comprehensive summary and description of the most common methods, their advantages, disadvantages and application for interface fracture experiments is given in Volinsky et al. [5] and Chen & Bull [32].

1.1. Fracture Mechanics Introduction

Here, a short introduction into linear elastic fracture mechanics will be given. Elastic-plastic fracture mechanics will not be discussed in detail. For further reading into the topic following literature is suggested [33–36].

1.1.1. Linear Elastic Fracture Mechanic

The first attempt to describe fracture dominated failure was the energy approach suggested by Griffith in 1920 [37]. He introduced an approach which states that a crack propagates in a sample if the total elastic energy of the system is lowered. This holds true for brittle materials, like glasses, for which Griffith developed his solution. Some years later, Irwin showed that the approach developed by Griffith is valid as long as there is no significant plastic deformation in the material. Irwin altered the Griffith approach by incorporating the energy contribution of plastic deformation [38]. In addition, Irwin found that for ductile materials the formation of new crack surfaces can be neglected compared to the large contribution of plastic deformation.

The stress intensity approach was also developed by Irwin, which states that when a critical stress concentration at the tip of the crack is surpassed, fracture occurs. This is termed the critical stress intensity factor K_C or in energy terms the critical energy release rate G_C. Later it was possible to show that for linear elastic fracture mechanics, G_C and K_C are equivalent.

This equivalent is derived in the example of an infinite plate with a through thickness crack in the centre under constant displacement conditions, with a crack length of $2a$, see Figure 1.

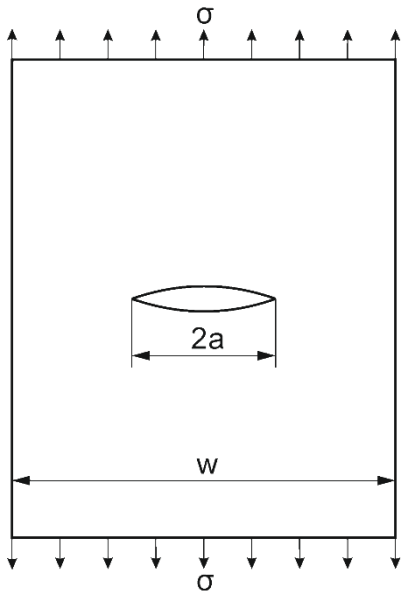

Figure 1 *Depiction of a plate with a centre crack of the length 2a under constant displacement conditions. The width of the plate has to be much larger than the crack length 2a (w>>2a). After [34].*

Equation 1 gives the Griffith energy approach. There are two main energy contributions to the total energy U of the plate, the internal and external contributions. The internal energy contributions are the elastic energy of the plate without the crack, U_e, the change in elastic energy due to the introduction of the crack, U_a, and U_s representing the change in elastic energy due to the formation of new crack surface. The external contribution is the work, W, performed on the system. This contribution has to be subtracted from all the internal energies listed above.

$$U = U_e + U_a + U_s - W \quad \textit{(Eq. 1)}$$

The energy contributions of U_a and U_s can be calculated the following way.

$$|U_a| = \frac{\pi\sigma^2 a^2}{E} \quad \textit{(Eq. 2)}$$

$$U_s = 4a\gamma_e \quad \textit{(Eq. 3)}$$

To be able to calculate U_a one has to know the stress, σ, the crack length, a, and the Young's modulus, E, of the material, see Equation 2. For U_s, as seen in Equation 3, additionally the energy necessary to form new crack surface, γ_e, has to be known.

As mentioned earlier, the constant displacement condition was chosen so the work *W=const.*. In this case U_a, the change of elastic energy because of the crack initiation, has to be subtracted. The reason for that is the decreasing of the elastic energy of the plate because of the crack. This leads to the form of the Griffith approach, as seen in Equation 4.

$$U = U_e - \frac{\pi\sigma^2 a^2}{E} + 4a\gamma_e - W \qquad \textit{(Eq. 4)}$$

Here, the elastic energy U of a plate with a centre crack of the length $2a$ is shown. It is considered that the initial energy of the plate U_e is constant. This means that the change in elastic energy for infinitesimal crack growth can be neglected ($dU_e/da=0$) and the change of the external work is zero, because of the constant displacement condition ($dW/da=0$). To find the equilibrium condition for crack propagation dU/da has to be set to zero and gives the equilibrium condition shown in the form of Equation 5.

$$\frac{\pi\sigma^2 a}{E} = 2\gamma_e = R \qquad \textit{(Eq. 5)}$$

The result of Equation 5 is the crack resistance R, which is the energy necessary to form two new crack surfaces. If a critical value of this crack resistance is surpassed fracture occurs. This critical value is called G_C, the critical energy release rate, which is necessary to extend the crack. Accordingly, it can be said that if the left hand side of Equation 5 is equal to or is exceeding G_C the sample fractures. In Equation 6 the fracture criterion according to Griffith is given. All parameters which are material dependent are on the right hand side. It can be assumed that they represent a material constant,

$$\pi\sigma^2 a \geq G_C E \qquad \textit{(Eq. 6)}$$

Irwin further suggested a stress concentration approach for the crack tip as seen in Equation 7

$$K = \sigma\sqrt{a\pi} f(a/w) \qquad \textit{(Eq. 7)}$$

Where K is the stress intensity factor, σ the applied stress, a the crack length and $f(a/W)$ a geometry form factor. For simplicity the form factor equals *1*, but it can differ significantly

depending on the geometry of the specimen. Geometry form factors for a wide range of specimen shapes and loading conditions can be found in literature [39,40]. It is obvious that for linear elastic behaviour of the sample, the left hand side of Equation 6 and the right hand side of Equation 7 are the similar and it follows that

$$K = \sqrt{GE}. \quad \textit{(Eq. 8)}$$

Equation 8 implies, if there is a critical energy release rate G_C for fracture, there also has to be a critical stress intensity factor K_C. Including the two main loading cases, namely plane stress and plane strain, this links the critical stress intensity and the critical energy release rate for the linear elastic case,

$$G_C = \frac{K_C^2}{E} \quad \text{(plane stress)} \quad \textit{(Eq. 9)}$$

$$G_C = \frac{K_C^2}{E}(1 - \nu^2) \quad \text{(plane strain)} \quad \textit{(Eq. 10)}$$

All the aforementioned relations are valid for mode I loading, when the load is applied perpendicular to the fracture surfaces (see Figure 2). There are three different modes of loading. As already mentioned, mode I corresponds to crack extension perpendicular to the loading direction and perpendicular to the crack plane (opening). Mode II is in direction of the crack extension (shear) and mode III corresponds to loading of the sample perpendicular to the crack extension and parallel to the crack plane (twist). In Figure 2 the three loading cases are depicted.

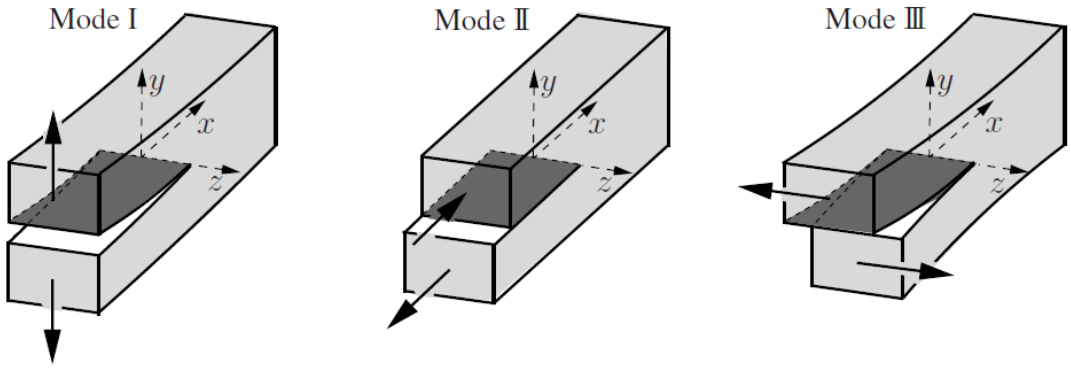

Figure 2 *Sketch of the different crack opening modes (mode I, II and III). Taken from [36].*

The derived relations lead to the following criterion for sample failure.

$$K \geq K_{IC} \qquad \textit{(Eq. 11)}$$

In most engineering materials there is plastic deformation (plastic zone) ahead of the crack tip. The size and shape of this plastic zone is dependent on the loading case, mode I, II or III, and the material, see Figure 3. For ductile materials a large plastic zone develops and for brittle material a small plastic zone is generated. The plastic zone size is also a criterion which has to be considered when determining if linear elastic fracture mechanics can be applied to a situation. To be allowed to use the linear elastic approach the size of this plastic zone has to be small compared to the sample dimensions. In addition, it can be said that for plane strain condition the plastic zone size is smaller than in plane stress. In Figure 3b it can be seen that in the centre of the sample of sufficient thickness there is a plane strain case, the plastic zone size is small and the closer one gets to the sample surface the larger the plastic zone gets, because the loading is changing from plane strain to plane stress at the surface. This is the reason why thicker samples are preferred for fracture mechanic investigations to guarantee a plane strain dominated behaviour.

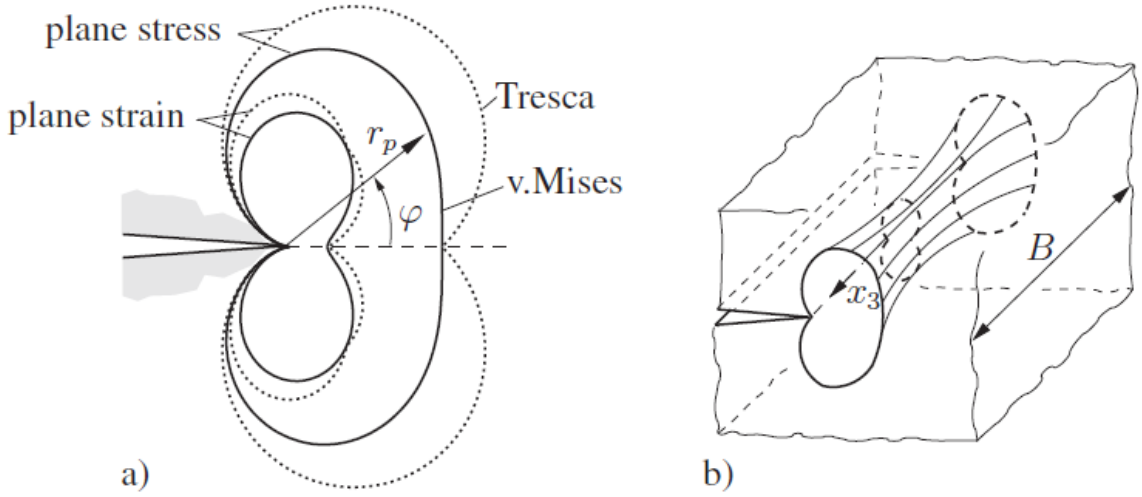

Figure 3 *Plastic zone ahead of the crack tip for a mode I crack. a) depicts the comparison of plane strain and plane stress case. In b) the plastic zone in front of the crack tip along the width of the sample is depicted. It can be clearly seen that the size of the plastic zone increases the closer one gets to the edge of the sample (plane stress case).From [36].*

When the plastic zone size is large compared to the sample, linear elastic fracture mechanics can no longer be applied and elastic-plastic fracture mechanics has to be used.
Irwin extended the approach by Griffith to include plastic deformation, seen in Equation 12.

$$\pi\sigma^2 a = 2E(\gamma_e + \gamma_p) \qquad \textit{(Eq. 12)}$$

For ductile materials $\gamma_p >> \gamma_e$, so the energy necessary for new crack surface formation γ_e is negligible compared to the contribution of plastic deformation γ_p. This extension of Griffith's fracture criterion by Irwin set the starting point for elastic-plastic fracture mechanics.
Elastic-plastic fracture mechanics deals with the investigation of materials with large plastic zones, but it cannot deal with samples that fail because of plastic collapse. Two methods are used in elastic-plastic fracture mechanics to investigate the fracture behaviour. One method is the crack tip opening displacement (COD) and the other is the J-integral. The COD approach uses the measurement of the displacement of the crack flanks in the vicinity of the tip. This displacement is a representative for the stress at the crack tip. If now the stress at the crack tip reaches a certain plastic limit, a certain critical value of the COD is surpassed, which induces crack growth. So this method is used to determine the onset of crack growth.
The J-integral approach is an energy approach, similar to the Griffith approach shown in Equation 1, but with the J-integral, it is possible to evaluate non-linear behaviour. The main assumption is that during loading, no unloading of any part of the sample occurs. Therein lies also the limitation of this method. At the onset of crack growth unloading of the newly formed

crack flanks occurs and the J-integral solution is no longer valid. This concludes that the J-integral solution for elastic-plastic fracture mechanics can only be used until the onset of crack growth.

1.1.2. Interface Fracture Mechanics

There have been many theoretical investigations of interface fracture [41–47]. About how the crack kinks onto the interface [42], under which circumstances the crack stays at the interface and when does it kink onto the adjacent material layer [43]. Furthermore, how interfaces can be tested, different loading schemes and possible sample geometries, and how the interface strengths for different loading cases can be determined is discussed in Hutchinson and Suo [46].

An important issue in determining the interface energy release rate is the mode mixity factor ψ, which gives the relation between mode I and II. In Figure 4 the graph shows how mode II increases with ψ.

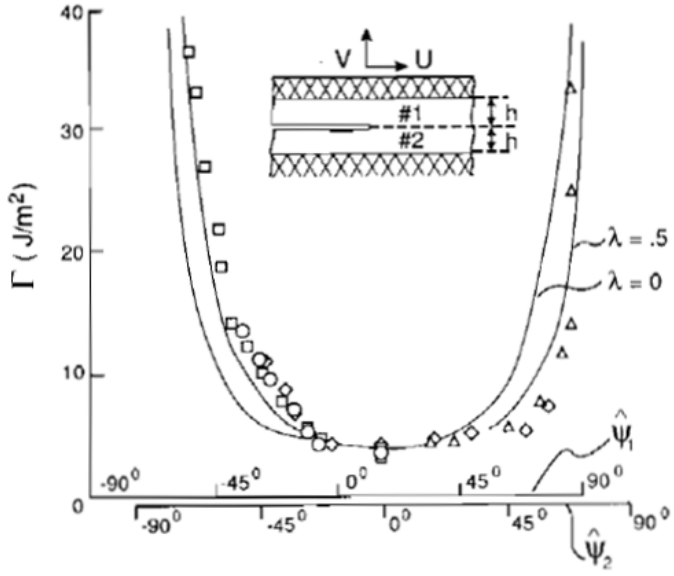

Figure 4 *Diagram of the dependence of the work of adhesion Γ on the mode mixity ψ [46,48,49]. Taken from [46].*

This mode mixity also influences the measured interface energy release rate. Usually in pure mode I loading (0°) the lowest interface energy release rate is measured and in pure mode II (90°) the highest, see Figure 4. This means that for a mixed mode fracture, like most of the interface testing techniques have, a value in between those two cases is measured for the interface energy release rate.

Another important issue for calculating an interface energy release rate is that the crack has to kink onto an interface. There are certain requirements that have to be met in order for the crack to kink onto the interface as shown by He and Hutchinson [42]. They revealed that the difference of the elastic mismatch in a bi-layered material system influences the possibility for the crack to kink onto the interface and propagate along it. This relation is shown in Figure 5. The ratio between the interface fracture energy and the energy necessary to fracture the adjacent material layer is drawn over α, the first Dundurs' parameter (see Equation 13), for $\beta=0$, the second Dundurs' parameter.

$$\alpha = [\mu_1(1-\nu_{2)} - \mu_2(1-\nu_1)]/[\mu_1(1-\nu_2) + \mu_2(1-\nu_1)] \qquad \textit{(Eq. 13)}$$

The indices *1* and *2* indicate the two adjacent material layers at the interface, μ, denotes the shear modulus and *v,* the Poison's ratio of the corresponding material.

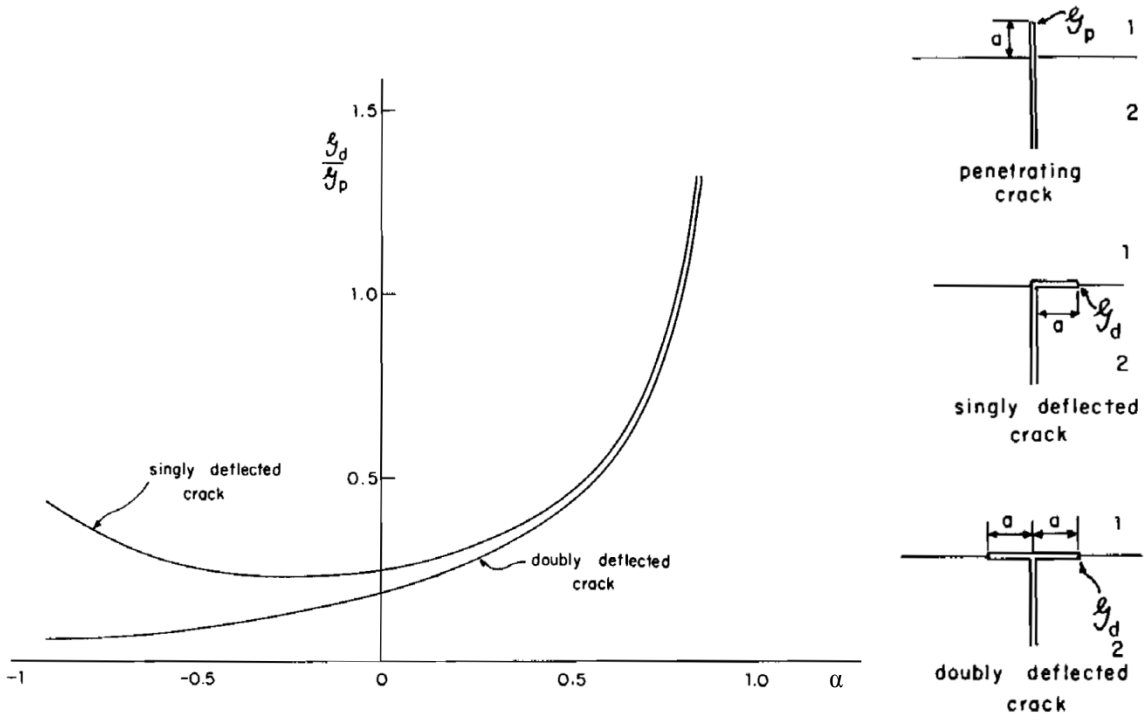

Figure 5 *Diagram of the ratio between interface energy release rate to the energy necessary to fracture the adjacent layer over α (first Dundurs' parameter) for the same crack extension a and β=0 (second Dundurs' parameter). Taken from [42].*

He and Hutchinson [42] showed in their study that for a bi-layered material system without any significant elastic mismatch, that the crack kinks onto the interface, if the energy

necessary for the crack to propagate along the interface is ¼ or less compared to the fracture energy of the film.

There are a lot of different methods for practical interface testing, for instance, nanoindentation with and without superlayer [6,24–27]. It has the advantage that it is a very quick method and a lot of indents can be performed in a short time. But to be evaluable there has to form a blister and it can be difficult to measure the actual size of the blister. Another method is the superlayer test [23], were the interface is failing because of the addition of a superlayer, which has compressive stress. Here it can be a very time consuming process to find the right thickness of the superlayer, which material should be used for it and the measurement of the peeling parameters which are necessary to evaluate the interface energy release rate can also be tricky. There is also the possibility of the 4-point-bending (4PB) method [3,22,50]. It proved to be useful for metal-dielectric interfaces. Furthermore, the sample production and experimental setup is simple. Certain difficulties with this method are that experimental measurements are time consuming, because of low loading rates, and the output of successful samples. The 4PB method was developed for testing bi-layer material systems by Charalambides et al. [22], see Figure 6.

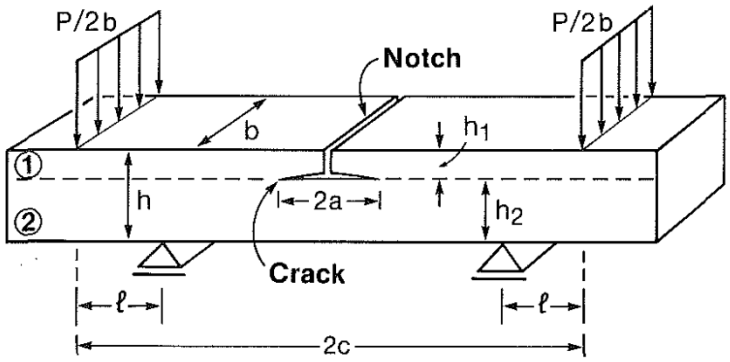

Figure 6 *Sketch of a 4PB experiment with the sample geometry for a bi-layered material system where the upper layer is thinner than the lower material. From [22].*

They showed that with this method it is possible to determine an interface energy release rate G_i for a material system the following way:

$$G_i = \frac{M^2(1-\nu_2^2)}{2E_2}\left(\frac{1}{I_2} - \frac{\lambda}{I_C}\right) \quad \text{with} \quad M = \frac{Pl}{2b} \;\; \& \;\; \lambda = \frac{E_2(1-\nu_1^2)}{E_1(1-\nu_2^2)} \qquad \textit{(Eq. 14)}$$

$$I_C = \frac{h_1^3}{12} + \frac{\lambda h_2^3}{12} + \frac{\lambda h_1 h_2 (h_1+h_2)^2}{4(h_1+\lambda h_2)} \qquad \textit{(Eq. 15)}$$

$$I_2 = \frac{h_2^3}{12}. \qquad \textit{(Eq. 16)}$$

In Equations 14-16 the indices *1* denotes the upper material (notched part), *2* the lower material (unnotched) and *C* the composite beam. *M* represents the bending moment normalized on the sample width *b*, *P* is the load at the load plateau in the load displacement curve (see Figure 8), *l* the distance between inner and outer loading pins (see Figure 6), *E* denotes the Young's modulus and *v* the Poison's ratio. The second moment of area *I* is also normalized to the sample width. In Equation 15 and Equation 16, *h* represents the height of the corresponding beam layer.

Equation 14 assumes elastic behaviour of the sample. This is strongly dependent on the investigated materials. Some problems can arise if ductile materials are investigated using this approach. Furthermore, there are certain points one has to consider when applying this method. For instance, the loading of the sample is not purely mode I and there is always a certain amount of mode II present, dependent amongst others, on the sample geometry. This means that the determined interface energy release rate is always higher than the mode I interface fracture energy.

Ma et al. [3] extended the 4PB method from Charalambides et al. [22] to be used for multilayer structures. They confined a thin multilayer film system in between two equally thick elastic silicon substrates, see Figure 7. This is the reason for predominant elastic behaviour, because silicon behaves almost ideally elastic. The dominant elastic properties are the ones from the silicon (E_{Si} and ν_{Si}) and the ones from the thin films constraint between the two silicon pieces are neglected.

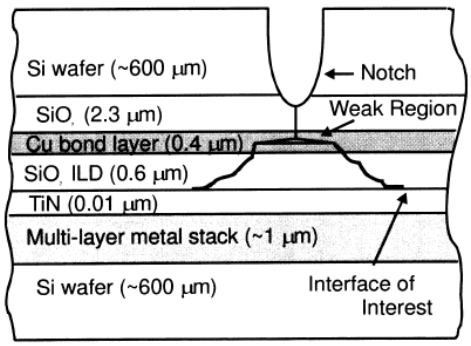

Figure 7 *Schematic sketch of a multilayer structure constrained in between two thick Si substrates. The interface of interest is marked and the crack path at crack initiation is shown. Taken from [50].*

Taking this into account, Equation 14 changes to

$$G_i = \frac{21\left(1-\nu_{Si}^2\right)M^2}{4E_{Si}b^2h^3} \quad \textit{(Eq. 17)}$$

Furthermore, there are certain requirements that have to be met to be able to evaluate an interface energy release rate, G_i, for a multilayer system. At first, the crack has to kink onto the interface of interest, the interface and, thus, the specimen needs to be long compared to the half sample height and there has to be stable crack growth along the interface in both directions. Additionally, the experimental load-displacement curve has to develop a load plateau, see Figure 8. At this load plateau the crack grows along the failing interface. When all these requirements are met, Equation 17 can be used to evaluate the interface energy release rate for the failing interface.

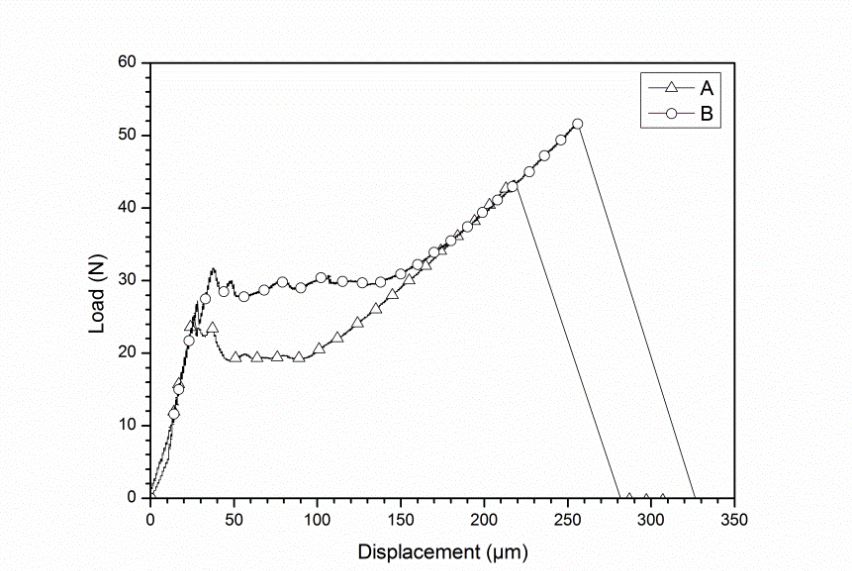

Figure 8 *Experimental 4-point-bending load-displacement curves for a W(Ti)/BPSG (A) and W(Ti)/Ti/BPSG (B) interface. Taken from [51].*

One of the problems with 4PB is the low success rate of the experiments, but there are certain ways which can be used to increase the success rate. For instance Birringer et al [9] suggested altering the sample geometry to increase the output of evaluable samples. Shaviv et al. [52] suggested to improve the output by increasing the pre-notch depth. A major concern is plastic deformation of ductile layers, which if it occurs, leads to an increase of the determined interface energy release rate [50,53]. Another influence to the interface energy release rate is the mode-mixity which depends, amongst others, on the sample geometry [22,54]. There are additional parameters influencing the interface energy release rate, like friction and loading

rate [8,52,55–57]. So, for the 4PB method the measured interface energy release rate should be viewed as an upper limit.

As already mentioned, interfaces play an important role in semiconductor devices and there are a lot of different methods to characterize them [5,21–26,32]. But most of the methods use macroscopic samples and the delamination of a large interface region is realized. To overcome that, new methods were developed over the last years, which use smaller samples to get localized adhesion information and to get closer to the actual sizes used in the devices. It is worth to note that the use of small samples can reduce the influence of plastic deformation [14]. Finally, most of the interfaces occurring in industrial use are not in thermo-dynamic equilibrium, because they are between layers which were deposited using non-equilibrium processes like chemical vapour deposition and physical vapour deposition.

As mentioned above miniaturized fracture experiments are required to probe actual device dimensions. One possible experimental method is the one by Kamiya et al. [58], where they utilized a kind of scratch test approach. Here, the structures were produced with a focused ion beam (FIB) and were sheared afterwards which gives a mode II interface strength.

The most common approach to test interfaces at small scales are micro-bending beams, as suggested by Matoy et al. [31]. There the bending beam is manufactured in such a way that the interface of interest is parallel to the loading direction. The sample setup, which was further reduced in this thesis to a submicron-size, can be seen in Figure 9.

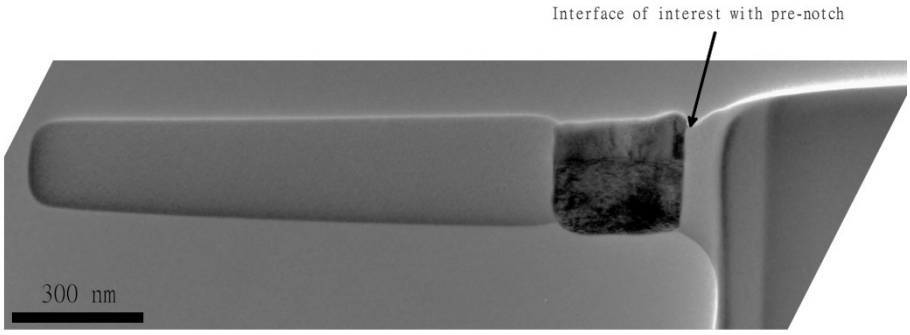

Figure 9 *TEM image of a bending beam. At the interface of interest a pre-notch, machined with a focused electron beam, of about 10 nm radius can be seen.*

The evaluation of such a bending beam can be made according to Matoy et al. [31]. They used the evaluation scheme for a semi-infinite plate with a round notch [59].

$$K = 1.12\sigma\sqrt{a\pi} \qquad \textit{(Eq. 18)}$$

In the next step the evaluated K has to be converted into a G according to Equation 9. The Young's modulus E^* used in Equation 9 to evaluate the energy release rate according is determined from Equation 19 [46]:

$$\frac{1}{E^*} = \frac{1}{2}\left(\frac{1}{E_1} + \frac{1}{E_2}\right); \qquad \textit{(Eq. 19)}$$

E^* takes into account the varying materials and Young's moduli of both sides of the interface of interest. In Equation 19, E_1 is the Young's modulus of one side of the interface of interest and E_2 represents the material on the other side, see Figure 9. The evaluated interface energy release rate has to be handled carefully, because it also contains possible plastic deformation in adjacent layers and other parameters, like friction or mode mixity to name a few. These different influences can lead to a distortion of the result and can complicate the comparison to other experiments. But if all these parameters are accounted for it can give a good estimate value for the interface energy release rate which can be compared to values determined by other microscopic or macroscopic experiments. This is discussed in more detail in Publication 4.

1.2. Analytics in the transmission electron microscope

This will be a brief introduction into the transmission electron microscope (TEM) and an overview on different methods of chemical analysis. The focus will be on the methods used in this thesis, such as scanning TEM (STEM) and energy dispersive X-ray spectroscopy (EDX). A more detailed description of TEM methods is found in [60–63].

There are two main modes in the TEM, the conventional TEM (CTEM) and STEM, see Figure 10. In CTEM a parallel beam irradiates the sample and an image is formed, like in an optical microscope, on a phosphor screen or on a CCD camera. The possible modes are bright field (BF) and dark field (DF) imaging or diffraction mode. In CTEM only one image or the diffraction pattern can be recorded at a time.

In contrast to that, in STEM a convergent beam is used and is continuously scanned across the sample, like in a scanning electron microscope, so that the information of each pixel is available.

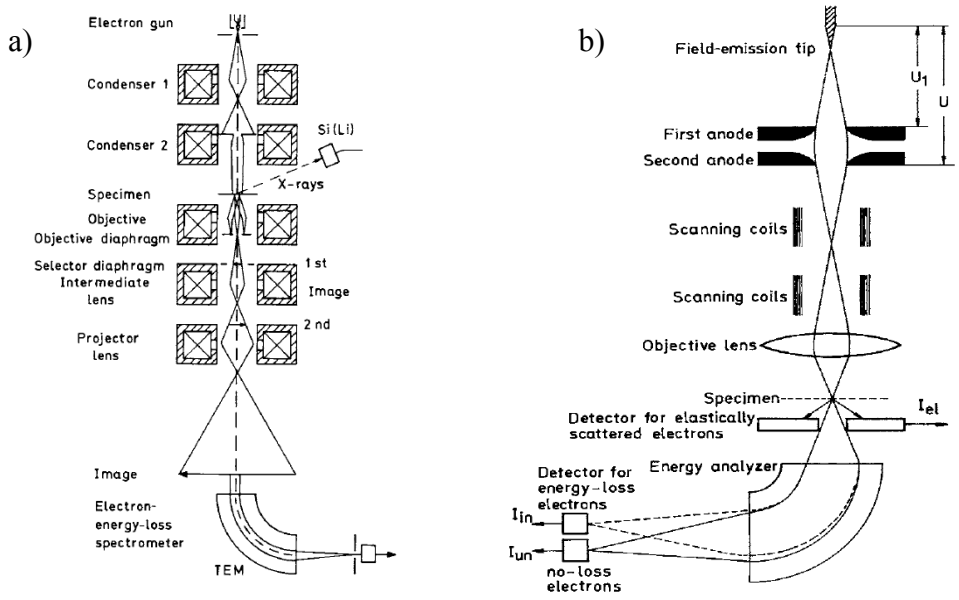

Figure 10 *Principle setup of a TEM (a) and STEM (b) with post column filter. Taken from [64].*

There are different detectors available in STEM, like a bright field detector (BF), an annular dark field detector (ADF) and the high angle annular dark field detector (HAADF), which can record different images at the same time. This is different to in CTEM where the different images have to be recorded in a serial manner.

In STEM mode it is possible to measure for each pixel the chemical information using electron energy loss spectroscopy (EELS) or EDX. EELS is favourable for light elements (Be, N, O, etc.) and EDX for heavier elements (Cu, W, etc.). In TEM only the information of the hole irradiated are is available. This gives STEM the advantage of getting very localized chemical information. The evaluation of EELS data is very complicated and as mentioned earlier does not work well for heavier elements. EDX on the other hand is a straightforward technique and data evaluation is easier compared to EELS. But the disadvantage of EDX that it is not able to quantify lighter elements with high accuracy, like B, C, N or O. Furthermore, if a detector with a Be-window is used elements below Be and Be itself cannot be detected. The principle behind EDX can be seen in Figure 11.

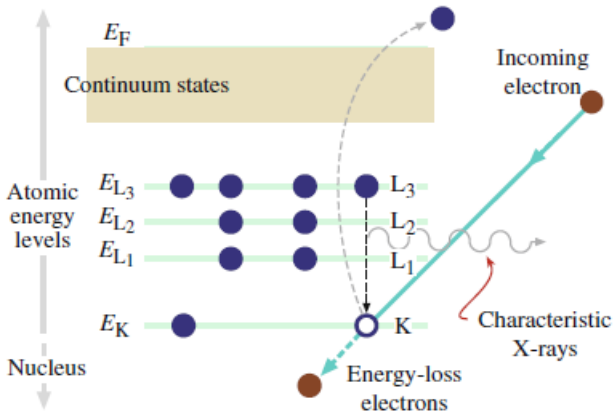

Figure 11 *Principle sketch of the EDX process. After [63].*

In Figure 11 it can be seen that the incoming electron beam can excite an electron in an inner atomic shell, leaving an empty space in that inner shell. An electron of an outer shell with a higher energy falls to this empty state. Hence, it has to lose energy and this can happen in the form of an X-ray photon. This X-ray photon has a certain energy depending on the energy level excited for the transition and this quantized photon is then detected by the EDX detector. Such photons are usually detected using Si(Li)-detectors, while the new generation are silicon drift detectors (SSDs). Another detector material is Ge. Ge detectors are preferential for higher energies (>20 keV), whilst the Si-detectors work best in the energy range from 0-20 keV, as shown in Figure 12. Disadvantages of Ge are that at around 10 keV it has an absorption edge (seen in Figure 12) and the production of Si-detectors is more developed (cost efficient) than for Ge-detectors.

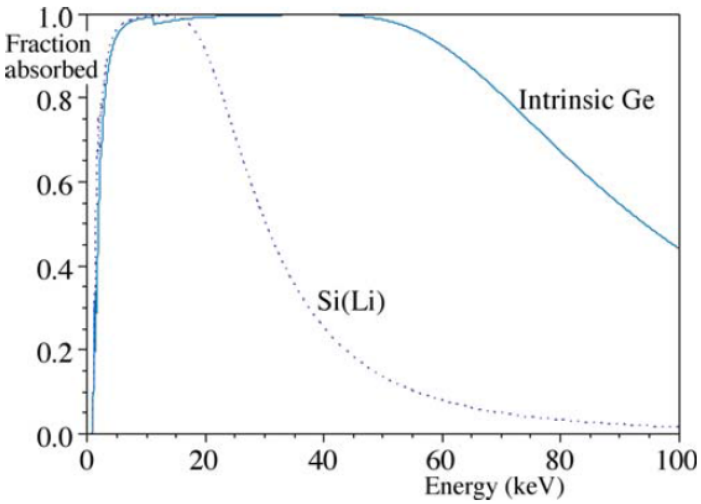

Figure 12 *Detector energy efficiency for x-rays absorbed in the detector of a Si(Li)-detector compared to a Ge-detector. From [63].*

Such a spectrum, as seen in Figure 13, can now be used to identify the materials, which possess peaks at certain energies and acts like a fingerprint for a material.

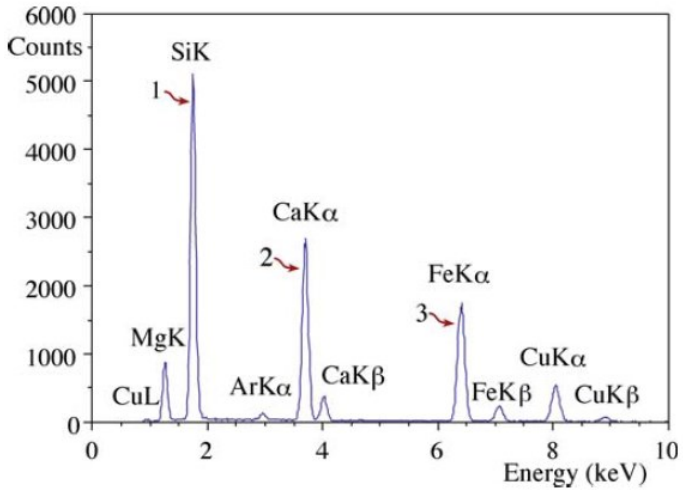

Figure 13 *Typical EDX spectrum where the different peaks are corresponding to different materials which are occurring in the sample. Taken from [63].*

If EDX or EELS is combined with STEM it is a very powerful tool to detect very localized chemical and structural information. It is even possible to detect local enrichments at certain interfaces, like on grain boundaries [65] or interfaces between different materials like metals and oxides [66]. A very detailed description of EELS in the TEM is found in [67] and EDX in the TEM is described extensively in [63].

1.3. Surface characterization techniques

There are several different methods to characterize surfaces in respect to chemical composition and topography [68–70] like secondary ion mass spectroscopy (SIMS), Auger electron spectroscopy (AES), scanning tunnel microscopy (STM), atomic force microscopy (AFM), etc.

1.3.1. Auger Electron Spectroscopy (AES)

AES is a method that can be used to identify the chemical composition of a surface and in certain cases also the chemical bonding. An advantage of AES is its surface sensitivity. The probe used to characterize the surface is an electron beam and what is detected is the energy distribution of the secondary electrons created (only the Auger electron contribution). Depending on its energy, the measured signal is emanating from the first few nm. If ion-beam sputtering is used in combination with AES it is possible to produce a depth profile of the

sample of up to few µm. A drawback of this approach is that some depth information is lost due to the mixture of the different layer because of the ion-beam bombardment. The mechanism behind AES is a competing mechanism to EDX. Instead of an X-ray photon, a secondary Auger electron, see Figure 14, is emitted. The Auger electron is an electron that is emitted due to the excess energy created from the process of an outer shell electron filling the inner shell position of the ejected electron, like in the EDX process. Instead of forming an X-ray photon the energy is transferred to the outer shell electron which is emitted. This process is preferential to the EDX process in lighter elements like Al, Mg, etc., the EDX process is favoured in heavier elements, see Figure 15.

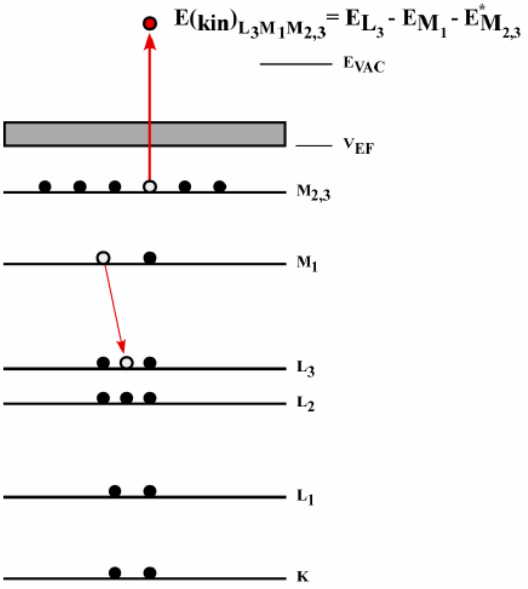

Figure 14 *Illustration of the Auger process, where an electron from an M-Shell relaxes to an L-Shell and the energy is used to emit an Auger electron from an outer shell. After [68].*

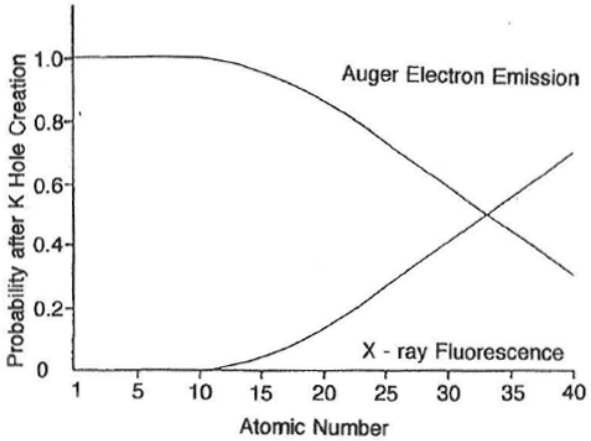

Figure 15 *Comparison of Auger electron emission and x-ray fluorescence depending on the atomic number. Taken from [69].*

1.3.2. Atomic Force Microscopy

To investigate the topography of a surface, AFM is the preferential method. AFM uses a cantilever with a sharp tip at the end, see Figure 16. The tip of the cantilever can either be in contact with the sample (contact mode) or not in contact (non-contact mode). In the non-contact mode repulsive forces like van-der Waals, electrostatic or magnetic forces are the reason for cantilever deflection. In contact mode it is the surface contour of the sample that deflects the beam. The deflection of the cantilever is measured via a reflective spot on the back of the detector which is irradiated by a laser. The detection of the laser reflections on a photodiode and the deflection of the cantilever can be detected.

There is another possibility to operate an AFM, the tapping mode. Here the cantilever is excited to oscillate near its resonance frequency. To measure the surface topography in this case the same principle of laser reflection is used as mentioned before. The difference to contact mode is that the trace of the laser reflection of the oscillating cantilever on the photodiode is followed. When the cantilever reaches a change in topography its oscillation frequency diverges from the resonance frequency. Because of that, a change of the trace of the laser reflection on the photodiode is detected. Comparing the two traces leads to measuring a phase shift, which can be related to the topography change. A sketch of contact and tapping modes is displayed in Figure 16.

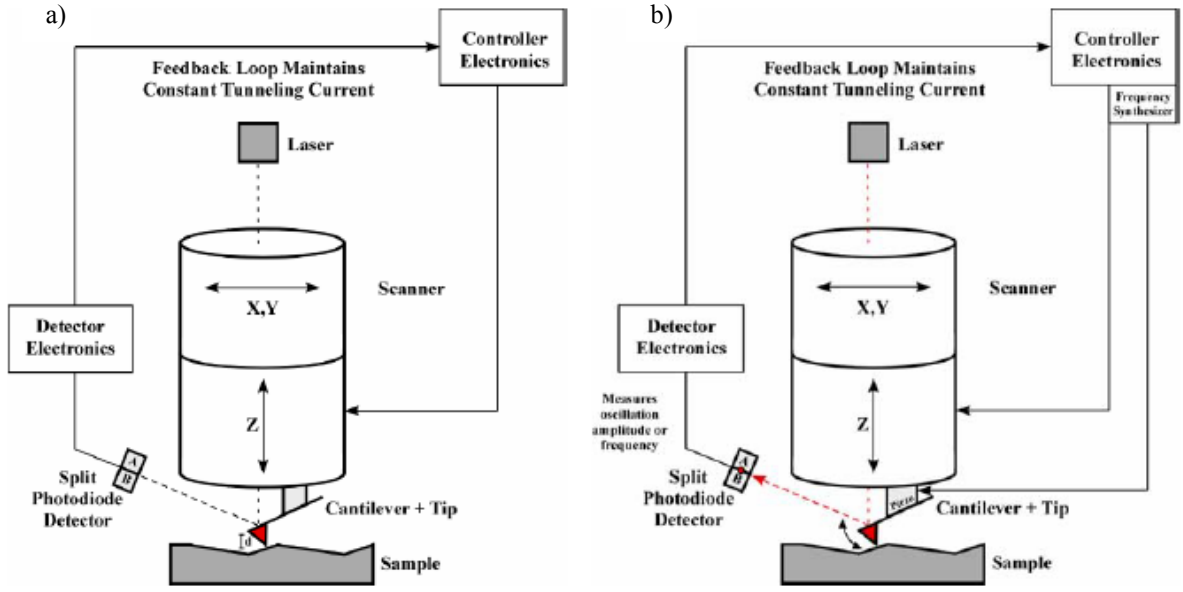

Figure 16 *Experimental setup of an AFM with the most important components. In a) the setup for contact mode is depicted and in b) the one for tapping mode. From [68].*

The accuracy of the height profile acquired through this method is lower than 1 nm, but the lateral resolution is strongly depending on the tip radius of the cantilever. Different geometries of cantilevers are available. Two examples are depicted in Figure 17.

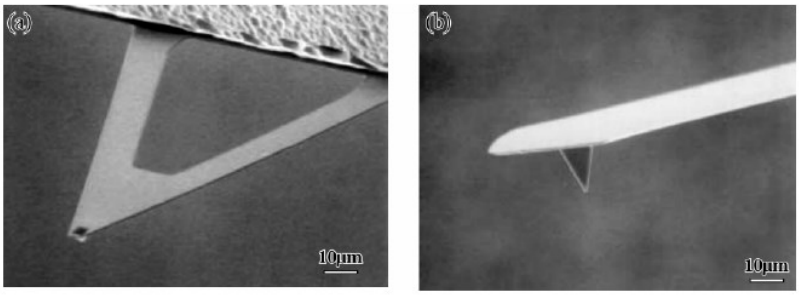

Figure 17 *Depiction of different cantilever geometries. Taken from [68].*

2. Summary and Conclusion

In the scope of this thesis different metallization layers on a dielectric borophosphosilicate glass (BPSG) were investigated. The focus was on a W layer which incorporated 20 at% Ti, from here on called W(Ti). It will be shown that the Ti incorporated in the W(Ti) layer improved the adhesion on annealed BPSG significantly, compared to a pure W layer. Furthermore, it was found that, if the Ti content is varied between 15-25 at% Ti in the W(Ti) layer no pronounced change in the interface energy release rate is measured. It was also revealed that the W(Ti) layer developed the same adhesion on a annealed BPSG as a pure Ti layer. This means that for annealed BPSG, 15 at% Ti are enough to promote the adhesion the same way as a pure Ti layer does. Another experimental series, which investigated the influence of a Ti interlayer showed similar results. The W(Ti) layer directly applied on the annealed BPSG showed the same interface energy release rate as the system with the 10 nm Ti interlayer between the W(Ti) and BPSG. The results for as-deposited BPSG differed significantly from the one obtained for annealed BPSG. Here the Ti interlayer showed a pronounced influence on the interfacial adhesion and gave an interface energy release rate around two times higher than the one for W(Ti) directly applied on as-deposited BPSG.

AES investigations of the fracture surfaces of the 4PB samples showed in all cases when the metallization layer contained Ti, that Ti residues are present on the BPSG fracture surface. This was supported by the AFM findings. There it was shown that particles are ripped out of the metallization side of the sample and stick to the BPSG fracture surface. Combining the AES and AFM findings suggests that the particles found on the surface are Ti-based particles.

The analytical investigation of the W(Ti) interface in the TEM showed that because of a final 400 °C anneal during sample production a Ti enrichment at the interface is occurring. This Ti excess was not found if the final 400 °C anneal is omitted. For future investigations the influence of the final 400 °C anneal on the adhesion of the W(Ti) layer on BPSG could be interesting.

To verify the comparability of 4PB tests and in-situ submicron-sized bending beams the interface between Cu and annealed BPSG was investigated. The 4PB experiments showed a weak interface for this system. In-situ 4PB tests in the SEM gave the opportunity to identify the failing interface during the experiment without using additional methods, like AES, on the fracture surfaces of the samples after the 4PB tests. In addition it was possible to gain more insight on the crack initiation and growth.

The results for the interface energy release rate of the ex-situ and in-situ 4PB tests of the Cu/BPSG interface are in good agreement with each other. If these are compared to the results

of the in-situ TEM submicron-sized bending beam tests, the latter showed a lower value for the interface energy release rate, than that found by 4PB. This behaviour can be explained by the smallest dimension of the Cu layer for each investigation. In the 4PB test it is 300 nm and in the TEM bending beam it is about 100 nm. This concludes that more plastic deformation can be accommodated in the thicker layer, which leads to an increase in the calculated interface energy release rate for the 4PB experiment, as presented in the findings of Kriese et al. [14].

Based on the findings of this thesis it can be concluded that alloying W with Ti increases the adhesion to BPSG layer. Thus, a separate Ti adhesion layer can be omitted if 15 to 25 at% Ti are contained in the W film. This amount of Ti is above the solubility limit in W and leads to a segregation of Ti to the W(Ti)/BPSG interface. Thus, it can be speculated that segregation of well-selected alloying elements opens a route for mechanical interface strengthening.

The novel in-situ 4-point-bending approaches developed in this work provide now a tool, which helps to avoid time consuming post-mortem investigations of the fracture mechanical testing to submicron component dimensions has come into reach as the successful measurement of Cu/BPSG samples in the TEM demonstrated.

References

[1] S. Varchenya, A. Simanovskis, S. Stolyarova, Thin Solid Films 164 (1988) 147.
[2] M. Kottke, J. Vac. Sci. Technol. B Microelectron. Nanometer Struct. 10 (1992) 1124.
[3] Q. Ma, H. Fujimoto, P. Flinn, V. Jain, F. Adibi-Rizi, F. Moghadam, R.H. Dauskardt, in:, Mater. Res. Soc. Symp. - Proc., 1995.
[4] S. Venkataraman, D.L. Kohlstedt, W.W. Gerberich, J. Mater. Res. 11 (1996) 3133.
[5] A.A. Volinsky, N.R. Moody, W.W. Gerberich, Acta Mater. 50 (2002) 441.
[6] M.J. Cordill, N.R. Moody, D.F. Bahr, J. Mater. Res. 19 (2004) 1818.
[7] M.J. Cordill, D.F. Bahr, N.R. Moody, W.W. Gerberich, IEEE Trans. Device Mater. Reliab. 4 (2004) 163.
[8] Z. Cui, G. Dixit, L. Xia, A. Demos, B.H. Kim, D. Witty, H. M'Saad, R.H. Dauskardt, in:, AIP Conf. Proc., 2005, pp. 507–511.
[9] R.P. Birringer, P.J. Chidester, R.H. Dauskardt, Eng. Fract. Mech. 78 (2011) 2390.
[10] S.W. Russell, S.A. Rafalski, R.L. Spreitzer, J. Li, M. Moinpour, F. Moghadam, T.L. Alford, Thin Solid Films 262 (1995) 154.
[11] S.A. Rafalski, R.L. Spreitzer, S.W. Russell, T.L. Alford, J. Li, M. Moinpour, F. Moghadam, J.W. Mayer, in:, Mater. Res. Soc. Symp. - Proc., 1994, pp. 613–618.
[12] S.D. McAdams, T.Y. Tsui, W.C. Oliver, G.M. Pharr, in:, MRS Proc., 1994.
[13] G. Dehm, M. Rühle, H.D. Conway, R. Raj, Acta Mater. 45 (1997) 489.
[14] M.D. Kriese, N.R. Moody, W.W. Gerberich, Acta Mater. 46 (1998) 6623.
[15] S. Jacobson, B. Jönsson, B. Subdqvist, Thin Solid Films 107 (1983) 89.
[16] C.W. White, G. Farlow, J. Narayan, G.J. Clark, J.E.E. Baglin, Mater. Lett. 2 (1984) 367.
[17] J.E.E. Baglin, G.J. Clark, Nucl. Instrum. Methods Phys. Res. Sect. B Beam Interact. Mater. At. 7 (1985) 881.
[18] P.A. Ingemarsson, B.U.R. Sundqvist, C.W. Nieh, T.A. Tombrello, Appl. Phys. Lett. 54 (1989) 1513.
[19] S. Sugden, C.J. Sofield, M.P. Murrell, Nucl. Inst Methods Phys. Res. B 44 (1989) 137.
[20] J.E.E. Baglin, Nucl. Inst Methods Phys. Res. B 65 (1992) 119.
[21] M.P. de Boer, M. Kriese, W.W. Gerberich, J. Mater. Res. 12 (1997) 2673.
[22] P.G. Charalambides, J. Lund, A.G. Evans, R.M. McMeeking, J. Appl. Mech. Trans. ASME 56 (1989) 77.
[23] A. Bagchi, G. Lucas, Z. Suo, A. Evans, J. Mater. Res. 9 (1994) 1734.
[24] D.B. Marshall, A.G. Evans, J. Appl. Phys. 56 (1984) 2632.
[25] M.D. Kriese, W.W. Gerberich, N.R. Moody, J. Mater. Res. 14 (1999) 3007.
[26] M.D. Kriese, W.W. Gerberich, N.R. Moody, J. Mater. Res. 14 (1999) 3019.
[27] M.J. Cordill, N.R. Moody, D.F. Bahr, Acta Mater. 53 (2005) 2555.
[28] J.M. Whitney, C.E. Browning, W. Hoogsteden, J. Reinf. Plast. Compos. 1 (1982) 297.
[29] E. Barthel, O. Kerjan, P. Nael, N. Nadaud, Thin Solid Films 473 (2005) 272.
[30] H. Hirakata, Y. Takahashi, D. Truong, T. Kitamura, Int. J. Fract. 145 (2007) 261.
[31] K. Matoy, T. Detzel, M. Müller, C. Motz, G. Dehm, Surf. Coat. Technol. 204 (2009) 878.
[32] J. Chen, S.J. Bull, J. Phys. Appl. Phys. 44 (2011) 034001.
[33] J.F. Knott, Fundamentals of Fracture Mechanics, Gruppo Italiano Frattura, 1973.
[34] H.L. Ewalds, R.J.H. Wanhill, Fracture Mechanics, Edward Arnold (Publishers), 1984.
[35] T.L. Anderson, Fracture Mechanics: Fundamentals and Applications, Third Edition, CRC Press, 2005.
[36] D. Gross, T. Seelig, Fracture Mechanics: With an Introduction to Micromechanics, Springer Science & Business Media, 2011.

[37] A.A. Griffith, Philos. Trans. R. Soc. Lond. Ser. Contain. Pap. Math. Phys. Character 221 (1921) 163.
[38] G.R. Irwin, J. Appl. Mech. 24 (1957) 361.
[39] Y. Murakami, Stress Intensity Factors Handbook. 1 (1987), Elsevier Science Limited, 1987.
[40] H. Tada, P.C. Paris, G.R. Irwin, The Analysis of Cracks Handbook, New York: ASME Press, 2000.
[41] J.R. Rice, J. Appl. Mech. Trans. ASME 55 (1988) 98.
[42] M.-Y. He, J.W. Hutchinson, Int. J. Solids Struct. 25 (1989) 1053.
[43] M.-Y. He, J.W. Hutchinson, J. Appl. Mech. Trans. ASME 56 (1989) 270.
[44] Z. Suo, J.W. Hutchinson, Mater. Sci. Eng. A 107 (1989) 135.
[45] Z. Suo, J.W. Hutchinson, Int. J. Fract. 43 (1990) 1.
[46] J. Hutchinson, Z. Suo, Adv. Appl. Mech. 29 (1992) 191.
[47] L. Banks-Sills, D. Ashkenazi, Int. J. Fract. 103 (2000) 177.
[48] K.M. Liechti, Y.-S. Chai, J. Appl. Mech. 58 (1991) 680.
[49] K.M. Liechti, Y.S. Chai, J. Appl. Mech. 59 (1992) 295.
[50] R.H. Dauskardt, M. Lane, Q. Ma, N. Krishna, Eng. Fract. Mech. 61 (1998) 141.
[51] B. Völker, W. Heinz, K. Matoy, R. Roth, J.M. Batke, T. Schöberl, C. Scheu, G. Dehm, Philos. Mag. (2014) DOI: 10.1080/14786435.2014.913108.
[52] R. Shaviv, S. Roham, P. Woytowitz, Microelectron. Eng. 82 (2005) 99.
[53] A.G. Evans, J.W. Hutchinson, Y. Wei, Acta Mater. 47 (1999) 4093.
[54] P. Charalambides, H. Cao, J. Lund, A. Evans, Mech. Mater. 8 (1990) 269.
[55] C.S. Litteken, S. Strohband, R.H. Dauskardt, Acta Mater. 53 (2005) 1955.
[56] D.M. Gage, K. Kim, C.S. Litteken, R.H. Dauskardt, J. Mater. Res. 23 (2008) 87.
[57] S. Roham, T. Hight, Microelectron. Eng. 84 (2007) 72.
[58] S. Kamiya, H. Kimura, K. Yamanobe, M. Saka, H. Abe, Thin Solid Films 414 (2002) 91.
[59] H. Tada, P.C. Paris, G.R. Irwin, The Stress Analysis of Cracks Handbook, Third Edition, ASME, Three Park Avenue New York, NY 10016-5990, 2000.
[60] S. Amelinckx, D. van Dyck, J. van Landuyt, G. van Tendeloo, Electron Microscopy: Principles and Fundamentals, John Wiley & Sons, 2008.
[61] R. Egerton, Physical Principles of Electron Microscopy: An Introduction to TEM, SEM, and AEM, Springer Science & Business Media, 2005.
[62] B. Fultz, J.M. Howe, Transmission Electron Microscopy and Diffractometry of Materials (Third Edition), Springer, Heidelberg, 2007.
[63] D.B. Williams, C.B. Carter, Transmission Electron Microscopy: A Textbook for Materials Science, Springer Science & Business Media, 2009.
[64] L. Reimer, H. Kohl, Transmission Electron Microscopy: Physics of Image Formation, Springer Science & Business Media, 2008.
[65] J.A.S. Ikeda, Y.-M. Chiang, A.J. Garratt-Reed, J.B.V. Sande, J. Am. Ceram. Soc. 76 (1993) 2447.
[66] C. Scheu, J. Microsc. 207 (2002) 52.
[67] R. Egerton, Electron Energy-Loss Spectroscopy in the Electron Microscope, Springer Science & Business Media, 2011.
[68] D. Brandon, W.D. Kaplan, Microstructural Characterization of Materials, John Wiley & Sons, 2013.
[69] R.W. Cahn, P. Haasen, E.J. Kramer, Materials Science and Technology: A Comprehensive Treatment, Wiley-VCH, 1998.
[70] C.R. Brundle, C.A. Evans, S. Wilson, Encyclopedia of Materials Characterization: Surfaces, Interfaces, Thin Films, Gulf Professional Publishing, 1992.

Publication 1

Published in Philosophical Magazine
DOI: 10.1080/14786435.2014.913108

Interface fracture and chemistry of a tungsten based metallization on borophosphosilicate glass

B. Völker[1,2], W. Heinz[1], K. Matoy[3], R. Roth[3], J.M. Batke[4], T. Schöberl[5], C. Scheu[6] and G. Dehm[7]

[1] KAI - Kompetenzzentrum Automobil- und Industrieelektronik GmbH, Technologiepark Villach, Europastrasse 8, 9524 Villach, Austria

[2] Department Materials Physics, University of Leoben, 8700 Leoben, Austria

[3] Infineon Technologies AG, 9500 Villach, Austria

[4] Infineon Technologies AG, 93049 Regensburg, Germany

[5] Erich Schmid Institute of Materials Science of the Austrian Academy of Sciences, Jahnstrasse 12, 8700 Leoben, Austria

[6] Department of Chemistry, Ludwig-Maximilians-University, Butenandstrasse11, 81377 München, Germany

[7] Max-Planck-Institut für Eisenforschung GmbH, 40237 Düsseldorf, Germany

Abstract

In microelectronic devices, the interface between barrier metal and dielectric is of particular interest for a reliable electronic functionality. However, it is frequently observed that this interface is prone to failure. In this work, the strength of interfaces between an as-deposited borophosphosilicate dielectric glass (BPSG) layer and a W(Ti) metallization with and without Ti interlayer was in the centre of interest. Four-point-bending tests were used for the mechanical characterization combined with a topological and chemical analysis of the fracture surfaces. In addition, the interface chemistry was studied locally prior to the testing to search for a possible Ti enrichment at the interface. The fracture results will be discussed taking the chemical and topological information into account.

1. Introduction

Interfaces play an important role in microelectronic devices where a multitude of different materials must be combined to achieve the required electronic functionality. However, the mechanical stability of interfaces between different materials are often weak points limiting the lifetime of devices by interfacial fracture. There are numerous interfaces present in such devices between different materials. Especially critical are interfaces between materials of different bonding characteristics such as interfaces between ionic-covalent dielectrics and metals. As a consequence several studies addressed the adhesion of dielectric/metallization interfaces [1–6]. For instance Ma et al. [2] investigated the interface between TiN/SiO_X in a multilayer structure using the 4-point-bending technique. Lane et al. [5] investigated Ta and TaN layers on SiO_X based substrates using 4-point-bending tests. According to their investigations pure Ta adheres weaker to SiO_X than TaN and the higher the N content in the TaN the higher the interface strength. Further, Kinbara et al. [4] studied different materials including metals and inorganic layers on a glass substrate. They used the scratch test method to perform their experiments. Using this method they could not calculate an interface energy release rate but they showed that the adhesion for different materials differs substantially.

In principle all studies revealed a rather weak adhesion for such interfaces, remedies to enhance the adhesion, such as incorporating a Ti interlayer and ion beam treatments were proposed [7–10]. Rafalski et al. [7] and Russel et al. [9] showed that the adhesion of Cu films on SiO_X, phosphosilicate glass (PSG) or borophosphosilicate glass (BPSG) could be enhanced, as mentioned before, by using a Ti interlayer or also by using a Cr interlayer. It was demonstrated by Dehm et al. [11] that even a Ti layer with a thickness of about 0.7 nm significantly improves the adhesion of Cu on α-Al_2O_3. Another approach suggested by Rafalski et al. [7] and Russel et al. [9] to promote adhesion is to incorporate Ti or Cr into the Cu layer. They reported that the Ti or Cr in the Cu layer migrates to the interface and enhances the adhesion by reacting with the SiO_X based substrate. Another possibility to enhance adhesion is ion bombardment of the interface as suggested by Baglin et al. [8].

The focus of this study lies on W(Ti), which is often used in semiconductor devices as a barrier metal to prevent diffusion of the Al metallization into the dielectric[12–14]. It was reported by McAdams et al. [15] that W(Ti) can be used as an adhesion promoting layer for Cu and Au on silicon substrates. This was also found by Matoy et al. [16] for a layer of W and W(Ti) on SiO_X using micro-bending beams, where an increase in interface energy release rate from around 3 J/m^2 to about 4.5 J/m^2 was determined. This combination of barrier

metallization and dielectric is frequently employed in actual devices but has not been systematically studied regarding interfacial strength and chemistry.

A number of different methods exist for characterizing the adhesion of such interfaces, like four point bending [1,3,17], scratch testing [18], superlayer test [19,20], indentation test [21,22], double cantilever beam test [23] and many others. A comprehensive overview of the different methods for testing interfaces is given in Volinsky et al. [24]. But either they are not fit for testing multilayer systems or they do not provide a quantity for the interface energy release rate. The 4-point-bending technique according to Ma et al. [1] is one of the few techniques which is suitable for multilayer systems like the one under investigation. In addition, it also provides a quantitative measure of the interfacial energy release rate.

The aims of this study are to sort out if a Ti interlayer increases the interfacial strength between W(Ti)/as-deposited BPSG or if the Ti that is alloyed into the W is sufficient and no further increase in interfacial adhesion does occur. To achieve this it is necessary to evaluate quantitative energy release rate data for the material systems under investigation. Further, chemical and morphological analysis of the fracture surfaces are performed to obtain insights into interface chemistry and the crack path along the interface.

2. Experimental Details

To characterize the adhesion between as-deposited BPSG and W which contains about 20 at% Ti (hereafter W(Ti)), and the influence of a nominally 10 nm thick Ti interlayer, 4-point-bending tests [1,3,17] were made. The sample preparation and geometry is based on [25] and schematically sketched in Figure 1.

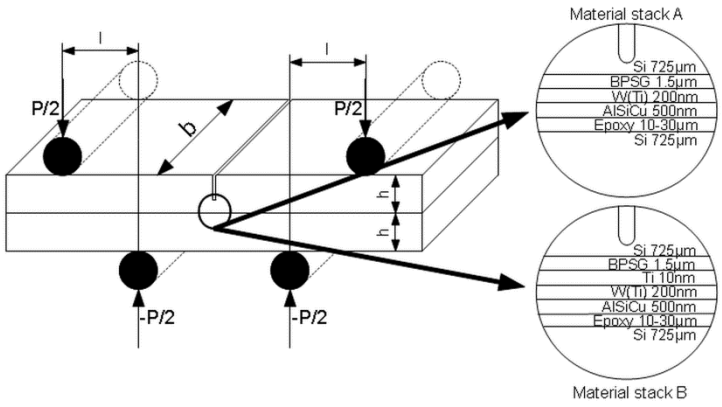

Figure 1 *Principle sketch of the 4-point-bending test with important measurement quantities: l - distance between inner and outer pins, b - width of the sample, h - half height of the sample and ±P/2 - half applied load. Two different material stacks A and B are analysed in the present work with the layer structure and thickness values provided in the enlarged sketch.*

Two different material stacks, A and B, were used to characterize the adhesion of dielectric to metallization. On a 725 µm-thick (100) Si wafer a 1.5 µm-thick BPSG layer was deposited using a plasma enhanced chemical vapour deposition (PECVD) process. For material stack A the W(Ti) was deposited directly on the BPSG while for material stack B a 10 nm-thick Ti interlayer was laid down before the 200 nm W(Ti). The deposition of the metallization layers was done by magnetron sputtering in vacuum. In both cases, an AlSiCu layer was deposited, also by magnetron sputtering, on top, firstly to get a more realistic material structure and secondly to promote the adhesion of the epoxy used to glue the Si counterpart, with a thickness of 725µm, to the material stacks A or B. After the last deposition process all, wafers were heat treated in an inert gas atmosphere at 400 °C for 1 hour.

The notch, with a depth of (500 ± 5) µm and a nominal width of 36 µm, which is necessary for the 4-point-bending test, was introduced into the Si side of the material stacks using a wafer saw (see Figure 1). To be comparable, all samples for material stack A and B had the same geometry, as can be seen in Figure 1. The length of the samples was 40 mm, the thickness was about 1.45 mm and the width was 7 mm.

Testing was done on a Kammrath & Weiss bending module, with an inner pin spacing of 20 mm and an outer pin spacing of 30 mm. The chosen testing speed was 0.1 µm/s.

For material stack A 15 samples and for material stack B 20 samples, were tested. Not all of the tested samples could be used to determine a quantitative interface energy release rate. Only six samples of material stack A and three samples of material stack B fulfilled strict requirements, which are as follows: Firstly, the interface has to fracture along both sides perpendicular to the notch, not only on one side. Secondly, the crack has to move along the interface and not kink into one of the adjacent materials. Finally, the load-displacement curve has to develop a plateau. Only if all three requirements are fulfilled, the experiment is counted as a valid energy release rate test and Equation (1) [1,17,25] is applied to determine the interface energy release rate G_i:

$$G_i = \frac{21\left(1-\nu^2\right)M^2}{4\mathrm{Eh}^3} \quad \text{with} \quad M = \frac{Pl}{2\mathrm{b}} \qquad \textit{(Eq. 1)}$$

Thereby, ν is the Poisson's ratio of 0.28 for Si (100) oriented [26], E the Young's modulus of 130 GPa for (100) orientation of Si [26], h the half sample height of about 725µm and M the

normalized bending moment which is calculated from the force *P*, the distance *l* of 5 mm between inner and outer pins, and the width *b* with 7mm of the sample (see Figure 1).
The sample standard deviation:

$$s = \sqrt{\left(\frac{1}{n-1}\right)\sum_{i=1}^{n}\left(x_i - \bar{x}\right)^2} \qquad \textit{(Eq. 2)}$$

is used to calculate the uncertainty in the energy release rate. In this investigation, the yield of samples which could be used to evaluate an interface energy release rate was moderate (six for material stack A and three for material stack B). To improve the sample yield Birringer et al. [27] mentioned several possible sample geometries, such as a 45° sample for which the orientation of the lower Si counterpart is 45° rotated compared to the upper Si substrate, or the T-beam specimen, where the width of the lower Si part is larger than the one of the upper Si substrate.
To determine which interface failed, energy-dispersive x-ray spectroscopy (EDX) in a scanning electron microscope (SEM, Zeiss LEO 1525), operated at an acceleration voltage of 20 kV, and Auger electron spectroscopy (AES, PHI Scanning Auger Nanoprobe), performed at an acceleration voltage of 5 kV, were carried out on the two opponent fracture surfaces of material stacks A and B. Additionally, atomic force microscopy (AFM) measurements, using a DI (Veeco) scanning probe microscope Dimension 3100 combined with a Nanoscope III controller, were performed in tapping mode to determine the fracture surface topography and thus the fracture path. The investigation was done for both fracture surfaces of a sample of each material stack.
Characterization of the intact interface was done by EDX line scans and EDX box measurements in the transmission electron microscope (TEM) following the approach of Ikeda et al. [28] and Scheu [29]. Cross sectional samples were prepared using the focused ion beam (FIB) lift-out method in the case of material stack A and conventional mechanical cutting, grinding, dimpling and Ar-ion milling in the case of material stack B. Measurements were made on a JEOL 2100F image-side Cs-corrected microscope in STEM mode. The line scans were done using spectrum imaging in DigitalMicrograph® with drift control. A step size of 0.8 nm and a beam diameter of 0.5 nm were used. Evaluation of the line scans was done by plotting the Ti amount along the scan line. Caution has to be taken when plotting the W and Si lines, because the W-M_α line at 1.774 keV and the Si-K_α line at 1.740 keV overlap.

For the box measurements, the SimpleImageViewer® from JEOL was used to define a measurement window with 5 nm width and 30 nm length. The beam was continuously scanned across the window to record the spectra. The reference spectra of the W(Ti) and BPSG films were recorded at a distance of ~50 nm from the interface as indicated in the high-angle annular dark field (HAADF) image in Figure 2.

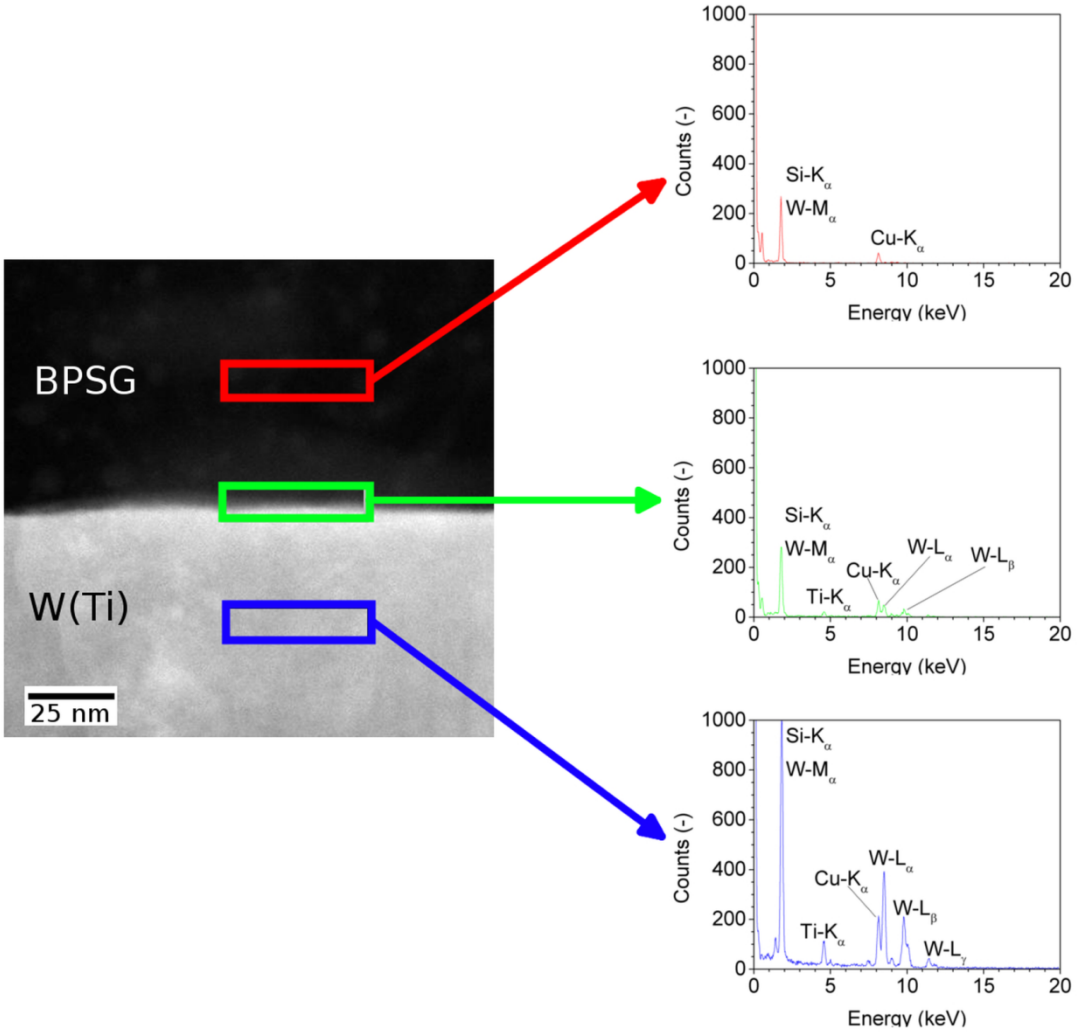

Figure 2 *HAADF image with three measurement areas (boxes) marked, one in the BPSG layer (dark region) and one in the W(Ti) layer (bright region) as reference measurements. One of the three interface measurements is also depicted. Furthermore, the corresponding EDX spectra are shown on the right side. In each spectra, the relevant peaks are labelled. For the interface measurement, it is obvious that only a part of the W(Ti) layer contributes to the measurement signal. To determine how much the contribution is, the W-L_α peak at the interface is compared to the one of the W(Ti) reference measurement.*

At the interface, three spectra were acquired for each region to get better statistics. The spectra were recorded using DigitalMicrograph® and each measurement lasted 180 s. The box measurements were only performed for material stack A to search for a possible Ti enrichment at the W(Ti)/BPSG interface. Interpretation of all the EDX box measurements was

done according to Ikeda et al. [28] and Scheu [29]. For each EDX spectrum, a Gauss peak was fitted to the Ti-K_α and the W-L_α peak. The area under the Gauss curve was determined. The area for Ti-K_α was set in relation to the area of the W-K_α Gauss fit, for each spectra acquired in the W(Ti) and at the interface. Finally, the relation between areas was used to calculate the at% ratio of Ti to W with a proportionality factor, the Cliff-Lorimer factor, which was determined using DigitalMicrograph® and a Ti:W ration of 20:80. This approach permits to detect a possible Ti enrichment and W depletion at the interface. The Ti enrichment is given in excess atoms/nm^2 (Γ_{Int}) and the equation used for its determination is according to Ikeda et al. [28]:

$$\Gamma_{Int} = \Delta C_{Ti} \rho_V d \qquad \dots \qquad (Eq.\ 3)$$

where ΔC_{Ti} is the concentration excess of Ti at the interface compared to the reference W(Ti) layer, ρ_V is the atomic density (atoms per unit volume) and d the height contribution of the W(Ti) layer to the measurement box at the interface. To determine to what extend the W(Ti) layer contributes to the box height at the interface measurement, it was assumed that the area under the Gauss peak of W-L_α in the W(Ti) reference measurement provides the value for the entire box height. Is this area now compared to the area under the Gauss fit at the interface, this relation gives the W(Ti) contribution to the interface measurement box height.

3. Results and interpretation

In Figure 3, examples of load-displacement curves for material stacks A and B, which were obtained during 4-point-bend testing, are depicted. In the beginning, the load rises until it reaches the point where the energy is sufficiently high to advance the crack through the different layers to the interface. Once the crack reaches a weak enough interface, it moves along this interface. As long as the crack is located between the two inner pins (see Figure 1), the load remains about constant. This can be seen as a plateau in the load-displacement curves in Figure 3. Once the crack reaches the two inner pins, the load rises again until the specimen fails completely.

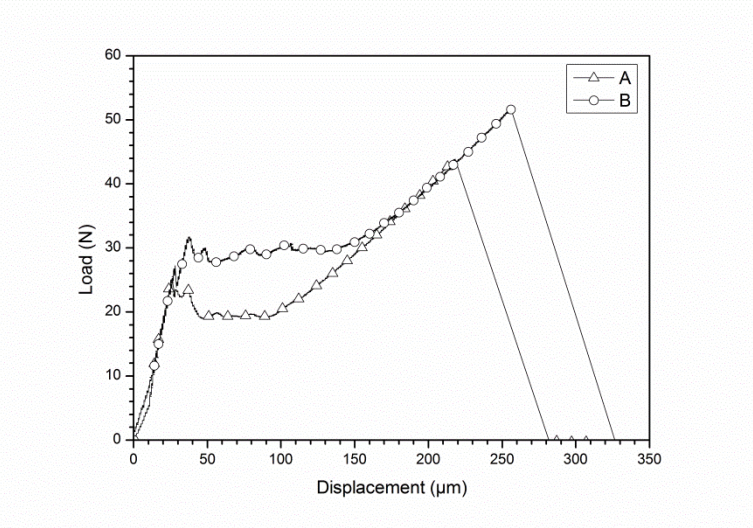

Figure 3 *Two examples for load-displacement curves for material stacks A and B are shown. For both materials the load rises in the beginning until the energy is sufficiently high to advance a crack from the notch through the different material layers to the interface. The region of constant load (plateau region) indicates interface fracture. When the crack reaches the two inner pins, the load rises again until the sample fails catastrophically. Note that for material stack A, the plateau load is significantly lower than for material stack B, revealing that the interface strength for material stack B exceeds that for material stack A.*

The value of the interface energy release rate calculated according to Equation (1) is (4.9 ± 0.2) J/m^2 for material stack A and (11.7 ± 0.4) J/m^2 for material stack B. These values for the interface strength also include the plastic deformation in the adjacent layers, like the AlSiCu and the epoxy layer. So, the two values above are an upper bound of the actual interface bond strength.

The 4-point-bending tests for material stack B revealed, as expected, that the Ti interlayer promotes the adhesion. The metallization of material stack A, without Ti interlayer, developed a much lower interface adhesion on BPSG compared to material stack B. This can be seen in the plateau load in Figure 3, which is higher for material stack B.

The EDX measurements of the fracture surfaces recorded in the SEM revealed that in all cases one side of the fracture surface showed only a signal from Si and O, while the other fracture surface contained signals from W and Ti. This indicated that for both material stacks, failure occurred at the interface between BPSG and metallization, i.e. W(Ti) for material stack A and Ti for material stack B. However, one disadvantage of EDX in the SEM is that the detected signal not only contains information from the surface but also from the material below up to a depth of ~3 µm.[1] Thus, if the surface layer is only a few atomic layers thick, the signal may be below the signal to noise detection limit. In order to clarify these questions, AES measurements were conducted due to its high surface sensitivity.

Results of the AES measurements are presented in Figure 4(a)-(e). AES spectra were recorded for the BPSG fracture surface of material stack A before and after removing surface atoms by

sputtering (Figure 4(a) and (b)). All other fracture surfaces were analysed using AES depth profiles (Figure 4(c)-(e)).

Figure 4(a) and (b) show AES spectra, before (Figure 4(a)) and after (Figure 4(b)) sputtering. In both cases, Si and O are found. Before sputtering, carbon contamination is present, due to exposure to air and previous SEM measurements, which is removed after sputtering. The sputtering was just a short burst of a few seconds of ion bombardment. The AES depth profile in Figure 4(c), which also includes surface information of the fractured materials, at the W(Ti) side of material stack A reveals only the presence of a W(Ti) layer. This confirms the EDX measurements and leads to the conclusion that fracture occurs along the dielectric to metallization interface (BPSG to W(Ti)).

Figure 4(d) and (e) show two AES depth profiles for material stack B. Figure 4(d) resolves mainly Si and O which corresponds to the BPSG layer and also 10 at% Ti. For the Ti/W(Ti) surface (Figure 4(e)), it can be seen that at first the Ti interlayer is present and afterwards the W of the W(Ti) layer appears. For material stack B, the failing interface is dielectric to metallization, in this case BPSG to Ti, as revealed by both techniques, EDX and AES. Furthermore, the AES data indicates that some Ti residues are present on the BPSG facture surface of material stack B. In contrast to that no Ti residues were found on the BPSG fracture surface of material stack A.

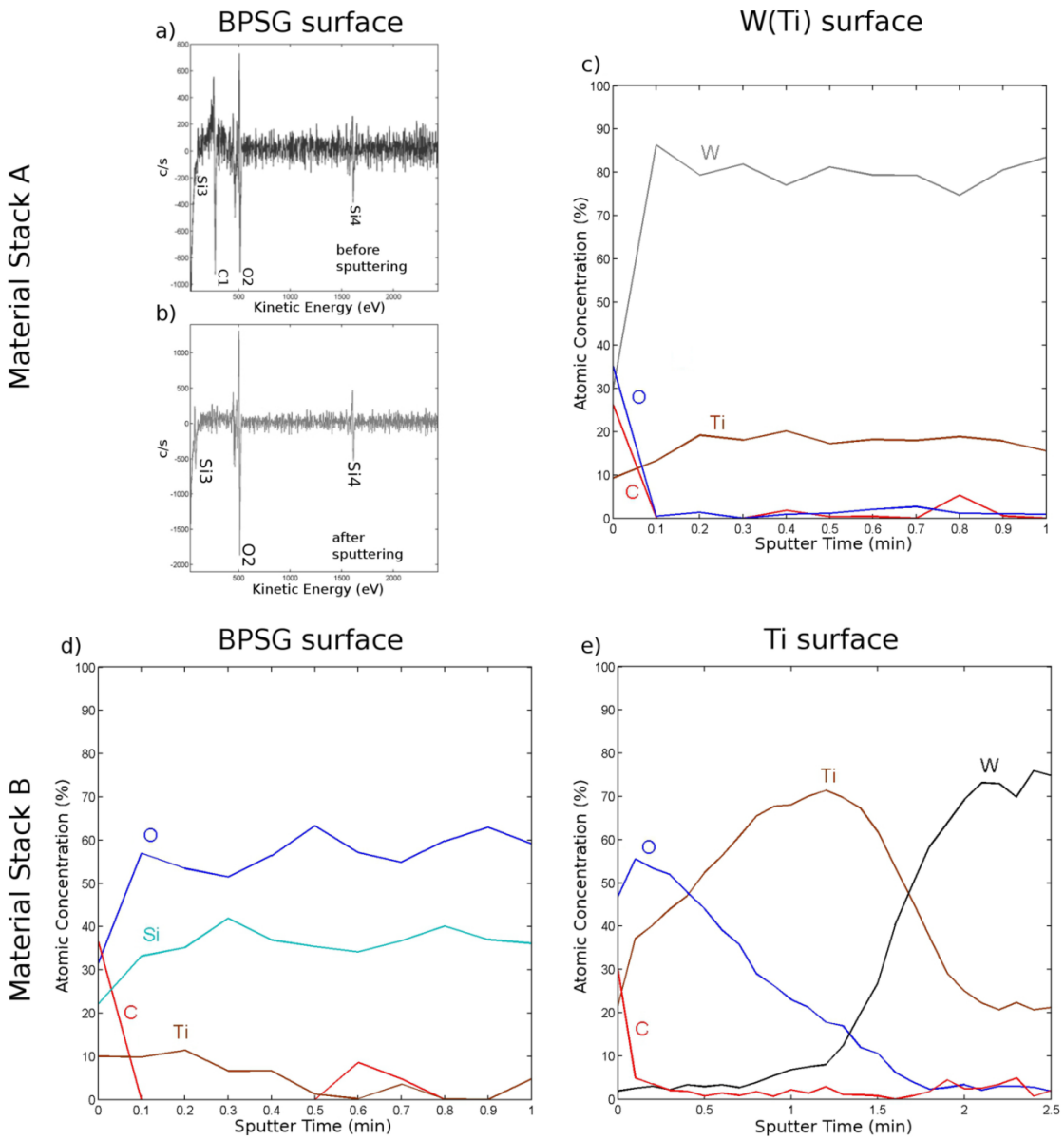

Figure 4 *AES spectra and depth profiles of the fracture surfaces for material stacks A and B. In (a) and (b), AES spectra before and after sputtering are shown and (c), (d), and (e) depict chemical depth profiles. (d) AES depth profile of the BPSG surface of material stack B. Si and O of the BPSG are present and some Ti residues are found on the surface. The AES depth profile of the metallization surface of material stack B (with Ti interlayer) can be seen in (e). See text for details.*

AFM measurements of all types of fracture surfaces revealed that they are very smooth with a surface roughness of several nm for the metallic side of the fracture surface (Figure 5(a) and (b)) and ~1nm for the BPSG (Figure 5(c) and (d)) side. This higher value in roughness for the metallization side could be attributed to relaxation of intrinsic stresses in the metallization layer occurring in the course of interface fracture. Further information gained using the AFM measurements is the presence of small cavities on the metallization fracture surface visible as dark spots in the AFM maps for material stacks A and B (Figure 5(a) and (b)). On the BPSG surfaces of both materials, elevated particles are resolved as bright appearing spots in the

AFM images (Figure 5(c) and (d)). The size of the particles on the BPSG and the size of the cavities found on the metallization match. Most probably, small metallic particles (grains) are extracted from the metallization layer and adhere to the dielectric surface. This interpretation is further supported by the AES results for material stack B which indicates traces of Ti on the BPSG fracture surface. The amount of Ti found on the BPSG fracture surface using AES and the evaluated area density using the AFM measurements differ significantly. According to AES, there should be around 10% Ti on the fracture surface. The evaluation of the area density gives only a value of about 3%. This difference may occur because AFM measures the topography revealing small three-dimensional particles, while the chemical content of 10% could also reflect the possibility that some Ti adatoms are attached to the BPSG fracture surface without forming a noticeable three-dimensional structure.

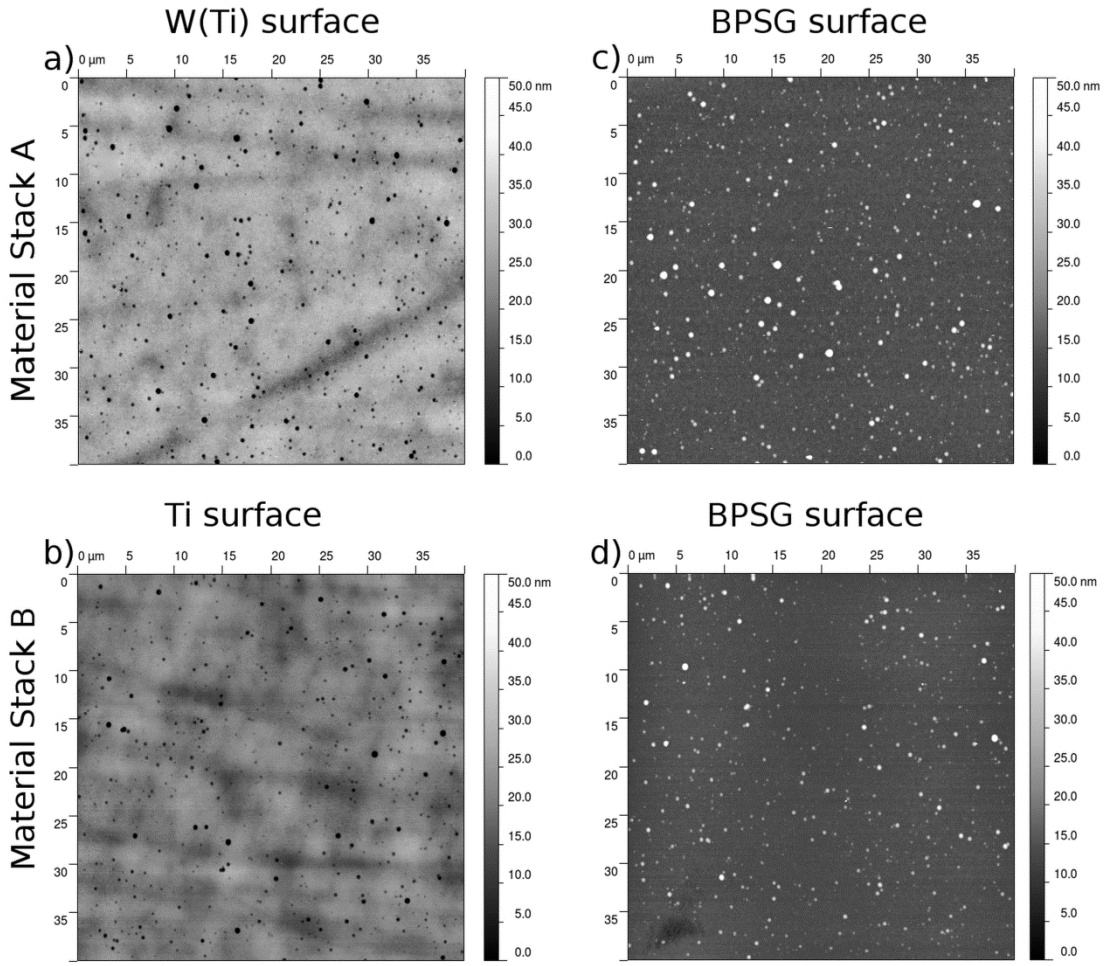

Figure 5 *AFM surface topography for material stack A and B for the metallization ((a), (b)) and for the BPSG fracture surfaces ((c), (d)). Note that the BPSG fracture surface is smoother than the metallic fracture surface. In all cases, bright or dark spots are revealed indicating nanometre sized small particles or cavities at the fracture surfaces with area densities of (a) 1.7%, (b) 1%, (c) 3.4% and (d) 3% for the corresponding AFM images.*

To look at the intact interface in more detail, EDX line scan measurements in the TEM were made. For material stack A (Figure 6(a)), no Ti enrichment at the interface is resolved, while for material stack B the 10 nm thick Ti interlayer can be clearly detected in the line scan (Figure 6(b)). More insight for material stack A, the layer system without the Ti interlayer, was gathered using the EDX measurements where the electron beam was scanned across a rectangular area (box measurements) at the interface. These box measurements were made and evaluated as described before in Section 2. The findings of these measurements were that the Ti content is higher at the interface than in the W(Ti) layer, see Table 1. This supports the suggested Ti enrichment at the interface. In Table 2, the Ti excess at the interface is depicted in atoms/nm^2. This enrichment would theoretically give an average Ti enrichment at the interface of (5 ± 1) atoms/nm^2 which would correspond to (0.6 ± 0.1) monolayers (see Appendix 1).

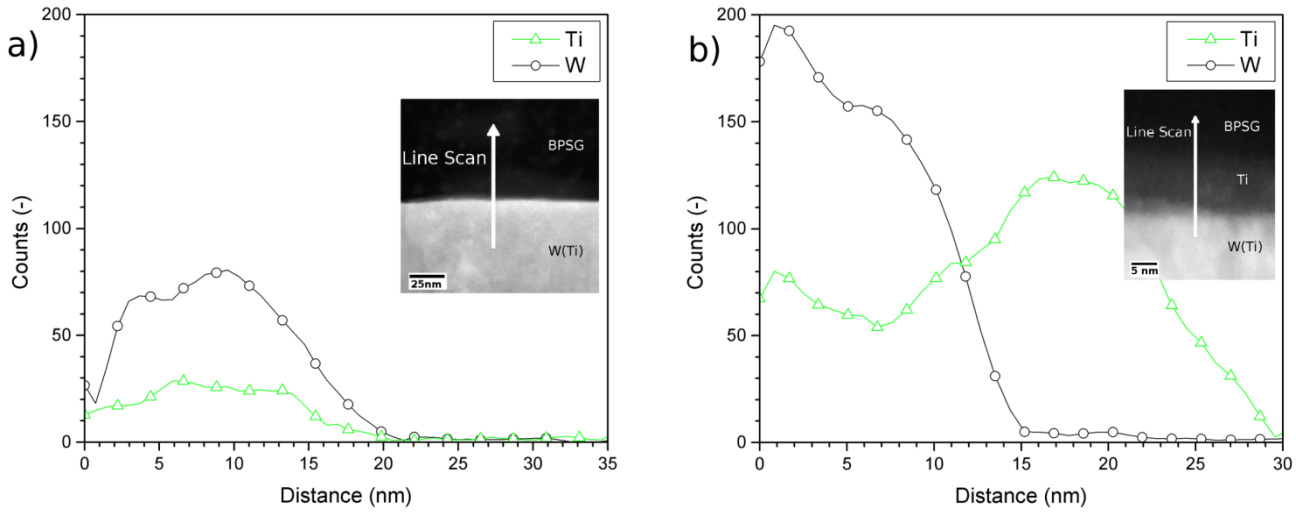

Figure 6 *EDX line scans across the interface for material stack A (a) and material stack B (b) acquired in STEM mode. Both line scans include the W-L and Ti-K profile. For material stack A seen in image (a), no Ti enrichment at the interface can be resolved in both the HAADF image and the line scan profile. In the HAADF image in (b), the 10 nm Ti interlayer is slightly visible as a light grey area between the W(Ti) and the BPSG and in the line scan profile it is clearly visible as an increase in the Ti signal. The arrow head in the image gives the direction of the line scan. In both cases, from the W(Ti) layer to the BPSG.*

Table 1 *Comparison of the concentration of Ti at the interface, with the standard deviation of the three measurements for each position, and in the W(Ti) layer. The Ti enrichment at the interface can be clearly seen.*

	Ti concentration (at%)				
Position	1	2	3	4	5
W(Ti)	18,5	20,7	20,7	19,3	20,0
Interface	23,2 ± 0,1	27,8 ± 2,9	33,3 ± 6,0	30,1 ± 4,4	34,5 ± 3,5

Table 2 *Number of excess atoms of Ti calculated using Equation (3) and the corresponding monolayer values at the interface. Calculation of monolayers see Appendix 1.*

Position	Excess atom concentration (atoms/nm^2)	Monolayer (-)
1	7	0.8
2	5	0.6
3	6	0.7
4	4	0.5
5	4	0.5
Average value ± standard deviation	5 ± 1	0.6 ± 0.1

4. Discussion

It is a well-known fact that a Ti interlayer, even in the sub-nanometre regime, serves as an adhesion promoter for different materials on glasses or ceramics [9,11,30]. It was shown by Rafalski et al. [7] and Russell et al. [9] that Ti or Cr incorporated into a Cu layer or a Cu/Ti or Cu/Cr bilayer deposited on a SiO_X strengthens the interface. More recently, Matoy et al. [16] investigated the adhesion properties of W(Ti) on SiO_X and pure W on SiO_X using micro-bending beams. They found an interface energy release rate of about 3 J/m^2 for pure W, which is about 40% less compared to W(Ti) (~4.5 J/m^2). This corresponds to the findings of Rafalski et al. [7] and Russell et al. [9], that Ti incorporated in a Cu layer strengthens the interface, because the Ti incorporated in the Cu layer migrates to the interface and there it reduces the SiO_X [9].

In our study, we analysed the material system W(Ti) on as-deposited BPSG and tried to answer the question how a pure Ti interlayer between those two layers affects the interfacial strength.

The findings for material stack A without the Ti interlayer (4.9 ± 0.2) J/m^2 are in accordance to the results of Matoy et al. [16] that W(Ti) on a SiO_X substrate layer possesses an adhesion of about 4.5 J/m^2. The evaluated interface strength values for both experimental approaches can be considered an upper boundary of the actual interface strength. That is because energy dissipating processes can occur in both experiments, such as plastic deformation in adjacent layers or other processes, which lead to a rise of the actual interface fracture energy.

The results from the 4-point-bending tests for material stack B with the 10 nm Ti interlayer show a significant promotion of the interfacial strengths. The interface energy release rate for material stack B (11.7 ± 0.4) J/m^2 was more than two times higher than the one for material stack A without the interlayer (4.9 ± 0.2) J/m^2. This is in accordance to the findings by Russel

et al. [9] for Cu/Ti bilayers and Cu(Ti) layers. They also found a factor of two for the difference in interfacial strength between Cu/Ti bilayers and a Cu(Ti) layer using a scratch test approach.

The factor of around two possibly arises from a potential excess of Ti adatoms at the BPSG fracture surface of material stack B with the 10 nm Ti interlayer compared to material stack A without the Ti interlayer. The higher density of Ti atoms at the interface in the case for the pure Ti interlayer compared to the W(Ti) interlayer, where the excess is only equivalent to (0.6 ± 0.1) monolayers, could provoke a stronger bonding to the as-deposited BPSG and hence increase the interface strength.

AFM measurements revealed that particles seem to stick to the BPSG surface of material stack A and B. Further, there were cavities found on the metallization fracture surface for both material stacks. The size of the cavities corresponds to the size of the particles found on the BPSG fracture surface. It seems that metallization residues stick to the BPSG fracture surface. The particles for both material stacks are in the range of several nm in height and the lateral size is from the µm regime down to the nm scale.

The AES analysis of material stack A without the Ti interlayer did not show any material residues present on the BPSG fracture surface, but C contamination was found. For material stack B with the Ti interlayer, it revealed the presence of Ti residues on the BPSG fracture surface. A possible reason why the AES measurement for material stack A is inconclusive about the metallization residues, which were found in the AFM measurements, could be that the noise in the spectra before sputtering is too high and that the Ti peak is below the background noise, especially caused by contamination of the fracture surface prior to the chemical analysis. This is supported by the EDX box measurements for material A where a Ti enrichment at the interface is seen but the Ti excess at the interface is not as significant as for the pure Ti interlayer, where several atomic layers of Ti are present. It only reaches an average Ti excess of (5 ± 1) atoms/nm^2 which corresponds to (0.6 ± 0.1) monolayers of Ti at the interface, which, however, could form Ti rich clusters rather than a uniform layer. Because of that we suggest that the particles found in the AFM measurements on the BPSG fracture surface of material stack A are metallic, most likely Ti-based or very small W(Ti) residues adhering to the BPSG substrate via a local Ti enrichment, i.e. Ti clusters. Similarly, the EDX-TEM line scans were also not able to reveal the Ti enrichment for material stack A. Only with the box measurements, a slight enrichment was detected. This Ti enrichment is equivalent to (0.6 ± 0.1) monolayers of Ti, compared to the reference measurements in the W(Ti) layer. The segregation of Ti to the interface could explain why there are particles

present on the fracture surface for material stack A, which are in the same height regime as the particles found for material stack B, and why the height for some particles surpasses 10 nm for material stack B, which is the Ti interlayer thickness. Possible explanations why segregation to the interface is happening could be that the equilibrium solubility of Ti in W is exceeded. The solubility reported in literature is less than 10% at 400 °C [31,32]. The W(Ti) layer is, according to the equilibrium solubility, oversaturated with the 20 at% Ti content used in this investigations and during the annealing treatment at 400°C, Ti most probably segregates to areas which are thermodynamically preferential, like grain boundaries, the interface and surface. The interface could be particularly favoured because it is the only source of oxygen for TiO_2 formation, like in the findings of Petrović et al. [33]. They illustrated that in a W(Ti) alloy, with 30 at% Ti, Ti segregates to the surface and reacts with the oxygen of the atmosphere and forms a TiO_2 monolayer even at room temperature. The formation of TiO_2 is an exothermic reaction with a formation enthalpy of -944 kJ/mol [34] and it is lower than the -910 kJ/mol [34] for SiO_2 at room temperature. So, the affinity of Ti to O could be an explanation for segregation of Ti to the interface. Furthermore, it was reported by Nussbaum et al. [35] that Ti segregates to the interface between Au and α-Al_2O_3, because Ti lowers the solid-solid interface energy between these two materials. This could also be a possible explanation for our W(Ti)/BPSG system.

Kottke et al. [36] found that Ti on a SiO_X layer in the as-deposited material is reducing the underlying oxide and forms a silicide phase at the interface. They also investigated Ti on a BPSG layer and could show that at the interface in principle the same reactions occur as for Ti on SiO_X. Further, a phosphorus rich interface layer forms, which, according to their findings, is the failing layer in their adhesion tests. The influence of annealing temperature was also investigated by them. There they could reveal that with higher annealing temperatures the silicide, oxide and phosphorus rich layer formation was increased. Their annealing temperatures were 600 °C and higher. Our samples were annealed only at 400 °C for 1 hour. The TEM investigations did not reveal silicide or oxide formation. However, as a small Ti enrichment is detected at the interface, it could be argued that in our case the onset of silicide, oxide and phosphorus rich layer formation may have occurred but not at such a significant extent as for 600 °C.

Finally, it is to mention that all experiments where performed with as-deposited BPSG, which is a very reactive form of BPSG. That is, as-deposited BPSG can strongly interact with its surrounding as shown in the investigations by Thorsness et al. [37]. Taking this into

consideration, the investigation of BPSG annealed at high temperatures could give completely different mechanical behaviour and chemical composition than presented here.

5. Conclusion

In this work, 4-point-bending tests were conducted to evaluate the interface strength of as-deposited BPSG to W(Ti), once with Ti interlayer and once without Ti interlayer. It could be shown that the material with Ti interlayer develops a much higher interface strength, with an interface energy release rate of (11.7 ± 0.4) J/m^2, than the material without it. In that case, an interface energy release rate of (4.9 ± 0.2) J/m^2 was determined for W(Ti) directly deposited on BPSG.

Chemical characterization of the fracture surfaces for both material stacks were done using EDX and AES measurements. According to the EDX measurements, failure occurred in both cases at the dielectric to metallization interface. AES measurements confirmed the EDX results but revealed that Ti residues are present on the BPSG fracture surface of material stack B, which were below the EDX detection limit. The chemical findings are supported by AFM surface topography information. Nanometre-sized particles are detected on the otherwise smooth BPSG fracture surface, while cavities of similar dimension are detected on the metallic fracture surfaces. This indicates that small Ti-based particles adhere to the BPSG surface. TEM studies performed at the internal interfaces prior to the mechanical testing revealed a subtle enrichment of Ti at the interface between BPSG and W(Ti).

Acknowledgement

B.V. wants to thank T. Detzel and J. Fugger of Infineon Technologies Austria AG for their support.

Funding

Part of this work was jointly funded by the Austrian Research Promotion Agency [FFG, Project No. 831163] and the Carinthian Economic Promotion Fund [KWF, contract KWF-1521|22741|34186].

Note

1. Calculated using CASINO v2.48 (2.4.8.1)

References

[1] Q. Ma, H. Fujimoto, P. Flinn, V. Jain, F. Adibi-Rizi, F. Moghadam, R.H. Dauskardt, in:, Mater. Res. Soc. Symp. - Proc., 1995.

[2] Q. Ma, J. Bumgarner, H. Fujimoto, M. Lane, R.H. Dauskardt, in:, Mater. Res. Soc. Symp. - Proc., 1997, pp. 3–14.

[3] R.H. Dauskardt, M. Lane, Q. Ma, N. Krishna, Eng. Fract. Mech. 61 (1998) 141.

[4] A. Kinbara, S. Baba, A. Kikuchi, T. Kajiwara, K. Watanabe, Thin Solid Films 171 (1989) 93.

[5] M. Lane, R.H. Dauskardt, N. Krishna, I. Hashim, J. Mater. Res. 15 (2000) 203.

[6] S. Varchenya, A. Simanovskis, S. Stolyarova, Thin Solid Films 164 (1988) 147.

[7] S.A. Rafalski, R.L. Spreitzer, S.W. Russell, T.L. Alford, J. Li, M. Moinpour, F. Moghadam, J.W. Mayer, in:, Mater. Res. Soc. Symp. - Proc., 1994, pp. 613–618.

[8] J.E.E. Baglin, Nucl. Inst Methods Phys. Res. B 65 (1992) 119.

[9] S.W. Russell, S.A. Rafalski, R.L. Spreitzer, J. Li, M. Moinpour, F. Moghadam, T.L. Alford, Thin Solid Films 262 (1995) 154.

[10] M.D. Kriese, N.R. Moody, W.W. Gerberich, Acta Mater. 46 (1998) 6623.

[11] G. Dehm, M. Rühle, H.D. Conway, R. Raj, Acta Mater. 45 (1997) 489.

[12] J. Cunningham, C. Fuller, C. Haywood, IEEE Trans. Reliab. R-19 (1970) 182.

[13] P.B. Ghate, J.C. Blair, C.R. Fuller, G.E. McGuire, Thin Solid Films Pap Present. Int Conf Met. Coat San Franc. Calif Apr 3-7 1978 53 (n.d.) 117.

[14] C.Y. Ting, M. Wittmer, Thin Solid Films 96 (1982) 327.

[15] S.D. McAdams, T.Y. Tsui, W.C. Oliver, G.M. Pharr, in:, MRS Proc., 1994.

[16] K. Matoy, T. Detzel, M. Müller, C. Motz, G. Dehm, Surf. Coat. Technol. 204 (2009) 878.

[17] P.G. Charalambides, J. Lund, A.G. Evans, R.M. McMeeking, J. Appl. Mech. Trans. ASME 56 (1989) 77.

[18] M.P. de Boer, M. Kriese, W.W. Gerberich, J. Mater. Res. 12 (1997) 2673.

[19] A. Bagchi, G. Lucas, Z. Suo, A. Evans, J. Mater. Res. 9 (1994) 1734.

[20] O. Jørgensen, A. Horsewell, B.F. Sørensen, J Mater Res 11 (1996) 2109.

[21] D.B. Marshall, A.G. Evans, J. Appl. Phys. 56 (1984) 2632.

[22] M.D. Kriese, W.W. Gerberich, N.R. Moody, J. Mater. Res. 14 (1999) 3007.

[23] E. Barthel, O. Kerjan, P. Nael, N. Nadaud, Thin Solid Films 473 (2005) 272.

[24] A.A. Volinsky, N.R. Moody, W.W. Gerberich, Acta Mater. 50 (2002) 441.

[25] R. Shaviv, S. Roham, P. Woytowitz, Microelectron. Eng. 82 (2005) 99.

[26] J.J. Wortman, R.A. Evans, J. Appl. Phys. 36 (1965) 153.

[27] R.P. Birringer, P.J. Chidester, R.H. Dauskardt, Eng. Fract. Mech. 78 (2011) 2390.

[28] J.A.S. Ikeda, Y.-M. Chiang, A.J. Garratt-Reed, J.B.V. Sande, J. Am. Ceram. Soc. 76 (1993) 2447.

[29] C. Scheu, J. Microsc. 207 (2002) 52.

[30] J. Yang, C. Wang, K. Tao, Y. Fan, J. Vac. Sci. Technol. Vac. Surf. Films 13 (1995) 481.

[31] S.V. Nagender Naidu, P. Rama Rao, eds., Phase Diagrams of Binary Tungsten Alloys, The Indian Institute of Metal, Calcutta, 1991.

[32] L. Kaufman, H. Nesor, Metall. Trans. A 6 (1975) 2123.

[33] S. Petrović, N. Bundaleski, D. Peruško, M. Radović, J. Kovač, M. Mitrić, B. Gaković, Z. Rakočević, Appl. Surf. Sci. 253 (2007) 5196.

[34] Collaboration: Scientific Group Thermodata Europe (SGTE), in:, Lehrstuhl für Theoretische Hüttenkunde, Rheinisch-Westfälische Technische Hochschule Aachen (Eds.), Pure Subst. Part 4 Compd. HgHg ZnTeg, Springer-Verlag, Berlin/Heidelberg, n.d., pp. 301–324.

[35] E. Nussbaum, H. Meltzman, W.D. Kaplan, J. Mater. Sci. 47 (2012) 1647.
[36] M. Kottke, J. Vac. Sci. Technol. B Microelectron. Nanometer Struct. 10 (1992) 1124.
[37] A.G. Thorsness, A.J. Muscat, J. Electrochem. Soc. 150 (2003) F219.

Appendix 1. Calculation of Ti monolayers:

The calculation of the number of monolayers, which the Ti excess at the interface in atoms/nm^2 corresponds to, was done the following way:

As Ti in its close-packed form possesses a hdp structure, we used the highest packing density of a hdp plane as a reference. This is the (0001) plane with a packing density of 78.5%. Assuming for simplicity, an atomic radius of r=150 pm for Ti and W, we can estimate how many atoms occupy an area of 1 nm^2.

One spherical atom requires a circular area of $r^2\pi$=0.071 nm^2. Thus, in 1 nm^2 fit (1 nm^2·0.785/0.071 nm^2) ~11 atoms. For an atomic concentration of 20 at% Ti and 80 at% W, this corresponds to about 2 Ti atoms and 9 W atoms.

The monolayers are calculated using the mentioned atomic distribution and the excess atomic concentration of Ti per nm^2 at the interface. The results of Ti monolayers at the interface are listed in Table 2.

Publication 2

Submitted to *Thin Solid Films*

Mechanical and chemical investigation of the interface between tungsten-based metallizations and annealed borophosphosilicate glass

B. Völker[1,2], W. Heinz[1], K. Matoy[3], R. Roth[3], J.M. Batke[4], T. Schöberl[5], M.J. Cordill[5] and G. Dehm[6]

[1] KAI - Kompetenzzentrum Automobil- und Industrieelektronik GmbH, Technologiepark Villach, Europastrasse 8, 9524 Villach, Austria

[2] Department Materials Physics, University of Leoben, 8700 Leoben, Austria

[3] Infineon Technologies AG, 9500 Villach, Austria

[4] Infineon Technologies AG, 93049 Regensburg, Germany

[5] Erich Schmid Institute of Materials Science, Austrian Academy of Sciences, Jahnstrasse 12, 8700 Leoben, Austria

[6] Max-Planck-Institut für Eisenforschung GmbH, 40237 Düsseldorf, Germany

Abstract

The focus of this study was on the interface between W-based metallizations and an annealed borophosphosilicate glass (BPSG) dielectric. W-based metallizations are often used in semiconductor devices because of their favourable properties as a diffusion barrier. The interface was characterized mechanically and chemically. For the determination of the interface energy release rate the 4-point-bending method was used. The fracture surfaces resulting from the 4-point-bending experiments were examined to determine the failing interface and the topography of the fracture surfaces. Chemical characterizations of intact interfaces were performed using an electron dispersive x-ray approach in a scanning transmission electron microscope to provide information why Ti incorporated in a W-layer improves the adhesion on annealed BPSG significantly compared to a pure W-layer.

Introduction

Semiconductor devices play an important role in everyday life. They usually consist of a multitude of layers of different materials. Hence, mechanical and chemical properties at the interface play an important role in such devices and need to be understood. Interfaces between metallic conductors and dielectric insulators are essential for the functionality of such devices. But such interfaces are usually mechanically weak [1–10] and prone to fail during service. A lot of effort has been put into understanding such interfaces and finding ways to improve the adhesion of interfaces between metals and dielectrics [5–7,11,12]. One approach consists of using interlayers of materials which are known to have a better adhesion than the base metallization, for instance Ti or Cr [6,7,11]. There is also the possibility to improve the adhesion by alloying the metallization layer with the previously mentioned elements [5–7], however, care has to be taken that the properties needed for the functionality of the device are maintained. Another possibility to improve the interface strength would be to modify the surface using ion beam irradiation as suggested by Baglin [12].

There are several different techniques to determine the interface strength of metal/dielectric interfaces, like scratch testing [13], nanoindentation with and without superlayer [14–16], double cantilever beam testing [17,18], superlayer tests [19], micro bending beams [5] and 4-point-bending tests [1,20,21]. Volinsky et al. [3] gave an overview of different techniques which are employed testing interfaces. All methods used for the mechanical characterization have some disadvantages. For instance, they can only be used to determine the interface strength for bi-layer systems and are not always suitable for multilayer systems. Some of the methods provide only a qualitative analysis of the interfacial adhesion, while a quantitative value for the interface energy release rate would be required for designing multi-layered structures. Therein lays the advantage of the 4-point-bending method. This method is one of a few which can not only be used to determine the interfacial strength for multilayer material systems, but it also provides a quantitative value for the interface energy release rate of the failing interface.

The interface of interest in this study is between a W-based layer, which contains Ti, and a borophosphosilicate glass (BPSG). This interface is commonly used in semiconductor devices, because the W(Ti) layer functions as a diffusion barrier layer [22]. The Ti incorporation is intended to improve the adhesion of the metallization layer in comparison to a pure W layer. This was revealed by Matoy et al. [5] who used a micro bending beam approach to determine the adhesion of W on SiO_X and W(Ti) on SiO_X. They found that the Ti incorporated in the W significantly improves adhesion compared to the pure W layer. Russel

et al. [6] showed similar results for Ti incorporated in a Cu layer on silicate based substrates. They observed that Ti segregates to the interface and concluded that this segregation promotes the interfacial strength compared to a pure Cu layer on silicate based substrates. A Ti segregation could also be detected by Petrović et al. [23]. They investigated the Ti segregation to the surface. In their study they demonstrated that even at room temperature after a sufficient amount of time the Ti migrates to the surface and reacts with the oxygen in the atmosphere forming a Ti-surface oxide.

In the present study the focus is laid on comparing the interface energy release rate of pure W films, Ti alloyed W films with a Ti content of 15 to 25 at% and a pure Ti layer on BPSG. Quantitative energy release rates are determined by 4-point-bending measurements. The fracture paths are determined by analysing the fracture surfaces using Auger electron spectroscopy (AES). The AES studies were used to identify the failing interface in the different multilayer structures and helped finding possible residues on the fracture surfaces. In addition, on top of all W or W(Ti) films an Al film containing Si and Cu (hereafter: AlSiCu) was deposited to mimic device structures. Further understanding of the interface between the W(Ti)/BPSG layer was accomplished by chemical analysis of intact interfaces using electron dispersive X-ray spectroscopy (EDX) in the scanning transmission electron microscope (STEM), which was performed to identify possible elemental enrichments or depletions at the interface. To gain insight on the fracture topography the fracture surfaces were imaged using atomic force microscopy (AFM).

Experimental Details

In this study different interfaces between W-based metallizations and a dielectric, annealed BPSG, have been investigated. A schematic drawing illustrating the 4-point-bend samples and the material stacks can be found in Figure 1. The exact layer structures of all investigated material stacks with the different metallizations are listed in Table 1, together with the applied characterization techniques.

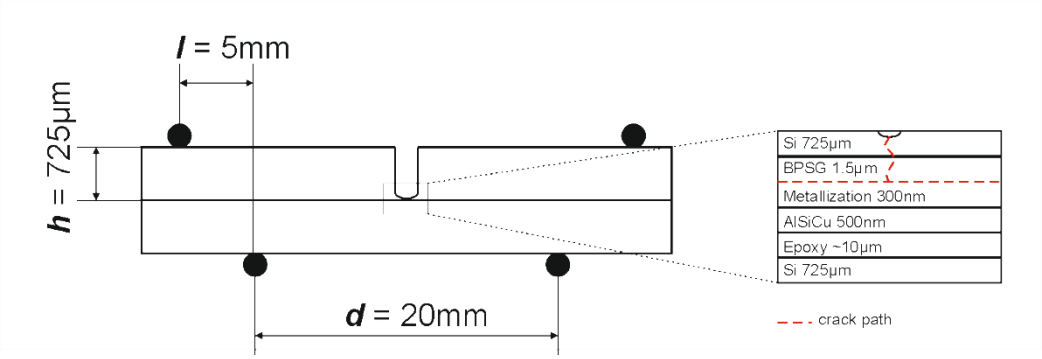

Figure 1 *Sketch of the 4-point-bending setup with the half sample height h, the distance between inner and outer loading pins l and d the distance between the two inner pins. The width of the sample in viewing direction is 7 mm and the length of the sample is 40 mm. The notch depth is 500 µm. The sample and measurement set-up are the same for all 4-point-bending samples. In the detail on the right hand side the principle layer structure is depicted. The crack initiates at the pre-notch, runs through the Si and the BPSG, and kinks into the interface between metallization (see Table 1) and BPSG.*

Table 1 *Material stacks and nominal Ti content for W(Ti) alloyed films. The layer sequences, layer thicknesses and the experiments performed on each material stack are reported. Note that Material Stacks 1a and 1b did not receive a surface treatment of the BPSG layer in contrast to all other material stacks. The following abbreviations are used: 4PB = 4-point-bending experiments, EDX = STEM EDX box measurements, AES = AES of the 4-point-bending fracture surfaces, AFM = AFM measurements of the 4-point-bending fracture surfaces (AFM).*

Material Stack	Layer structure	Surface treatment	Investigations
1a	Si 725 µm / BPSG 1.5 µm / W(20at%Ti) 300 nm / AlSiCu 500 nm	-	4PB, AES, AFM
1b	Si 725 µm / BPSG 1.5 µm / Ti 10 nm / W(20at%Ti) 300 nm/ AlSiCu 500 nm	-	4PB, AES, AFM
2	Si 725 µm /BPSG 1.5 µm / W 300 nm / AlSiCu 500 nm	X	4PB, AES, AFM
3a	Si 725 µm / BPSG 1.5 µm / W(15at%Ti) 300 nm / AlSiCu 500 nm	X	4PB, AES, AFM
3b	Si 725 µm / BPSG 1.5 µm / W(20at%Ti) 300 nm / AlSiCu 500 nm	X	4PB, EDX, AES, AFM
3c	Si 725 µm / BPSG 1.5 µm / W(20at%Ti) 300 nm / AlSiCu 500 nm	X	4PB, AES, AFM
4	Si 725 µm / BPSG 1.5 µm / Ti 300 nm / AlSiCu 500 nm	X	4PB, AES, AFM
5	Si 725 µm / BPSG 1.5 µm / W(20at%Ti) 50 nm	X	EDX

Mechanical testing of the different interfaces was done using the 4-point-bending approach following Ma et al. [1,24]. The sample geometry and experimental setup is shown in Figure 1. The sample manufacturing closely follows the details reported earlier [25] and is based on the sample preparation route developed by Shaviv et al. [26]. A 725 µm thick Si (100) wafer substrate was coated with a 1.5 µm thick BPSG layer produced by plasma enhanced chemical vapour deposition. After deposition of the BPSG layer the wafer was annealed at about 900°C. The wafers of Material Stack 2-5 got a surface treatment, as suggested by Baglin [12],

to enhance adhesion between material and BPSG, while the surfaces of Material Stacks 1a and b did not get such surface treatments. For Material Stack 1b, a 10 nm Ti interlayer was sputter deposited after the annealing. All other layer systems with the different metallizations (see Table 1) were directly deposited onto the annealed BPSG layer using magnetron sputtering. On top of the different metallization layers an AlSiCu layer was applied (except for material stack 5) to mimic real device structures and to enhance adhesion to the epoxy. The epoxy is needed to attach the second 725 µm Si wafer to the stack (see Figure 1) to create the 4-point-bending beam. In a final step most of the wafers, except Material Stack 5, were annealed at 400°C for one hour in an inert gas atmosphere.

The finished wafers were cut into the 4-point-bending geometry (7 mm x 40 mm) using a wafer saw with a diamond cutting wheel. Notches, with a width of about 36 µm and a depth of 500 µm, were cut into the Si side of the wafer with the deposited material stacks also using a wafer saw. Pure Si (100) counterparts having the same dimensions but no notch were glued with epoxy to a notched beam with EPO-TEK 375 epoxy. Finally, after curing the epoxy for 8 hours at 100 °C in vacuum of about $1x10^{-5}$ mbar, the edges of the samples were mechanically polished to remove epoxy residues and to obtain flat surfaces.

To determine the interface strength 4-point-bend testing was performed on a Kammrath & Weiss bending module with a crosshead speed of 0.1 µm/s. For an experiment to be considered as valid, the crack had to kink on both sides of the interface, as indicated in Figure 1, and the recorded load-displacement curve had to develop a plateau, as can be seen in Figure 2. When both requirements are met, the plateau load can be used to evaluate an interface energy release rate G_i according to the following equation:

$$G_i = \frac{21\left(1-\nu^2\right)P^2 l^2}{16Eh^3b^2} \qquad (Eq.1)$$

which has been employed by Ma et al. [1]. Here b denotes the sample width, h the half sample height, l the distance between inner and outer pins, $\nu=0.28$ the Poisson's ratio for Si (100) [27] and $E=130\ GPa$ the Young's modulus of Si (100) [27].

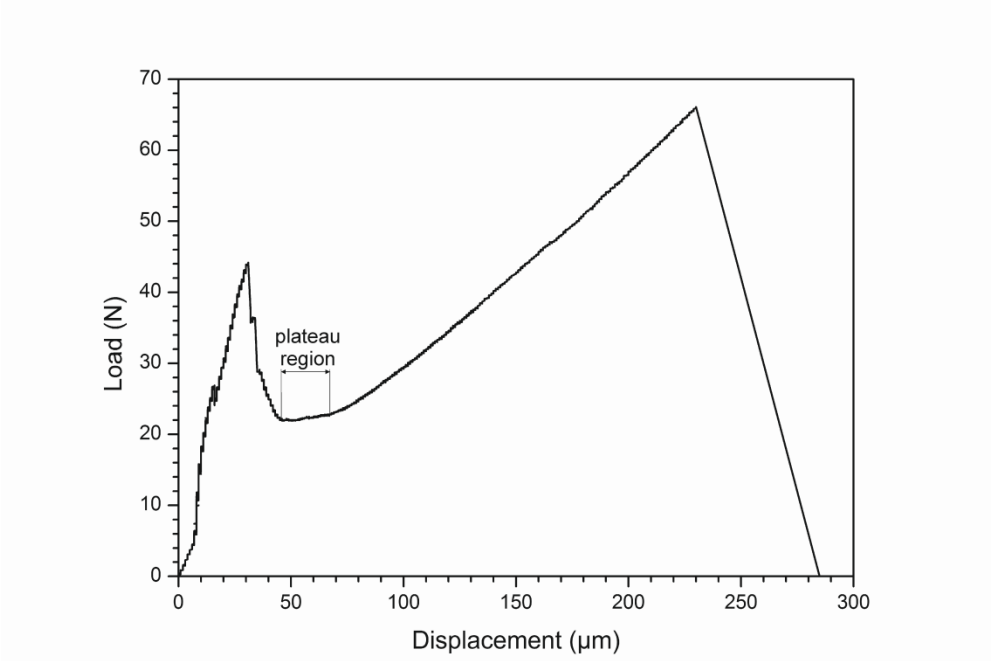

Figure 2 *Example of an experimental 4-point bending load-displacement curve showing the load plateau regime where the crack moves along. This value is used to determine the interface energy release rate according to Equation 1.*

The statistical error of the measurements was deduced using the standard deviation *s* as follows:

$$s = \sqrt{\left(\frac{1}{n-1}\right)\sum_{i=1}^{n}(x_i - \bar{x})^2} \quad \textit{(Eq.2)}$$

Here, n represents the number of values, x_i the observed value and $\bar{x}$ the mean value. Identification of the failing interfaces was carried out on the fracture surfaces of the 4-point-bending samples using AES. The AES measurements were performed on a PHI Scanning Auger Nanoprobe, at an acceleration voltage of 5 kV. Investigations of the fracture surfaces were made using AFM. The instrument used was a Digital Instruments (Veeco) scanning probe microscope Dimension 3100 combined with a Nanoscope III controller, in tapping mode.

Determination of a possible Ti enrichment was done on an intact W(Ti)/BPSG interface. Material Stacks 3b and 5 (see Table 1) were used for the investigations. Note that the two material systems differ by a 400 °C anneal for 3b, which was omitted in the case of Material Stack 5. For the EDX measurements cross section samples were prepared by conventional sample preparation routes using grinding, dimpling and final Ar-ion thinning to obtain

electron transparent samples. EDX area (box) measurements were performed on a JEOL 2100F image-side C_S-corrected microscope in scanning mode following the guide lines of Ikeda et al. [28] and Scheu [29]. The size of the measurement box was about 40 nm in length and around 5 nm in height. To get enough signal counts in the EDX spectra a measurement time of 180 s was chosen. During the measurement the beam was constantly scanned across the box to prevent beam damage and to average the signal over the region of interest. Five measurements have been performed for each interface: one in the W(20at%Ti) layer and one in the BPSG about 30 nm away from the interface, as reference measurements. The remaining three box measurements were executed on areas containing the interface. Subsequently, the background of the EDX spectra was subtracted and Gauss peaks were fitted to the Ti-K_α and W-L_α peaks. The area under these peaks was determined and used to calculate the Ti excess at the interface. A more detailed description of the evaluation can be found in Völker et al. [25]. These results were used to evaluate the Ti excess concentration Γ_{Ti} in atoms/nm^2 according to Ikeda et al. [28]

$$\Gamma_{Ti} = \Delta C_{Ti} \rho_V d \quad \textit{(Eq.3)}$$

In Equation 3, ΔC_{Ti} represents the Ti excess concentration at the interface, ρ_V the atomic density (atoms per unit volume) and d the W(20at%Ti) layer contribution to the height of the entire measurement box at the interface. The calculated excess concentration Γ_{Ti} was then used to estimate the number of monolayers the Ti concentration corresponds to. A closed-packing like in the basal plane of Ti was assumed. For more details see Völker et al. [25]

Results

A comparison of the results of the 4-point-bending experiments for Material Stacks 1a (5.9±0.3) J/m^2 and 1b (5.2±0.6) J/m^2, the W(20at%Ti) on the annealed BPSG without and with Ti interlayer, show no difference in interface strength, see Figure 3. This means that there is no influence of the Ti interlayer on the adhesion strength for a W(20at%Ti) on annealed BPSG. The investigations of Material Stacks 3a-c showed that the variation of the Ti content, in the regime of 15-25 at%, in a W layer does not influence the adhesion for these material systems significantly, see Figure 3. All three systems present almost the same interfacial strength, Material Stack 3a (6.1±0.6) J/m^2, 3b 5.8 J/m^2 [5.5 J/m^2 and 6.0 J/m^2] and 3c 6.3 J/m^2 [6.6 J/m^2 and 6.0 J/m^2]. For Material Stacks 3b and c no standard deviation is

given because only two samples for each material system could be used to evaluate an interface energy release rate. Both experimental values are reported in these cases in the square brackets next to the mean value. The evaluated interface energy release rate for these three systems also corresponds to the one measured for Material Stack 4, the pure Ti layer on annealed BPSG, with (6.2±0.4) J/m^2. But when compared to the interfacial adhesion of Material Stack 2, the pure W layer, of about (3.1±0.5) J/m^2, it can be clearly seen that the Ti incorporated in the W layer, Material Stacks 3a-c, promotes the adhesion significantly, see also Figure 3.

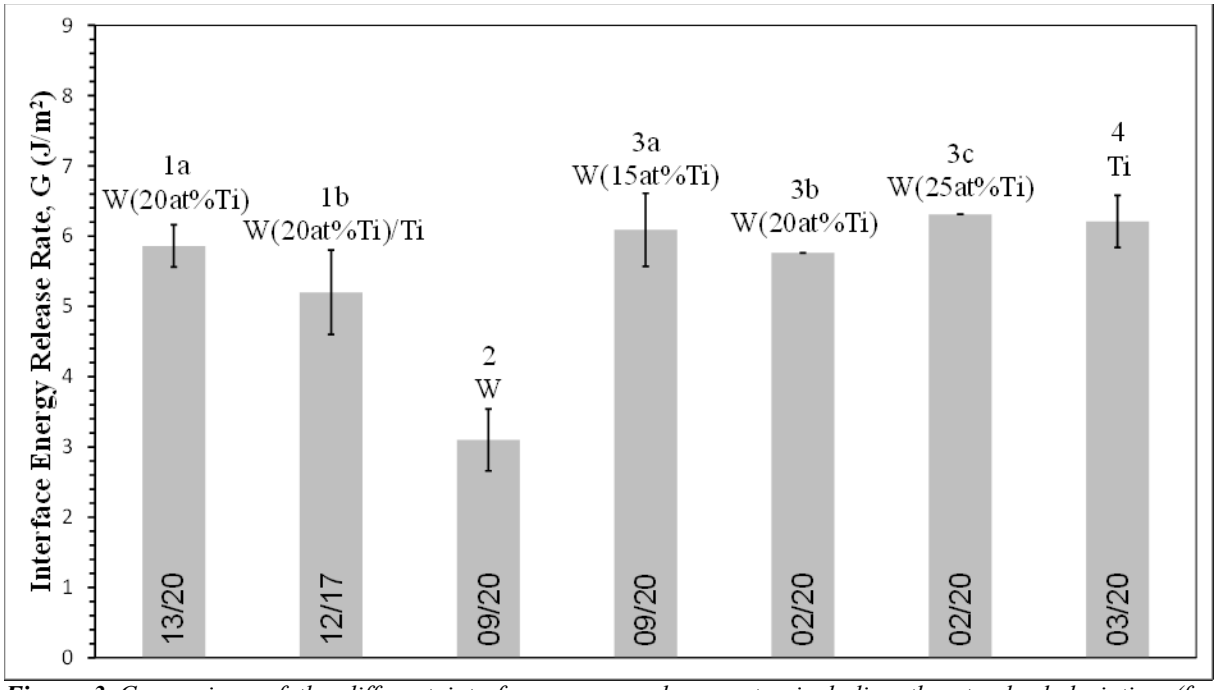

Figure 3 *Comparison of the different interface energy release rates including the standard deviation (for samples where only two specimens could be used to evaluate an interface energy release rate, no standard deviation was calculated). Material Stacks 1a and b, without and with Ti interlayer; Material Stacks 3a-c, with the different Ti contents in the W(Ti) layer; Material Stack 2, the pure W layer; Material Stack 4; the pure Ti layer. It is clearly shown that Ti incorporated in a W layer improves the adhesion significantly compared to pure W. The numbers on the bottom of the bars indicate the ratio of successful tests/totally tested samples.*

Figure 4 and 5 show the AFM topography images and the AES spectra of the fracture surfaces for Material Stack 3b (W(Ti)/BPSG) and Material Stack 2 (W/BPSG). Material Stack 3b was chosen as a representative for all the metallizations containing Ti, because in principle they all gave the same result.

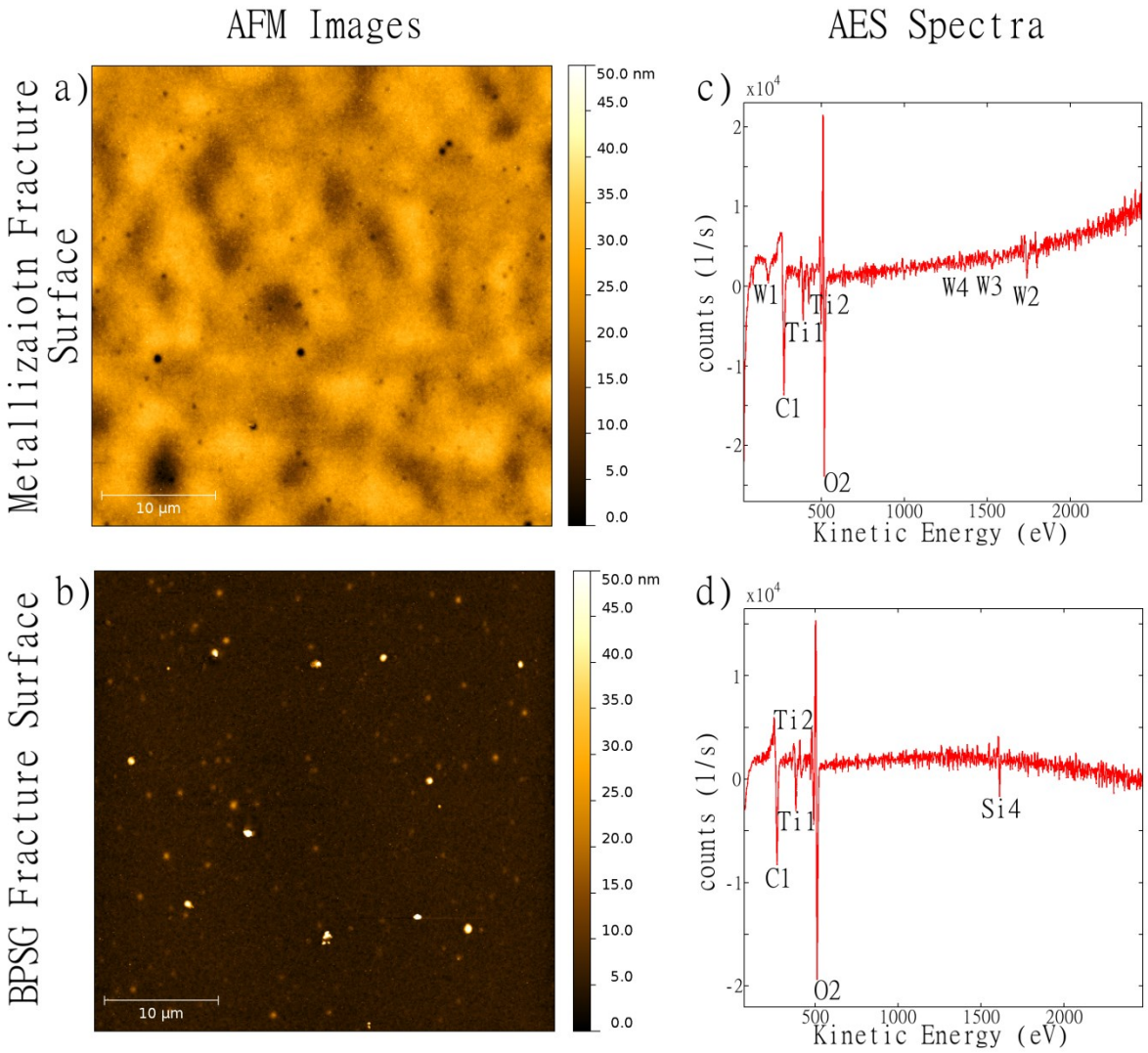

Figure 4 *Here as an example for all the Ti containing metallizations the AFM topography images ((a) and (b)) and the AES spectra ((c) and (d)) of the fracture surfaces for Material Stack 3b, the W(20at%Ti) sample, are depicted. All other Ti containing material stacks show a similar result. The bright spots on the BPSG fracture surface, seen in (b), correspond to elevated particles on the surface and the dark spots on the metallization fracture surface, in (a), to cavities of missing material. The AES spectrum in (d) reveals Ti residues on the BPSG fracture surface. No W is found on the surface of the BPSG fracture surface. This suggests that the particles found in the AFM in (b) are Ti based particles which are ripped out of the metallization during failure.*

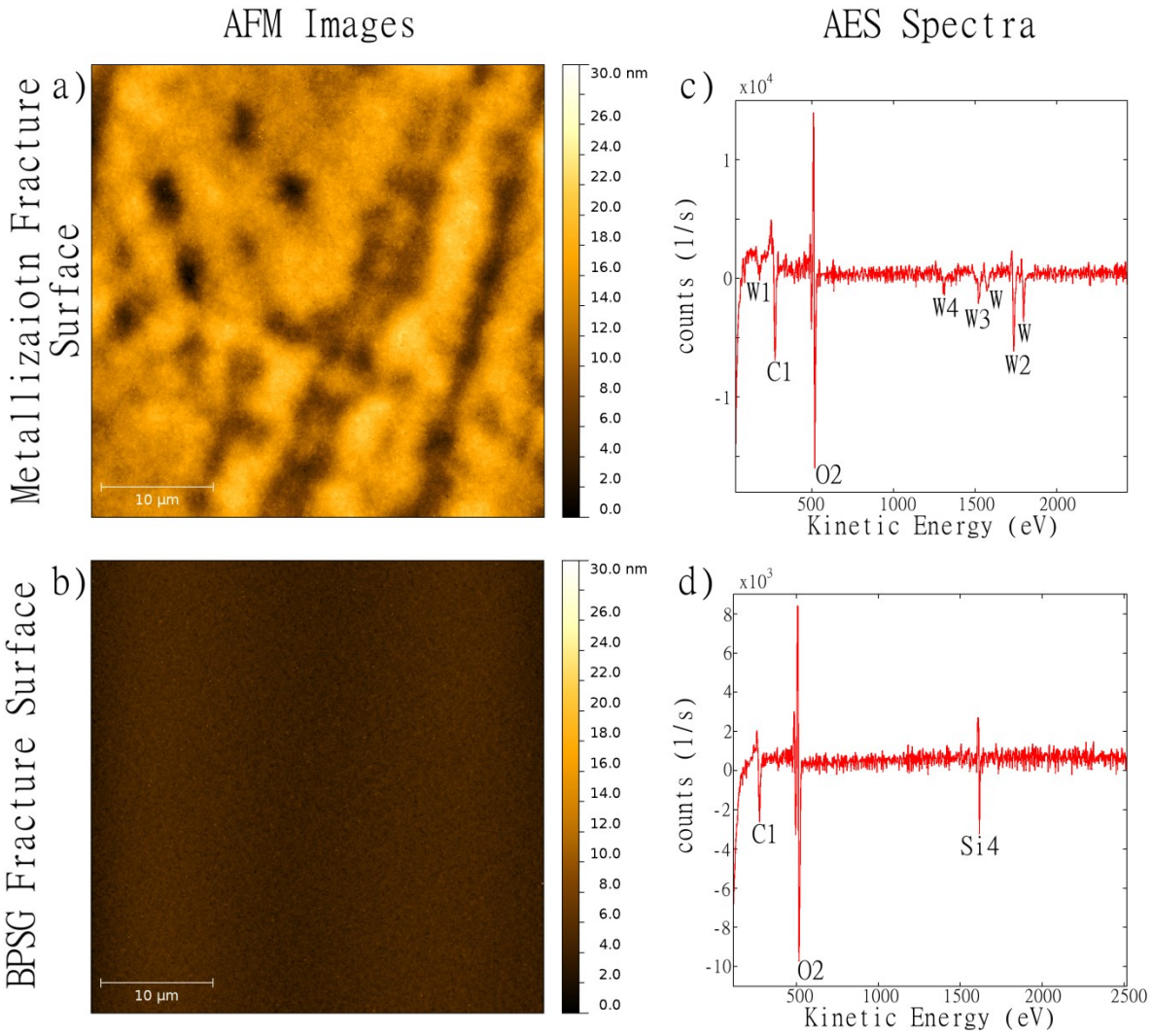

Figure 5 *For comparison the AFM images and AES measurements of the fracture surfaces of Material Stack 2, the pure W-layer on annealed BPSG, are depicted. The AFM images of the fracture surfaces of Material Stack 2 ((a) and (b)) are smooth and devoid of cavities and particles observed for the Ti containing material stacks.*

The chemical analysis using AES of the 4-point-bending fracture surfaces for the different material stacks indicated that in all the cases the failing interface is between metallization and annealed BPSG (see Figures 4c, 4d, 5c and 5d). The AES measurements for Material Stack 3b, seen in Figure 4c and d, reveal that some Ti residues can be found on the BPSG fracture surface. This Ti-residue is also found on the BPSG fracture surfaces of all other material stacks, except for the pure W layer, which did not show any metallic residues on the BPSG fracture surface. Note that the C contamination (see Figure 4c, d, 5c, and 5d) found on all fracture surfaces, is a consequence of the ex-situ fracture testing under ambient conditions.

The structural analysis of the two fracture surfaces, the metallization side and the BPSG side, of the different material stacks, utilizing the AFM, shed some light on the fracture surface topography. It was revealed that all material systems containing Ti, either incorporated in the W layer or as pure Ti layer, have particles sticking to the BPSG fracture surface (see Figure

4b). The counterpart of the fracture surfaces, the metallization side, showed cavities (Figure 4a). These cavities and particles found on the fracture surfaces for the mentioned material stacks correspond in size and shape. So it seems that some metallization residues are torn out of the metallization and adhere to the BPSG fracture surface. The investigation of the fracture surfaces of Material Stack 2 (see Figure 5a and 5b), the pure W layer, does not show any particles on the BPSG fracture surface and hence, no cavities are found on the metallization side of the fracture surface. This coincides with the AES findings for the different metallizations containing Ti, see spectrum Figure 4d, that no W is present on the BPSG fracture surfaces of these material systems. This suggests that Ti-based particles are present at the interface between metallization and BPSG and they adhere to the BPSG. The roughness of the metallization fracture surfaces found in the AFM measurements for all material stacks, seen in Figure 4a and 5a, are probably because of the relaxation of intrinsic stresses after the 4-point-bending experiment, due to the loss of the support of the Si substrate.

The results of the EDX investigations of intact interfaces in STEM can be found in Table 2. For Material Stack 3b, W with 20 at% Ti incorporated in the W layer, and the final 400 °C anneal a Ti enrichment at the interface was found. This enrichment comprises of 4±2 Ti excess atoms/nm^2, which corresponds to a 0.6±0.1 monolayer of Ti at the interface. These findings suggest that there is not a closed monolayer of Ti at the interface but probably Ti clusters. If the same material stack is created without the final 400 °C anneal then no significant increase in Ti concentration was found at the interface with 1±1 Ti excess atoms/nm^2, which corresponds to a 0.3±0.1 Ti monolayer, coinciding with a the overall Ti content of ~20 at%, indicating very little Ti segregation during deposition.

Table 2 *Results from the STEM/EDX measurements of Ti enrichment at the interface.*

Material Stack	Excess Ti concentration at the interface [atoms/nm^2]	Corresponding Ti monolayer at the interface [-]
3b annealed	4±2	0.6±0.1
5 not annealed	1±1	0.3±0.1

Discussion

It is a well-known fact that Ti promotes adhesion and several different investigations address this matter [6,7,11,25,30]. Even very thin films of Ti, as shown by Dehm et al. [11], can strengthen the interface. Furthermore, in an earlier study [25] it was revealed that on an as-deposited BPSG a Ti interlayer has a significant impact on the adhesion of a W(20at%Ti)

layer. This was also found for Cu on a BPSG layer by Russel et al. [6]. In this study the influence of a Ti interlayer on the adhesion of W(20at%Ti) on annealed BPSG is investigated. In the case of annealed BPSG it seems that the Ti interlayer does not have any additional impact. For Material Stack 1a, without the Ti interlayer, the 4-point-bending experiments gave an interface strength of (5.9±0.3) J/m^2 and for Material Stack 1b, with the Ti interlayer, (5.2±0.6) J/m^2 (see Figure 3). Within the accuracy of the 4-point-bending fracture test there is no measureable difference between these two sample types. Hence, the Ti interlayer does not further enhance the interface adhesion strength. This suggests that the significant improvement of the interface strength in the earlier investigation can be considered an effect of the as-deposited state of the BPSG. The findings of Thorsness and Muscat [31] support this, they revealed that as-deposited BPSG is very reactive. Furthermore, they could show that the formation of hydroxyl groups on the surface and in the layer traps water absorbed from the surroundings. These hydroxyl groups might be the reason that in the as-deposited state the BPSG layer is able to react more with the Ti and increase the interfacial adhesion significantly. During the annealing process of BPSG at around 900 °C trapped water is removed and the BPSG layer densifies. Hence, interfacial reactions between Ti and the BPSG could be reduced, which would corresponds to the lower energy release rate of (5.2±0.6) J/m^2 of this study compared to (11.7±0.4) J/m^2 of Ti on as-deposited BPSG in an earlier study of us [25].

The results further propose that the surface treatment of Material Stacks 2-5 during the sample production does not have an influence on the interface strength. If the interface energy release rates of Material Stacks 1a, (5.9±0.3) J/m^2, and 3b, 5.8 J/m^2, are compared, there does not seem to be any influence of the surface treatment on the interface strength.

The investigation of the W-based metallization layers, with a Ti content variation between 15-25 at%, emphasized that there seems to be no difference in the interface strength for the different film systems. It was also revealed that the Material Stacks 3a-c, the different W(Ti) layers on annealed BPSG, develop an interface energy release rate in the magnitude of that of Material Stack 4, the pure Ti on BPSG. This denotes that a content of 15 at% of Ti is enough to promote the adhesion of a W-layer nearly to the same value as a pure Ti layer on annealed BPSG does. Therefore, some kind of Ti enrichment at the interface is occurring. This is further shown by the fact that Material Stack 2, the pure W system, has an adhesion energy of (3.1±0.5) J/m^2, which is significantly lower than that of Material Stacks 3a-c (G_i of about 6 J/m^2). Hence, the Ti addition in the layer gives a pronounced increases in interfacial adhesion for W. This was also found by Matoy et al. [5] using a micro bending beam approach. They

showed for W on SiO_X an interfacial strength of 2.86 J/m^2. Furthermore, they investigated the interface between W(Ti) on SiO_X. For this interface they found an interface energy release rate of 4.8 J/m^2. The results in their investigation and those presented here coincide very well. It seems that these new results are quite reasonable and do not have too much influence of plastic deformation in adjacent layers during 4-point-bend testing. Still, the values for the interface energy release rates should be viewed as upper boundaries for the real interface strength, because there still could be some plastic deformation present and/or other energy dissipating processes, which lead to higher measured interface energy release rates than the actual interface strength.

The increase in interface strength by the addition of Ti suggests that it migrates to the interface. This was found by Russel et al. [6] during their investigation of Cu on different silicate based substrates. They found that Ti incorporated in the Cu layer migrates to the interface and increased the interfacial strength significantly compared to the pure Cu layer. In a previous study [25], it was shown by STEM/EDX studies that a Ti enrichment at the interface between W(20at%Ti) and as-deposited BPSG occurred. The AES findings (Figure 4d) support the possibility of Ti enrichment at the interface with the findings of Ti residues on the BPSG fracture surface for the Material Stack 3b. This is further supported by the AFM measurements, revealing particles, which seem to be torn out of the metallization fracture surface and adhere to the BPSG fracture surface, see Figure 4b. If the AFM and AES results are combined these particles seem to be Ti-based particles. At the moment the possibility that W is present in these particles cannot be excluded and that the amount of it is just too low to be detected with AES (because AES is more sensitive to light elements). However, for the pure W on annealed BPSG the AFM and AES results of the fracture surfaces (Material Stack 2, Figure 5a and 5b) show no particles and no cavities but rather smooth fracture surfaces. The AES analysis (Figure 5d) did not show any presence of metallization residues on the BPSG fracture surface of Material Stack 2. Hence, it is suggested that no W is present. This concludes that only Ti based particles are present on the fracture surfaces of Material Stacks 1a-b, 3a-c and 4.

The EDX measurements in the STEM give the final evidence that there is Ti enrichment at the interface. These measurements revealed that there is excess Ti at the intact interface of a Material Stack 3b, W(20at%Ti) with the final 400 °C anneal. Also, it could be shown that the Ti enrichment is less than one monolayer, suggesting that the Ti forms clusters.

Concluding, it seems as if the Ti enrichment at the interface between a W(Ti) and BPSG layer is in the form of clusters or particles near the interface, rather than a continuous layer.

Furthermore, it seems that the enrichment of Ti at the interface is occurring during the final 400 °C anneal. Because, the sample without the final 400°C anneal did not show a significant increase in Ti content at the interface. This is supported by the W-Ti equilibrium phase diagram, which reports a Ti solubility in W at 500°C of around 10 at% [32]. So in the case of the material stack with a maximum temperature during production of only 400 °C and with 20 at% of Ti in W layer it is obvious that the W(Ti) film is over saturated. Hence, it can be assumed that during the 400°C anneal the system tries to balance itself, leading to segregation of Ti to energetically more favourable sites like grain boundaries, surfaces and interfaces. This is supported by the findings of Petrović et al. [23]. They showed that even at room temperature Ti segregates to the surface of a W(Ti) layer, if given the sufficient amount of time, to form a Ti-oxide layer at the surface.

Conclusion

This study was performed to investigate the interface between a W-based metallization and an annealed BPSG dielectric layer. It was shown that for all material stacks investigated by the 4-point-bending method the failing interface is the one between the metallization and the dielectric, annealed BPSG. It was also revealed that Ti incorporated in a W layer on BPSG enhances the interface strength significantly, with an interface energy release rate of about 6 J/m^2, if compared to a pure W layer with about (3.1±0.5) J/m^2. Furthermore, it could be shown that a Ti content of 15 at% in the W layer, with an interface strength of (6.1±0.6) J/m^2, seems to be sufficient to promote the adhesion in the same way as 20 at% (5.8 J/m^2), 25 at% Ti (6.3 J/m^2), or even a pure Ti layer ((6.2±0.4) J/m^2). The chemical investigation of the intact interface by STEM EDX studies revealed that Ti enriches the interface in a W(20at%Ti) layer, due to the final 400 °C anneal, to 4±2 Ti excess atoms/nm^2. In contrast, the W(20at%Ti) sample without the final 400 °C anneal is lacking a pronounced enrichment of Ti at the interface with an excess concentration of only 1±1 atoms/nm^2.

Acknowledgement

B.V. would like to thank R. Pippan for the discussions and T. Detzel and J. Fugger of Infineon Technologies Austria AG for their support. Part of this work was jointly funded by the Austrian Research Promotion Agency (FFG, Project No. 831163) and the Carinthian Economic Promotion Fund (KWF, contract KWF-1521|22741|34186).

References

[1] Q. Ma, H. Fujimoto, P. Flinn, V. Jain, F. Adibi-Rizi, F. Moghadam, R.H. Dauskardt, in:, Mater. Res. Soc. Symp. - Proc., 1995.

[2] Z. Cui, G. Dixit, L. Xia, A. Demos, B.H. Kim, D. Witty, H. M'Saad, R.H. Dauskardt, in:, AIP Conf. Proc., 2005, pp. 507–511.

[3] A.A. Volinsky, N.R. Moody, W.W. Gerberich, Acta Mater. 50 (2002) 441.

[4] S. Venkataraman, D.L. Kohlstedt, W.W. Gerberich, J. Mater. Res. 11 (1996) 3133.

[5] K. Matoy, T. Detzel, M. Müller, C. Motz, G. Dehm, Surf. Coat. Technol. 204 (2009) 878.

[6] S.W. Russell, S.A. Rafalski, R.L. Spreitzer, J. Li, M. Moinpour, F. Moghadam, T.L. Alford, Thin Solid Films 262 (1995) 154.

[7] S.A. Rafalski, R.L. Spreitzer, S.W. Russell, T.L. Alford, J. Li, M. Moinpour, F. Moghadam, J.W. Mayer, in:, Mater. Res. Soc. Symp. - Proc., 1994, pp. 613–618.

[8] C. Zhou, P. Su, M.A. Korhonen, C.-Y. Li, in:, Mater. Res. Soc. Symp. - Proc., 1998, pp. 377–381.

[9] M.J. Cordill, D.F. Bahr, N.R. Moody, W.W. Gerberich, IEEE Trans. Device Mater. Reliab. 4 (2004) 163.

[10] S. Varchenya, A. Simanovskis, S. Stolyarova, Thin Solid Films 164 (1988) 147.

[11] G. Dehm, M. Rühle, H.D. Conway, R. Raj, Acta Mater. 45 (1997) 489.

[12] J.E.E. Baglin, Nucl. Inst Methods Phys. Res. B 65 (1992) 119.

[13] M.P. de Boer, M. Kriese, W.W. Gerberich, J. Mater. Res. 12 (1997) 2673.

[14] D.B. Marshall, A.G. Evans, J. Appl. Phys. 56 (1984) 2632.

[15] M.D. Kriese, W.W. Gerberich, N.R. Moody, J. Mater. Res. 14 (1999) 3007.

[16] M.D. Kriese, W.W. Gerberich, N.R. Moody, J. Mater. Res. 14 (1999) 3019.

[17] J.M. Whitney, C.E. Browning, W. Hoogsteden, J. Reinf. Plast. Compos. 1 (1982) 297.

[18] E. Barthel, O. Kerjan, P. Nael, N. Nadaud, Thin Solid Films 473 (2005) 272.

[19] A. Bagchi, G. Lucas, Z. Suo, A. Evans, J. Mater. Res. 9 (1994) 1734.

[20] P.G. Charalambides, J. Lund, A.G. Evans, R.M. McMeeking, J. Appl. Mech. Trans. ASME 56 (1989) 77.

[21] R.H. Dauskardt, M. Lane, Q. Ma, N. Krishna, Eng. Fract. Mech. 61 (1998) 141.

[22] M.A. Nicolet, M. Bartur, J. Vac. Sci. Technol. 19 (1981) 786.

[23] S. Petrović, N. Bundaleski, D. Peruško, M. Radović, J. Kovač, M. Mitrić, B. Gaković, Z. Rakočević, Appl. Surf. Sci. 253 (2007) 5196.

[24] Q. Ma, J. Bumgarner, H. Fujimoto, M. Lane, R.H. Dauskardt, in:, Mater. Res. Soc. Symp. - Proc., 1997, pp. 3–14.

[25] B. Völker, W. Heinz, K. Matoy, R. Roth, J.M. Batke, T. Schöberl, C. Scheu, G. Dehm, Philos. Mag. (2014) DOI: 10.1080/14786435.2014.913108.

[26] R. Shaviv, S. Roham, P. Woytowitz, Microelectron. Eng. 82 (2005) 99.

[27] J.J. Wortman, R.A. Evans, J. Appl. Phys. 36 (1965) 153.

[28] J.A.S. Ikeda, Y.-M. Chiang, A.J. Garratt-Reed, J.B.V. Sande, J. Am. Ceram. Soc. 76 (1993) 2447.

[29] C. Scheu, J. Microsc. 207 (2002) 52.

[30] S.D. McAdams, T.Y. Tsui, W.C. Oliver, G.M. Pharr, in:, MRS Proc., 1994.

[31] A.G. Thorsness, A.J. Muscat, J. Electrochem. Soc. 150 (2003) F219.

[32] S.V. Nagender Naidu, P. Rama Rao, eds., Phase Diagrams of Binary Tungsten Alloys, The Indian Institute of Metal, Calcutta, 1991.

Publication 3

Submitted to *Journal of Materials Research*

Following crack path selection in multi-film structures with weak and strong interfaces by in-situ 4-point-bending

B. Völker[1,2], S. Venkatesan[3], W. Heinz[1], K. Matoy[4], R. Roth[4], J.M. Batke[5], M.J. Cordill[6] and G. Dehm[3]

[1] KAI - Kompetenzzentrum Automobil- und Industrieelektronik GmbH, Technologiepark Villach, Europastrasse 8, 9524 Villach, Austria

[2] Department Materials Physics, Montanuniversität Leoben, 8700 Leoben, Austria

[3] Max-Planck-Institut für Eisenforschung GmbH, 40237 Düsseldorf, Germany

[4] Infineon Technologies AG, 9500 Villach, Austria

[5] Infineon Technologies AG, 93049 Regensburg, Germany

[6] Erich Schmid Institute of Materials Science, Austrian Academy of Sciences, Jahnstrasse 12, 8700 Leoben, Austria

Abstract

In this study the interfacial adhesion of Cu and TiN on an annealed borophosphosilicate glass (BPSG) was investigated. The two material systems under investigation are representatives for weak, Cu/BPSG, and strong, TiN/BPSG, interfaces. These interfaces were chosen to identify a difference in the fracture behaviour of weak and strong systems. To investigate this, an in-situ 4-point-bending approach was used. It was revealed that there is a discrepancy in the output of samples which fail along the interface of interest. Additionally a way to describe this result by using theoretical findings of earlier studies was proposed. The proposed reason is supported by the outcome of the in-situ 4-point-bending measurements.

Introduction

Interfaces are essential for the functionality of semiconductor devices. One such interface is between the dielectric (usually some kind of silicate glass) and metal based materials. But these interfaces have one disadvantage, they are rather weak [1–3]. Therefore, it is necessary to test these interfaces using one of the methods available to measure adhesion. A summary of the most common test methods, their advantages and disadvantages and suitability for certain material systems is found in a review by Volinsky et al. [3]. One of the methods described is nanoindentation induced delamination [4–6]. However, with this method it may be necessary to apply a compressive stressed over-layer on top to induce delamination of an interface [5–8]. Another method is the double cantilever beam test according to Barthel et al. [9]. With this method multilayer structures can be tested and an interface energy release rate can be calculated. Micro-bending beams are also often utilized for determining interface fracture energies, especially with in-situ experiments [10–12]. Another method which is often employed to determine an interface energy release rate for multilayer systems is the 4-point-bending test [13–15]. In the beginning it was developed to determine the interfacial adhesion for bi-layered material systems [13] but Ma et al. [14] modified the sample setup so it can be used to determine interface energy release rates in multilayer material systems. This method is widely used in semiconductor material systems to characterize metal/dielectric interfaces [14–20]. A disadvantage of this method which is also shared by other tests is that not necessarily the interface of interest fails in a multilayer system. Hence, it is necessary to identify the failing interface post-mortem. The output of successful tests which can be used to evaluate an interface energy release rate is also a challenge for the 4-point-bending technique. Earlier studies addressed this problem [19,20] and different approaches were proposed to enhance the output of evaluable samples. For instance, Birringer et al. [20] suggested that the geometry of the sample should be modified to raise the output or that the orientation of the silicon counterpart glued to the Si part with the material layers on them, is changed. Another method as proposed by Shaviv et al. [19] is varying the depth of the pre-notch.

In this study we investigated the material systems Cu and TiN on annealed borophosphosilicate glass (BPSG) with the 4-point-bending technique. The two systems Cu/BPSG and TiN/BPSG were chosen as representatives of a weakly and a strongly adhering interface. It is known from literature that Cu/SiO_X represents a weak interface [11,21] with an interface energy release rate of about 0.65 J/m^2 as reported by Matoy et al. [11]. Another result for a Cu/SiO_2 interface was reported by the measurements of Kriese et al. [21], but they also found that depending on the thickness of the Cu layer the determined interfacial adhesion

is changing. This can be ascribed to plastic deformation in the Cu layer, which is more suppressed in a thin film. Hence, it appears as if a thicker Cu layer adheres better than a thin one, but the plastic deformation leads to an overestimation of the energy release rate of the interface. Bulk Cu itself has a very high fracture energy, for instance an ultra-fine grained Cu, with a grain size in the region of 340 nm [22] shows a crack initiation energy of 7.6 kJ/m^2 [22].

The interface TiN/BPSG is representative of a strong interface, if compared to the Cu/BPSG interface. In literature an interface adhesion of about 8 J/m^2 [14] is reported for a TiN/SiO_2 system. TiN usually is a very brittle material with a fracture energy of about 20 J/m^2 [23,24]. In these two studies micro cantilever [23] and micro bending beam approaches [24] were used to determine the fracture energy of a TiN film in the thickness regime of a few μm.

The adhesion testing in our study was performed utilizing ex-situ and in-situ 4-point-bending approaches under an optical and in a scanning electron microscope (SEM). Experimental investigations in the optical microscope have been performed in earlier studies [14,15] to observe the crack initiation and subsequent crack propagation along the interface. In our investigation, additional in-situ testing in the SEM was performed to obtain a more detailed view on the crack behaviour and crack path selection during the experiment. This should allow for the determination of the failing interface while the experiment is ongoing without using any additional testing methods after the experiment. In addition, the in-situ observation may also shed light on the crack initiation and propagation which helps to understand the features of the load-displacement data. In the end an explanation shall be given why for the investigated material systems (Cu/BPSG and TiN/BPSG) certain interfaces are failing.

A lot of theoretical work has been performed to understand the crack behaviour and crack path selection for an interfacial crack [25–29]. An explanation of when a sample chooses to fail along the interface is given by He and Hutchinson [25]. They investigated the mechanical requirements for a crack in a bi-material layer system to kink onto the interface and fail along it. They found that, for a material system where there is no elastic mismatch between the two materials, the interface energy release rate has to be around ¼ or less of the fracture energy for the adjacent material, so that the crack can kink onto the interface between those two materials. In this study we did not have a bi-layered material system. Instead it was the aim of this study to investigate if it is possible to use the findings of He and Hutchinson [25] and employ them on a system consisting of several different films (here after termed multilayer).

In our case the thin film multilayer structure is confined between two thick silicon substrates which give the predominant elastic properties of the sample. It is assumed that it is possible to

use the findings of He and Hutchinson [25] for the 4-point-bending method and see if they can be used to answer pending questions.

Experimental

As base material a 725 µm thick Si (100) wafer was used for the two types of multi-layered samples investigated in this study. A BPSG layer with 1.5 µm thickness was deposited using plasma enhanced chemical vapour deposition (PECVD). Prior to deposition of subsequent layers the BPSG film was densified by an annealing treatment at ~900 °C. Following that, a 300 nm layer of one of the two metallization layers, Cu (Material Stack A) or TiN (Material Stack B), was deposited using magnetron sputtering. In a final deposition step the top layer of AlSiCu with 500 nm thickness was applied by magnetron sputtering. After completion of the deposition the wafers were annealed in an inert gas atmosphere at 400 °C for 1 hour. Detailed information on the different material stacks and a list of the performed experiments for each one is given in Table 1.

Table 1 *Layer structure of the two investigated material stacks and the investigations which have been performed for each material system.*
4PB…4-point-bending (ex-situ and in-situ); AES…Auger electron spectroscopy; EDX…energy dispersive x-ray spectroscopy in the TEM;

Material Stack	Substrate	Dielectric	First metallization	Top metallization	Investigations
A	Si 725 µm	BPSG 1.5 µm	Cu 300 nm	AlSiCu 500 nm	4PB, AES, EDX
B	Si 725 µm	BPSG 1.5 µm	TiN 300 nm	AlSiCu 500 nm	4PB, AES

The 4-point-bending sample preparation was based on one proposed in earlier studies [19,30]. After finishing the wafer production the samples were diced into the desired geometry by a wafer saw. The geometry of the samples is 7 mm by 40 mm. During dicing of the wafers the pre-notch with 500 µm depth and 36 µm width was introduced by the wafer saw. Afterwards, the wafer pieces were glued on a matching Si (100) counterpart with a thickness of 725 µm, using an EPO-TEK 375 epoxy. After the epoxy was cured for 8 hours at 100°C in vacuum, the edges of the samples were ground and polished to get scratch free edges for the optical and SEM in-situ experiments. Besides testing in-situ in the optical microscope and SEM, some samples were also tested ex-situ.

Ex-situ and in-situ 4-point-bending tests were performed using a Kammrath & Weiss bending module with a displacement rate of 0.1 µm/s. The spacing between the two inner loading pins was 20 mm and between the two outer pins 30 mm. The ex-situ and in-situ 4-point-bending

experiments under an optical microscope were performed until the sample completely fractured. The in-situ SEM measurements were stopped at 35 N to prevent failure of the sample and possible damage to the SEM by fractured parts of the sample. The SEM used for the in-situ experiments was a Zeiss LEO 1525, operated at an acceleration voltage of 20 kV.
The interface energy release rate was determined using the equation of Ma et al. [14]:

$$G_i = \frac{21(1-\nu^2)P^2 l^2}{16Eh^3 b^2}. \qquad (Eq.1)$$

Here, P is the load at the plateau region, at which the crack extends along the interface, b represents the 7 mm width of the sample, l the 5 mm distance between inner and outer pins, h the half sample height of about 725 µm, E the Young's modulus of 130 GPa for Si (100) [31] and $\nu=0.28$ the Poison's ratio of Si (100) [31]. The standard deviation of the interface energy release rate was determined using the following equation:

$$s = \sqrt{\left(\frac{1}{n-1}\right)\sum_{i=1}^{n}\left(x_i - \bar{x}\right)^2} \qquad (Eq.2)$$

In this case n denotes the number of samples, x_i the observed value and $\bar{x}$ the mean value. Determination of the failing interface for the ex-situ experiments was performed using Auger electron spectroscopy (AES) to analyse the fracture surfaces of tested 4-point-bending samples on a PHI Scanning Auger Nanoprobe, at an acceleration voltage of 5 kV. In addition, transmission electron microscopy (TEM) energy dispersive X-ray spectroscopy (EDX) investigation of the intact interface of material stack A was performed on a JEOL JEM-2200FS analytical TEM with a field emission gun at 200kV with in-column energy filter (Omega Filter), in scanning mode. The TEM sample was prepared following the conventional preparation route of grinding, dimpling and Ar-ion thinning.

Results

The ex-situ load-displacement curves shown in Figure 1 for Material Stack A, the Cu metallization, gives an interface energy release rate of (3.7±0.3) J/m^{2}according to Equation 1. For Material Stack B, with the TiN layer, the calculated interface energy release rate 8.4 J/m^2.

In this specific case the failing interface (TiN/BPSG) was confirmed by post-mortem AES studies. Other samples of Material Stack B showed no significant plateau region, even though the optical appearance of the fracture surfaces suggests that an interface is failing but not necessarily the interface of interest. By an optical analysis of the fracture surfaces it appeared that the delaminated interface is AlSiCu/epoxy. Rather surprising was the output of evaluable samples of the ex-situ experiments for Material Stacks A and B. For Material Stack A 15 of the 20 tested samples could be used to evaluate an interface energy release rate. In contrast to that, only 1 of 45 tested samples of Material Stack B gave a result for the TiN/BPSG interface. This is also the reason why for Material Stack B no standard deviation is provided. All interface energy release rate results from the ex-situ and in-situ 4-point-bending experiments are summarized in Table 2.

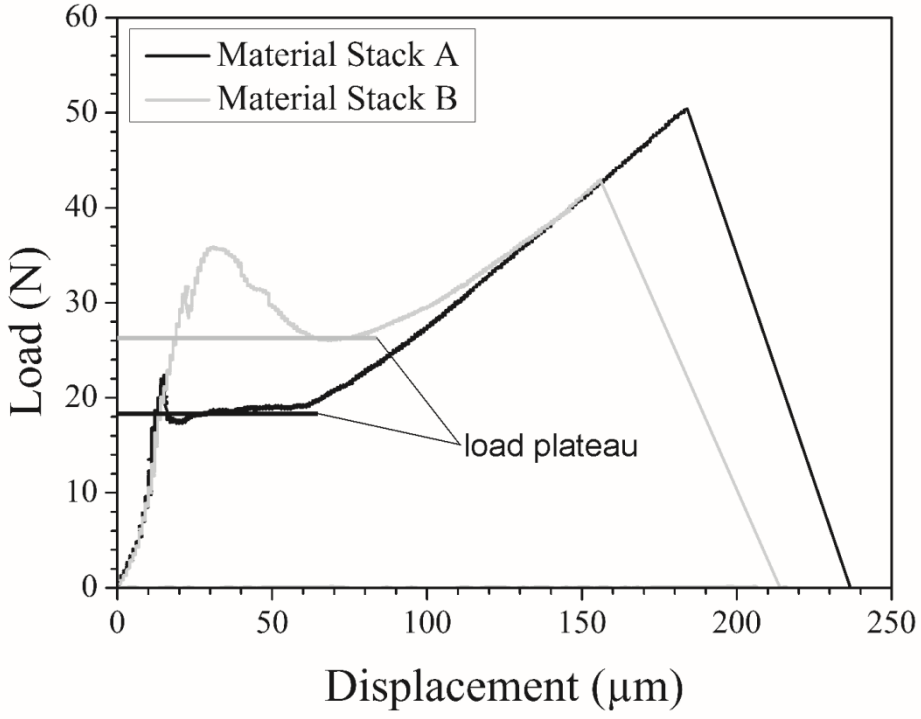

Figure 1 *Load-displacement curves of ex-situ 4-point-bending fracture experiments. The curve with the lower load plateau is for Material Stack A, the Cu metallization, and the curve with the higher load plateau for Material Stack B, the TiN layer.*

Table 2 *4-point-bending results for the different material stacks. The interface energy release rates for Material Stack A are in good agreement to each other. For Material Stack B only the ex-situ experiments gave one sample which could be used to evaluate an interface energy release rate of the TiN/BPSG interface. The failing interface was confirmed by post-mortem characterization.*

Material Stack	Investigation	Interface energy release rate (J/m^2)	Evaluable samples/tested samples
A	ex-situ	3.7±0.3	15/20
A	in-situ optical	3.2±0.6	05/08
A	in-situ SEM	2.9±0.2	04/09
B	ex-situ	8.4	01/45
B	in-situ optical	-*	00/05
B	in-situ SEM	-*	00/06

**Note that the in-situ tests of Material Stack B revealed failure along the AlSiCu top layer and epoxy and thus provided no values for the interface of interest.*

All in-situ 4-point-bending experiments under the optical microscope revealed crack initiation from the notch at the initial load drop in the load displacement curve. In the optical microscope it is also possible to distinguish if the crack kinks onto an interface or not, and if the crack extends only on one side or on both sides along the interface. However, the failing interface itself cannot be identified with the optical in-situ 4-point-bending experiment due to the limited resolution power.

In a next step the in-situ testing was performed in the SEM. During these in-situ tests the failing interface could be resolved, because the layers have significantly different contrast in the secondary electron image. For Material Stack A it is the Cu/BPSG which is depicted in Figure 2a. For Material Stack B the in-situ SEM observation (see Figure 2) resolves that not the TiN/BPSG interface is failing, but rather the interface between AlSiCu/epoxy is delaminating. It can be seen in Figure 2b, that the crack arrests at the interface between AlSiCu and epoxy. This would also explain the findings in some of the ex-situ and the in-situ optical measurements where it seems as if the sample is failing along an interface but not the interface of interest (TiN/BPSG).

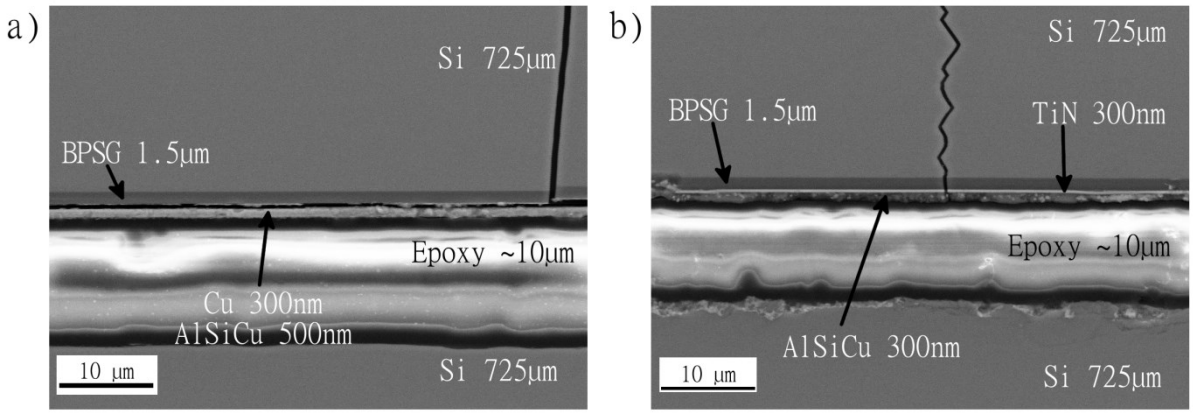

Figure 2 *Two in-situ SEM images after crack initiation for the two Material Stacks A and B are shown. (a) Image of the crack reveals fracture along the Cu/BPSG interface of Material Stack A. Note that the 300 nm Cu and 500 nm AlSiCu film appear as one layer in the image, which may be due to interdiffusion (see Fig. 4). Furthermore, it can be seen that some residues from the Al-Cu layer seem to stick to the BPSG. (b) shows the layer structure of Material Stack B. The image reveals that the crack does not kink onto the interface between TiN/BPSG. It rather propagates through the TiN and the AlSiCu layer and arrests at the AlSiCu/epoxy interface. All layers have significantly different contrast which permits their identification in the secondary electron image.*

The measured interface adhesion for material stack A in the in-situ SEM experiments was (2.9±0.2) J/m^2 which coincides with the results of the in-situ optical measurements (3.2±0.6) J/m^2 and the ex-situ experiments (3.7±0.3) J/m^2. For Material Stack B no interface energy release rate could be evaluated for the in-situ experiments, because the load-displacement curves showed no significant load plateau.

AES measurements for the fracture surfaces of Material Stack A, the Cu metallization, revealed that there was some Al present on the interface between Cu and BPSG, as shown in Figure 3a and b. Furthermore, identified AES, for the one sample of Material Stack B, the TiN system, the failing interface as the one between TiN/BPSG, see Figure 3c and d. Additionally, TiN residues were found on the BPSG fracture surface, as shown in Figure 3c.

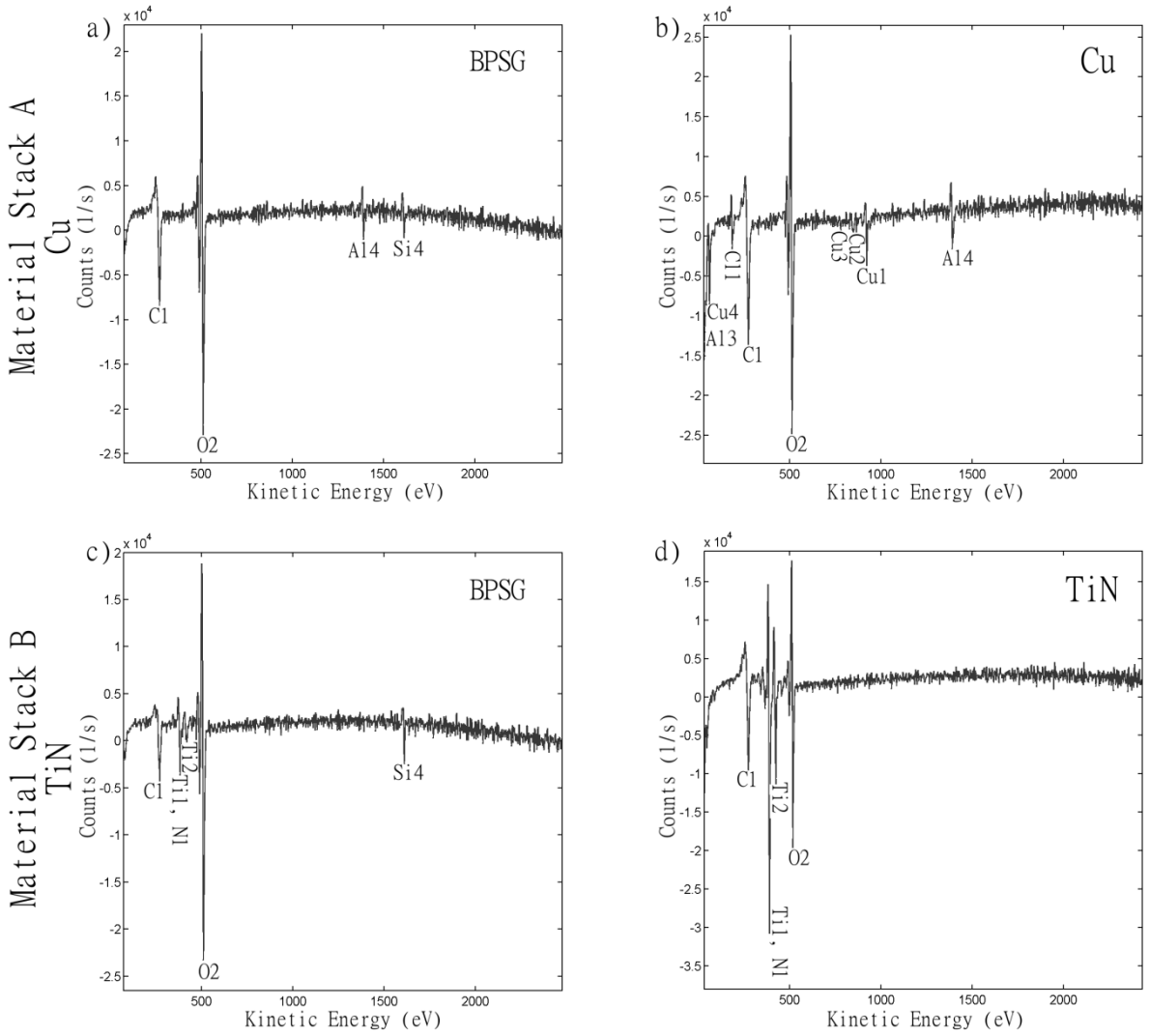

Figure 3 *AES spectra of the 4-point-bending fracture surfaces of Material Stacks A ((a) and (b)) and B ((c) and (d)). The spectra show that for the investigated samples the failing interface is the one between Cu (Material Stack A) or TiN (Material Stack B) and BPSG. In the AES spectra in (a) and (b), Al is found on both fracture surfaces. This occurs because of Al diffusion through the Cu layer into the BPSG layer. In spectra (c) and (d) the fracture surfaces of Material Stack B are depicted. In image (c), the BPSG fracture surface, TiN residues are detected.*

The Al found at the interface of Material Stack A led to a more detailed investigation of the Cu and AlSiCu layer using EDX scanning transmission electron microscopy (STEM) measurements. It was possible to show by EDX that some Al from the top AlSiCu layer diffused through the Cu film to the interface (see Figure 4b). Most likely the Al diffused during the final 400 °C anneal. In Figure 4a the presence of pores at the interface between the metallic film and BPSG of Material Stack A was also obxreved. Additionally it can be seen that there is a contrast difference between the left side (brighter region) and the right side (darker region) of the Cu+AlSiCu layer. Since Figure 4a is a high angle annular darkfield (HAADF) image, the main contrast difference is due to the difference in atomic number. This means that heavier elements appear brighter and lighter elements appear darker. Taking that

into account, the region of the metallic film next to the BPSG layer must be Cu rich, while the top part must be Al rich. This can also be seen in the line scan profile (Figure 4b), where Cu signal loses intensity going further to the right side of the layer. Another interesting feature visible in the HAADF image are the dark spots in the Al rich side of the layer, which corresponds to Si rich particles forming in the AlSiCu layer. These findings are further supported by the EDX map presented in Figure 4c. There it can be seen that an Al (green) enrichment is found on the top part of the metallic films and a Cu (blue) rich region at the lower part of the film adjacent to the BPSG diffusion barrier. In addition, the Si (red) particles are embedded in the AlSiCu layer are resolved in the EDX map.

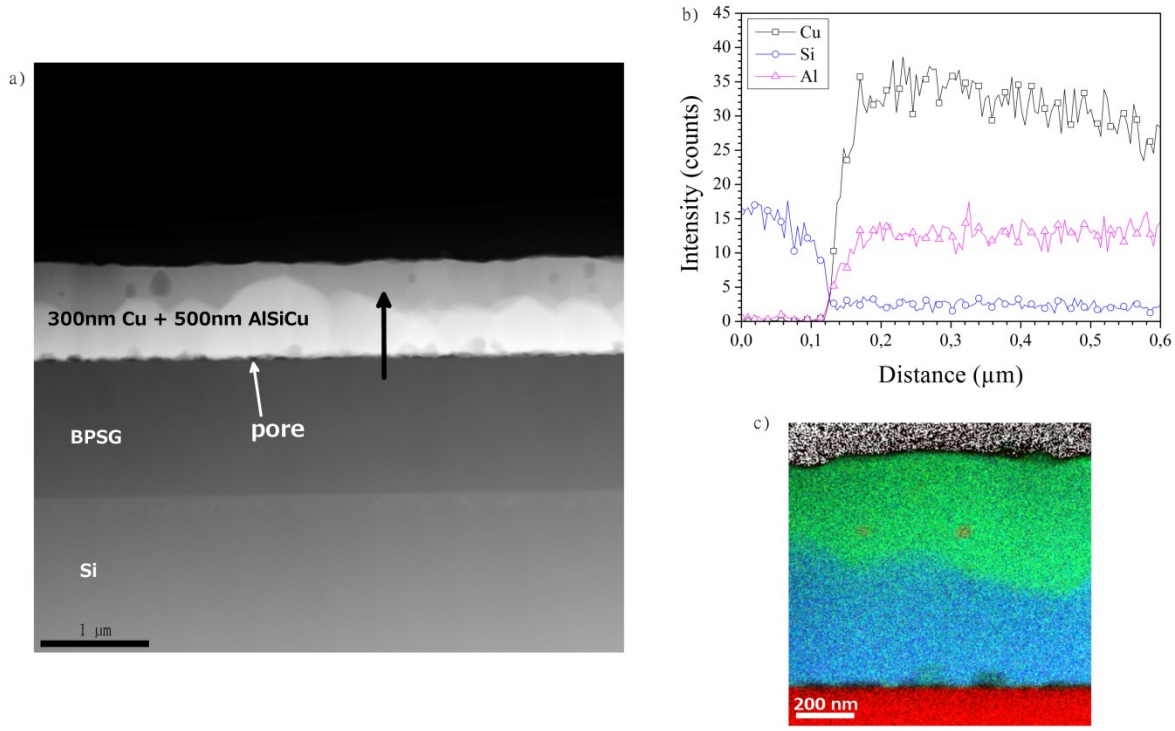

Figure 4 *HAADF images for Material Stack A (a). Small pores (white arrow in (a)) are resolved at the interface between BPSG and the metal layer. The contrast difference indicates Cu rich (bright) and Al rich (dark) regions in the nominally 300 nm thick Cu/ 500 nm thick AlSiCu layers. (b) concentration profiles for Cu, Al and Si were revealed by EDX line scans (see black arrow in (a)). The line scan profile of Material Stack A, resolves Al diffusion through the Cu layer. In addition, it can be seen that the Cu signal intensity decreases with distance from the interface. This is supported by the EDX map of the Cu+AlSiCu layer in (c). In (c) green represents Al, blue Cu and red Si. Note that some Si particles are found in the AlSiCu side of the layer. The Si precipitates are also resolved in the HAADF image by their scattering contrast.*

Discussion

The main goal of the investigation is to learn from in-situ fracture experiments how a crack initiates and propagates in a multilayer structure. In addition, an explanation shall be found why a certain interface is failing in a system consisting of several films. However, before

discussing this issue we have to discuss the interdiffusion of Al and Cu and its impact on the energy release rate values which we obtained.

The evaluated interface adhesion for Material Stack A (Cu/BPSG interface), (3.7±0.3) J/m^2, does correspond to the literature value found for similar material systems. Volinsky et al. [3] report a value of 4.3 J/m^2 for the work of adhesion of an Al-Cu layer on a SiO_2 layer. Another study by Kriese et al. [21] found, for a Cu/SiO_2 interface with a 400 nm thick Cu layer, an interface energy release rate of about 4 J/m^2 [21]. These results are in agreement with the one we found for our Al-alloyed Cu/BPSG interface (3.7±0.3) J/m^2 which consisted of an 800 nm thick intermixed Cu-AlSiCu film. It further indicates that the diffused Al does not to have a significant influence on the interface energy release rate adhesion of Cu on BPSG. For Material Stack B, the TiN system, the determined value for the interface energy release rate of 8.4 J/m^2 coincides well with a reported literature value of about 8 J/m^2 [14].

The in-situ SEM 4-point-bending experiments for Material Stack A showed that the crack kinked onto the Cu/BPSG interface (Figure 2a), which is confirmed for the ex-situ experiments by using AES analysis. For Material Stack B it is depicted in Figure 2b, that the crack does not kink onto the TiN/BPSG interface, but rather extends completely through the layer system to the AlSiCu/epoxy interface and arrests at that interface. The failure of this interface could not be resolved because the applied load in the in-situ SEM 4-point-bending experiments was not sufficiently high to fracture this interface. However, the optical inspection of the fracture surfaces, i.e. of ex-situ and in-situ 4-point-bending tests under the optical microscope, revealed fracture along the AlSiCu/epoxy interface.

The comparison of samples from the ex-situ experiments, which can be used to evaluate an interface energy release rate for the interface of interest for each material system, showed that the number is much higher for Material Stack A (15 samples) than for Material Stack B (1 sample). An explanation for this behaviour is based on the theoretical findings of He and Hutchinson [25]. They found for a bi-material layer system, that a crack chooses to kink onto the interface, if the interface energy release rate is about ¼ or less of the energy necessary to fracture the adjacent layer. The factor of about ¼ can be applied when it is assumed that there is no elastic mismatch between the two material layers. In principle this can be assumed in the case of 4-point-bending with the sample setup used in our investigations. The elastic mismatch between the thin films can be neglected because they are confined between two thick Si substrates which provide the predominant elastic properties of the sample. If the interfacial energy release rate for the interface of interest from the 4-point-bending experiment is compared to the values for the fracture energy of the metallization layer, it

should be possible to determine if the interface of interest is failing during the experiment. Literature values for the fracture energy of a TiN film several µm thick are about 20 J/m^2 [23,24] and for UFG Cu 7.6 kJ/m^2 [22]. UFG Cu was chosen because the grain size of about 340 nm [22] corresponds to our layer thickness of 300 nm. If these literature values are compared to the calculated interface energy release rates from the 4-point-bending experiments it becomes obvious that for TiN, with 8.4 J/m^2 interfacial energy release rate and fracture energy of about 20 J/m^2, the ratio of ¼ is not fulfilled. So the crack will prefer to fracture the TiN layer and run along another interface which fulfils the ¼ criterion. For Material Stack A, the Cu layer, it can be seen that the interfacial energy release rate determined using the 4-point-bending experiment (3.5 J/m^2) is much less than ¼ of the fracture energy of UFG Cu with 7.6 kJ/m^2 [22]. Hence, it is more probable for Material Stack A to fail along the Cu/BPSG interface. This explains why for Material Stack A the sample output is significantly higher than for Material Stack B and it is possible to describe the failing of different interfaces, as observed for some of the 4-point-bending samples of Material Stack B. The TiN/BPSG interface does not fulfil the criterion for failure along the interface, as mentioned earlier, but many samples tend to fail along the AlSiCu/epoxy interface. This suggests that this interface fulfils the ¼ criterion and it is more probable for the crack to extend along the AlSiCu/epoxy interface. The failure of the TiN/BPSG interface can be explained as follows. There is the possibility of a flaw at the interface. This flaw gives the crack the opportunity to kink onto the interface. Once there, the energy necessary to fracture along the TiN/BPSG interface is lower than the energy to fracture along the AlSiCu/epoxy interface. So the crack stayed at the interface and extended along it. These findings also conclude that it does matter on which side the pre-notch is introduced. In our sample setup the pre-notch is made on the Si wafers with the material layers on them. If the pre-notch would be introduced on the opposite side of the sample, the pure Si counterpart, it is possible that a different interface would fail than the one observed in our experiments. The reason for that is that the crack could hit an interface which fulfils the ¼ criterion before it reaches the interface of interest. In this case it is more likely for the crack to grow along the first interface. Taking these arguments into account it can be concluded that the hypotheses regarding the fracture assumptions are correct and the criterion by He and Hutchinson [25] can be employed for 4-point-bending tests of multilayer structures. In addition, the in-situ measurements provide the possibility to identify the failing interface during the course of the experiment making time consuming post-mortem investigation methods of the fracture surfaces to a large extend unnecessary.

Conclusion

In this study it was possible to show that in-situ 4-point-bending experiments in the SEM allow to determine the failing interface in multi-layered samples with several interfaces between materials without using additional methods. Furthermore, it could be demonstrated that in-situ experiments provide information on the selection of the crack path, thus permitting to judge if a valid interface energy release rate can be calculated. The in-situ experiments indicated that the theoretical findings by He and Hutchinson [25] for the interface failure in a bi-material system without elastic mismatch of the two materials can be employed on 4-point-bending experiments of multilayer thin film structures constrained between two thick Si substrates.

Acknowledgements

B.V. would like to thank R. Pippan for the discussions and T. Detzel and J. Fugger of Infineon Technologies Austria AG for their support. Part of this work was jointly funded by the Austrian Research Promotion Agency (FFG, Project No. 831163) and the Carinthian Economic Promotion Fund (KWF, contract KWF-1521|22741|34186).

References

[1] S. Varchenya, A. Simanovskis, S. Stolyarova, Thin Solid Films 164 (1988) 147.
[2] A. Kinbara, S. Baba, A. Kikuchi, T. Kajiwara, K. Watanabe, Thin Solid Films 171 (1989) 93.
[3] A.A. Volinsky, N.R. Moody, W.W. Gerberich, Acta Mater. 50 (2002) 441.
[4] D.B. Marshall, A.G. Evans, J. Appl. Phys. 56 (1984) 2632.
[5] M.D. Kriese, W.W. Gerberich, N.R. Moody, J. Mater. Res. 14 (1999) 3007.
[6] M.D. Kriese, W.W. Gerberich, N.R. Moody, J. Mater. Res. 14 (1999) 3019.
[7] M.J. Cordill, N.R. Moody, D.F. Bahr, J. Mater. Res. 19 (2004) 1818.
[8] M.J. Cordill, N.R. Moody, D.F. Bahr, Acta Mater. 53 (2005) 2555.
[9] E. Barthel, O. Kerjan, P. Nael, N. Nadaud, Thin Solid Films 473 (2005) 272.
[10] H. Hirakata, Y. Takahashi, D. Truong, T. Kitamura, Int. J. Fract. 145 (2007) 261.
[11] K. Matoy, T. Detzel, M. Müller, C. Motz, G. Dehm, Surf. Coat. Technol. 204 (2009) 878.
[12] J. Schaufler, C. Schmid, K. Durst, M. Göken, Thin Solid Films 522 (2012) 480.
[13] P.G. Charalambides, J. Lund, A.G. Evans, R.M. McMeeking, J. Appl. Mech. Trans. ASME 56 (1989) 77.
[14] Q. Ma, H. Fujimoto, P. Flinn, V. Jain, F. Adibi-Rizi, F. Moghadam, R.H. Dauskardt, in:, Mater. Res. Soc. Symp. - Proc., 1995.
[15] R.H. Dauskardt, M. Lane, Q. Ma, N. Krishna, Eng. Fract. Mech. 61 (1998) 141.
[16] Q. Ma, J. Bumgarner, H. Fujimoto, M. Lane, R.H. Dauskardt, in:, Mater. Res. Soc. Symp. - Proc., 1997, pp. 3–14.
[17] M. Lane, R.H. Dauskardt, N. Krishna, I. Hashim, J. Mater. Res. 15 (2000) 203.
[18] Z. Cui, G. Dixit, L. Xia, A. Demos, B.H. Kim, D. Witty, H. M'Saad, R.H. Dauskardt, in:, AIP Conf. Proc., 2005, pp. 507–511.
[19] R. Shaviv, S. Roham, P. Woytowitz, Microelectron. Eng. 82 (2005) 99.
[20] R.P. Birringer, P.J. Chidester, R.H. Dauskardt, Eng. Fract. Mech. 78 (2011) 2390.
[21] M.D. Kriese, N.R. Moody, W.W. Gerberich, Acta Mater. 46 (1998) 6623.
[22] A. Hohenwarter, R. Pippan, Mater. Sci. Eng. A 540 (2012) 89.
[23] S. Kamiya, H. Nagasawa, K. Yamanobe, M. Saka, Thin Solid Films 473 (2005) 123.
[24] S. Massl, W. Thomma, J. Keckes, R. Pippan, Acta Mater. 57 (2009) 1768.
[25] M.-Y. He, J.W. Hutchinson, Int. J. Solids Struct. 25 (1989) 1053.
[26] M.-Y. He, J.W. Hutchinson, J. Appl. Mech. Trans. ASME 56 (1989) 270.
[27] Z. Suo, J.W. Hutchinson, Int. J. Fract. 43 (1990) 1.
[28] L. Banks-Sills, D. Ashkenazi, Int. J. Fract. 103 (2000) 177.
[29] Z. Suo, J.W. Hutchinson, Mater. Sci. Eng. A 107 (1989) 135.
[30] B. Völker, W. Heinz, K. Matoy, R. Roth, J.M. Batke, T. Schöberl, C. Scheu, G. Dehm, Philos. Mag. (2014) DOI: 10.1080/14786435.2014.913108.
[31] J.J. Wortman, R.A. Evans, J. Appl. Phys. 36 (1965) 153.

Publication 4

In preparation

TEM submicron-sized bending beam fracture experiments of the interface between metal and dielectric.

B. Völker[1,2], W. Heinz[1], K. Matoy[3], R. Roth[3], J.M. Batke[4], M.J. Cordill[5] and G. Dehm[6]

[1] KAI - Kompetenzzentrum Automobil- und Industrieelektronik GmbH, Technologiepark Villach, Europastrasse 8, 9524 Villach, Austria

[2] Department Materials Physics, University of Leoben, 8700 Leoben, Austria

[3] Infineon Technologies AG, 9500 Villach, Austria

[4] Infineon Technologies AG, 93049 Regensburg, Germany

[5] Erich Schmid Institute of Materials Science, Austrian Academy of Sciences, Jahnstrasse 12, 8700 Leoben, Austria

[6] Max-Planck-Institut für Eisenforschung GmbH, 40237 Düsseldorf, Germany

Abstract

In this study a miniaturized in-situ TEM bending beam approach is investigated. It should be determined if it is a feasible method to determine an interface fracture energy, which is comparable to other methods. The interfaces under investigation are Cu/borophosphosilicate glass (BPSG) and W(20at%Ti)/BPSG as examples for a weak and a strong interface, respectively. It was possible with the in-situ experiments to evaluate an interface fracture energy for Cu/BPSG. Additionally, it could be shown that the evaluated fracture energy determined from the in-situ TEM bending beams gives a meaningful result. The TEM imposes challenges which can complicate the determination of an interface energy release rate are discussed. An example where the TEM approach failed is the W(20at%Ti)/BPSG no interface as no fracture occurred. Thus it is concluded, that the in-situ TEM bending beam method is useful for weak interfaces but for strongly adhering interfaces it is improperly. The reason for this will be discussed.

Introduction

Much effort has been put towards testing samples in the µm-scale in the last years. This enables the possibility to mechanically characterize small volumes of material from which it is not possible to prepare macroscopic samples. Furthermore, this opens a route to study how the mechanical properties of bulk material changes with size [1–12]. Recently, mechanical testing of interfaces at small length scales is gaining more and more interest [13–16]. Mechanically robust interfaces are increasingly important in every days applications, especially in micro-/nanoelectronics devices and sensors. As a consequence it is necessary to develop miniaturized testing methods for interfaces and novel preparation methods to be able to create the corresponding samples from small material volumes.

One such novel approach to characterize an interface, is the in-situ bending beam approach in the SEM utilized by Matoy et al. [14]. They tested the interfaces between W/SiO_X, $W(Ti)/SiO_X$ and Cu/SiO_X. In their investigation they revealed a fracture energy for the different interfaces of 2.86 J/m^2 for W/SiO_X, 4.8 J/m^2 for $W(Ti)/SiO_X$ and 0.65 J/m^2 for Cu/SiO_X. Furthermore, they could show that their results coincided with simulations and that their samples behave linear elastic. In these results it can be clearly seen that the Cu/SiO_X interface is significantly weaker than the other two interfaces.

Another study utilizing this SEM approach is reported by Schaufler et al. [15]. In their study the adhesion of amorphous carbon layers on a steel substrate was investigated.

Another possibility to do µm-scale testing of interfaces is the method proposed by Kamiya et al. [17]. Their method is based on scratch testing. This study revealed agreement between the micro-scale scratch test results and the 4-point-bending (4PB) data for a Cu/SiCN interface.

To get even smaller than the micro-bending beams used in the aforementioned SEM studies the approach suggested by Hirakata et al. [13] can be used. They described an in-situ transmission electron microscope (TEM) submicron-sized bending beam approach to evaluate crack initiation at the interface between Cu/Si. This method was extended by Sumigawa et al. [18] to study the fatigue behaviour of the same interface. Their investigation revealed plasticity in the Cu film and that the sample fractures due to higher cumulative plastic strain in the Cu layer under cyclic loading than under monotonic loading. Another study which employed this TEM approach is the one by Yan et al. [16], who investigated the environmental effects on the interface fatigue strength of the interface between Cu/Si. Samples that were treated in a special environmental chamber before testing showed a significantly lower failure stress for the interface than the ones without the treatment. The aforementioned studies used TEM in-situ submicron-sized bending beams.

All these investigations show that obviously bending beams are the favoured method for small scale mechanical testing of interfaces. The advantage of getting smaller and smaller, down to the submicron-sized bending beam samples used in the TEM, is that the interfaces can be tested closer to their size in semiconductor devices. In the above mentioned studies the dimensions of the bending beams had a thickness about 300 nm in electron beam direction and a width of about 200-300 nm perpendicular to the electron beam direction. However, so far no notch was introduced in the in-situ TEM samples and a direct comparison with other fracture tests of identical intrfaces is missing.

In this study the in-situ TEM submicron-sized bending beam approach, as suggested by Hirakata et al. [13], was employed to test a Cu/BPSG interface and determine an interface energy release rate for a sample with a pre-notch at the interface. The obtained results from the submicron-sized bending beams are compared to 4PB experiments, based on the method of Ma et al. [19]. The comparison of these two methods reveals if the in-situ TEM submicron-sized bending beam approach can be compared to the results of the macroscopic 4PB experiments. Additionally, certain limitations and restrictions of the in-situ submicron-sized bending beam method shall be disclosed.

Experimental Details

The sample production of the 4-point-bending beams was based on the one of Shaviv et al. [20] and follows the procedure as outlined in an earlier investigation [21]. As base material a 725 µm thick Si (100) wafer was used on which a 1.5 µm thick borophosphosilicate glass (BPSG) layer was deposited using plasma enhanced chemical vapour deposition (PECVD). After the BPSG layer was laid down the wafers were annealed at around 900 °C to densify the BPSG layer. In a next step the 300 nm Cu for Material Stack 1 and 2, and the 300 nm thick W(20at%Ti) layer for Material Stack 3, were deposited using magnetron sputtering. After the application of the 300 nm thick metallization layers different sample preparation processes were continued for Materials Stack 1 to 3. For Material Stack 1 the wafers were annealed at 400 °C and afterwards a 500 nm thick AlSiCu layer was laid down. To prepare the 4PB samples the wafer of Material Stack 1 were cut into the 40 mm long and a 7 mm wide rectangular pieces by a wafer saw. The next step was to introduce a pre-notch with 500 µm depth and 36 µm width into the Si side of the wafer. The rectangular pieces with the notch were then glued to a bare Si (100) counterpart with the same geometry, except that it had no pre-notch. The two pieces were joined used an epoxy (EPO-TEK 375). After curing the epoxy

the edges of the sample were ground and polished to remove epoxy residues and scratches from dicing.

For Material Stacks 2 and 3 the metallization layers, Cu and W(20at%Ti), were buried under a 2.5 µm thick SiO_X layer grown by PECVD. Finally, a 400 °C anneal was performed in an inert gas atmosphere. A detailed description of the Material Stacks 1 to 3 and the corresponding experiments for each system are summarized in Table 1.

Table 1 *Investigated material stacks and the experiments performed on each material system. 4PB abbreviates 4-point-bending and in-situ TEM stands for the in-situ TEM submicron-sized bending beam experiments.*

Material Stack	Layer structure	Investigations
1	Si 725µm / BPSG 1.5µm / Cu 300nm / AlSiCu 500nm	4PB
2	Si 725µm / BPSG 1.5µm / Cu 300nm / SiO_X 2.5µm	in-situ TEM
3	Si 725µm / BPSG 1.5µm / W(20at%Ti) 300nm / SiO_X 2.5µm	in-situ TEM

For Material Stacks 2 and 3 the wafers were diced in 10 mm x 7 mm pieces using a wafer saw. The pieces were structured in ~20 µm wide ~50 µm long lamellas by employing an Ar-ion cross section polisher (E-3500, Hitachi). From these lamellas, lift-out TEM samples were prepared with the focused ion beam (FIB). The lift-out lamellas were fixed on a TEM grid and the geometry of a miniaturized bending beam was milled. The geometry and dimensions of such a beam are depicted in Figure 1. The thickness of the beam is about 100 nm to obtain electron transparency in the TEM; the beam height is approximately 200 nm and the beam length 1500 nm. Since the thickness and height of the bending beam, and thus the region of interest, are, ≤200 nm we use the term submicron-sized bending beam. The pre-notch at the metal/BPSG interface, with a radius of about 10 nm, was introduced with a focused electron beam in the TEM. This allowed for a precise positioning of the electron beam.

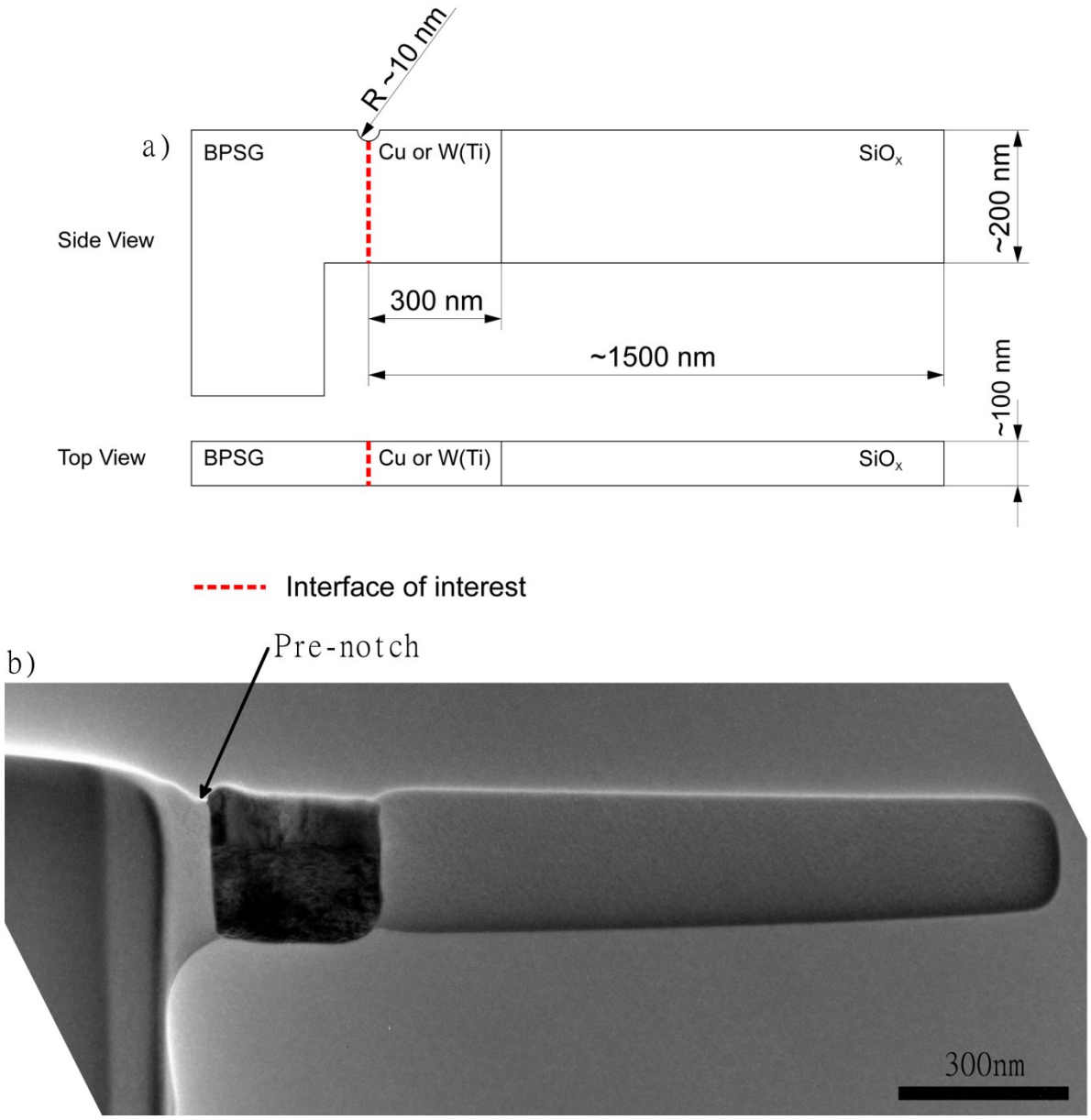

Figure 1 *(a) Sketch of the geometry and approximate measurements of an in-situ TEM micro-bending beam. The dashed line marks the interface of interest. (b) TEM image of a bending beam of Material Stack 3 where the pre-notch, which is prepared with a focused electron beam, is indicated.*

4PB testing of Material Stack 1 was done on a bending module of Kammrath & Weiss. The loading rate for these experiments was 0.1 µm/s. For the loading pins the distance between the two inner pins was 20 mm and the one between the two outer pins 30 mm. The evaluation of the experiment was done employing the equation for the interface energy release rate G_i according to Ma et al. [19]:

$$G_i = \frac{21(1-\nu^2)P^2l^2}{16Eb^2h^3}, \qquad \textit{(Eq. 1)}$$

where b=7 mm is the width of the 4PB sample, l=5 mm the distance between inner and outer loading pins , P the plateau load from the load displacement curve (see Figure 2), during which the crack extends along the interface, E=130 GPa the Young's modulus for Si (100) [22] and ν=0.28 the Poison's ratio for Si (100) [22]. The error given in the 4-point-bending results represents the standard deviation of the measurements. To determine the failing interface of Material Stack 1 Auger electron spectroscopy (AES) investigations of the fracture surfaces were performed on a PHI Scanning Auger Nanoprobe at an acceleration voltage of 5 kV.

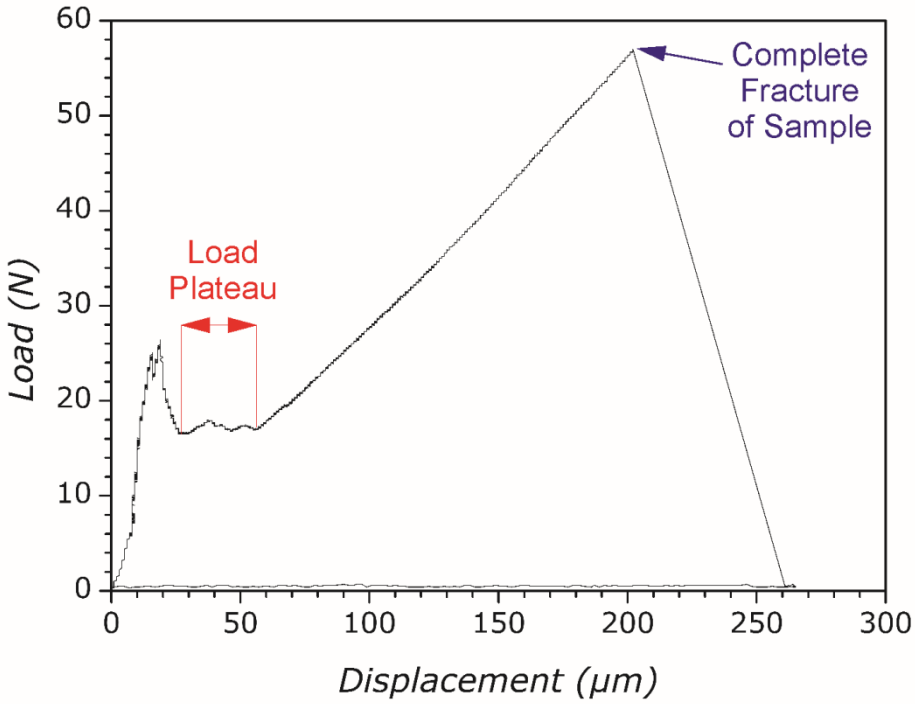

Figure 2 *Load-Displacement curve of a macroscopic 4-point-bending experiment of Material Stack 1 with a load plateau, which indicates stable crack growth along the interface and hence, can be used to evaluate the interface energy release rate from Equation 2 according to Ma et al. [19].*

The submicron-sized in-situ TEM bending beam experiments were conducted in a Jeol 2100F image-side C_S-corrected TEM utilizing a Hysitron Pico-Indenter, PI-95, with a wedge shaped indenter tip. The chosen loading scheme was displacement controlled and the displacement was increased from 50 nm up to 400nm. Duration of the loading segment was set to 20 s for each displacement. After fracture of the interface of interest the submicron-sized bending beams were evaluated according to Matoy et al. [14]. They used the evaluation scheme of a half circular notch in a semi-infinite body [23]. In this case the interface energy release rate is calculated by:

$$G = K^2/\bar{E} \qquad (Eq.\ 2)$$

K is the stress intensity factor for a semi-infinite plate with half circular notch [23], according to Equation 4, and the Young's modulus $\bar{E}$ considers the elasticity of the two adjacent materials forming the interface, with:

$$\frac{1}{\bar{E}} = \frac{1}{2}\left(\frac{1}{E_{Cu}} + \frac{1}{E_{BPSG}}\right) \qquad (Eq.\ 3)$$

according to Hutchinson and Suo [24]. In the present case E_{Cu}≈117 GPa is the Young's modulus of polycrystalline Cu [25] and E_{BPSG}≈70 GPa for BPSG [26–28]. The fracture toughness is calculated according to [23]

$$K = 1.12\sigma\sqrt{a\pi} \qquad (Eq.\ 4)$$

$$\sigma = \frac{M_b}{W_b} \qquad (Eq.\ 5)$$

$$M_b = F.l_i \qquad (Eq.6)$$

In this equation *1.12* represents the geometry factor and *a* the notch depth. σ denotes the bending stress, according to Equation 5, where M_b denotes the bending moment, which is calculated from load, *F*, times the lever, l_i between interface and loading point, see Equation 6. W_b is the section modulus for a rectangular area with the beam dimension.

Results and Discussion

The in-situ TEM bending-beam experiments were performed on Material Stacks 2 and 3. For Material Stack 2, the Cu system, 2 of the 3 tested samples failed along the interface. Still images taken during a successful TEM fracture experiment of Material Stack 2 are presented in Figure 3a-c. In Figure 3a the beginning is depicted where the indenter starts to load the specimen. Figure 3b reveals the crack initiation; in this image the crack initiates at the pre-notch and extends at the interface. This point corresponds to the onset of the load drop in the load-displacement curve of the in-situ TEM experiments. Finally, in Figure 3c the image recorded at the maximum displacement is presented, where the largest crack extension was

observed. Note that the sample did not fail catastrophically at crack initiation but shows a rather continuous crack growth.

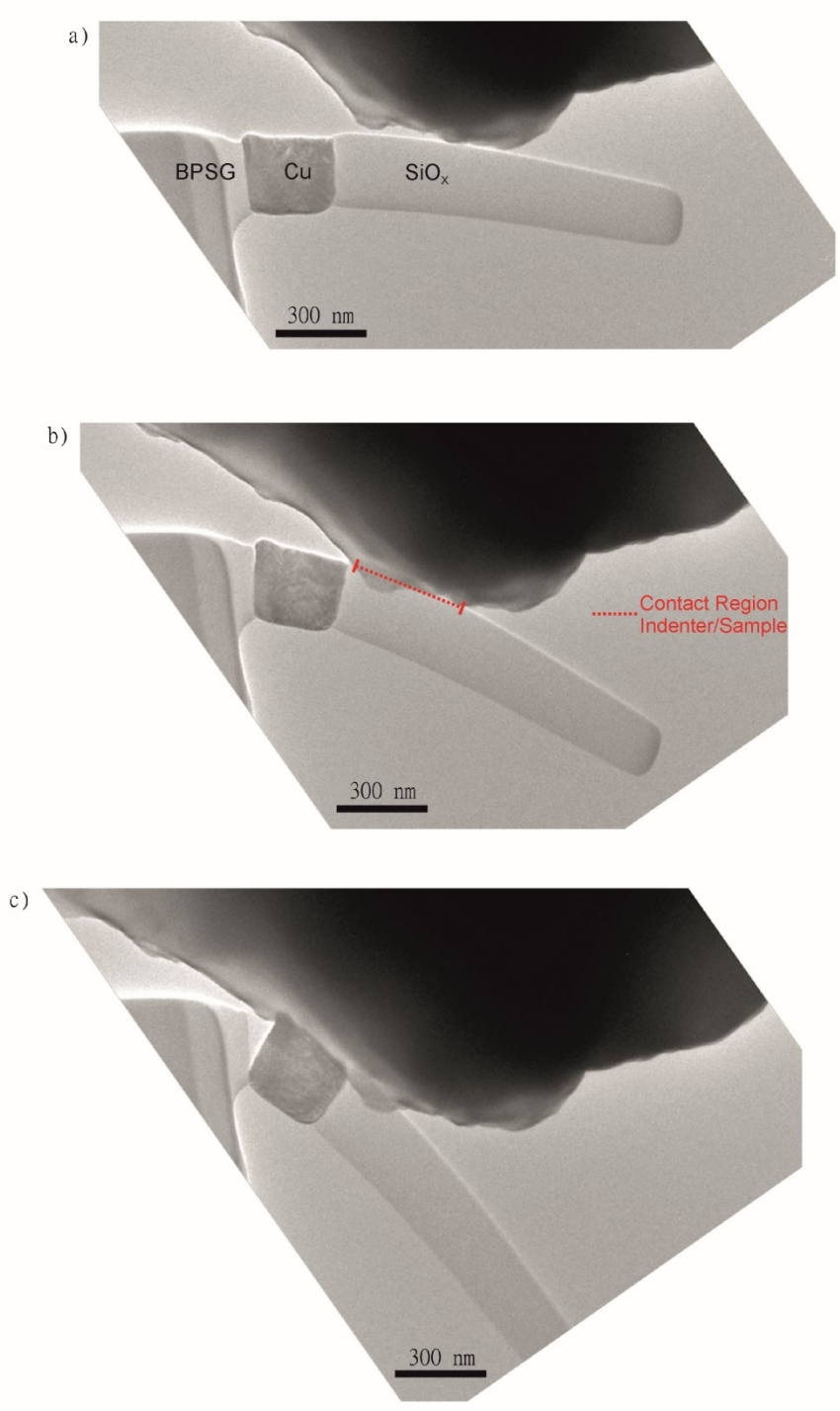

Figure 3 *The TEM images a-c depict different stages in the in-situ micro-bending beam experiment of sample B from Material Stack 2. (a) illustrates the initial state at the onset of loading. (b) shows the crack initiation and growth shortly after the load drop, seen in Figure 4. Furthermore, the contact region with the minimum and maximum lever length is depicted in (b). In image (c) the crack extension and beam deformation at the maximum displacement is shown.*

In Figure 4, the corresponding load-displacement curve for the Cu/BPSG sample presented in Figure 3 is provided (Sample B). Additionally, a second successful in-situ TEM measurement of Material Stack 2 (Cu/BPSG) is provided. The load used to evaluate the interface energy release rate is the maximum before the load drop. At that point the crack starts to initiate at the interface, which is shown in Figure 3b. The interface fracture energy was evaluated according to Matoy et al. [14]. The evaluated interface energy release rates of the two beams that could be evaluated for Material Stack 2 are (1.4±0.7) J/m^2 (Figure 4, sample A) and (1±0.5) J/m^2 (Figure 4, sample B) (Table 2). The given error of these results is caused by the corresponding minimum and maximum length of the contact region where the indenter loads the bending beam (see dotted line in Figure 3b). There were several difficulties in calculating the interface fracture energy. A major influence on the bending stress, and hence, on the interface fracture energy is the measurement of the lever between the point of loading and the interface. In the TEM images (Figure 3b) it is not clearly resolved where exactly the indenter touches the bending beam. In the 2 dimensional projection of the image it looks more like a region where the indenter is in contact with the beam, rather than a single contact point. It was assumed as an approximation that the point of loading is the centre of the line which seemed to be in contact. Furthermore, there is additional plastic deformation in the Cu layer and plastic deformation can also occur in the BPSG, according to the findings of Zheng et al. [29]. They found that electron beam irradiation can induce super-plasticity during mechanical deformation in silicate glass. The aforementioned plastic deformation causes an increase of the calculated interfacial fracture energy. Another parameter that influences the determined interface energy release rate is the mode mixity between mode I (opening of the crack flanks) and mode II (shearing of the crack flanks). With increasing mode II part the interface energy release rate increases [24]. The mode mixity also depends on the length of the lever. The shorter the lever the higher the contribution of mode II and hence, the higher the measured interface energy release rate. Taking these points into account the evaluated interface fracture energy of the in-situ submicron-sized bending beams can only be considered as an upper boundary for the theoretical fracture energy of the interface.

Table 2 *Results of the in-situ TEM bending beam experiments. For Material Stack 2 two beams fractured along the interface. The error given in the values for Material Stack 2 stems from the uncertainty in the lever length of the contact region (see Figure 3b).*

Material Stack	Tested Samples	Samples failing along the interface	Interface fracture energy (J/m^2)
2 Cu/BPSG	3	2	1±0.5 and 1.4±0.7
3 W(Ti)/BPSG	6	0	-

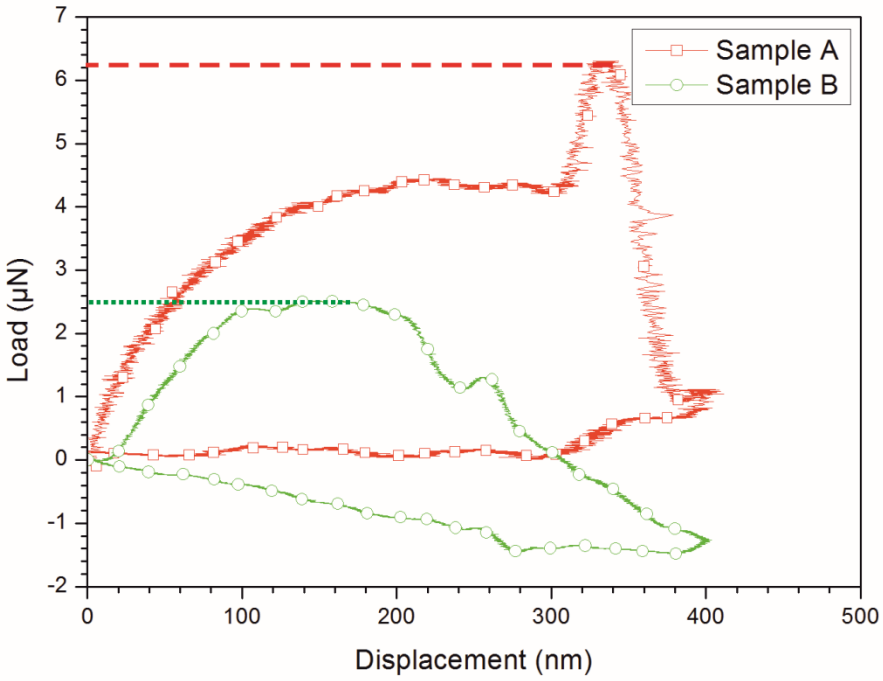

Figure 4 *In-situ TEM Load-displacement curves of Material Stack 2 for the samples which fractured along the interface. For both Cu/BPSG in-situ TEM samples interface fracture energies could be determined as the onset of crack opening was observed by in-situ TEM. The load used to determine the interface fracture energy is marked by the dashed line for sample A and the dotted line for sample B.*

For the macroscopic 4PB experiments 20 samples of Material Stack 1 were tested, while 7 could be used to evaluate an interface energy release rate. A load-displacement curve of a successful 4PB experiment is depicted in Figure 2. There the load plateau, which is used to calculate the interface energy release rate according to Equation 1, is clearly visible. The AES analysis of the two fracture surfaces of Material Stack 1 revealed that the failing interface is the one between Cu and BPSG. The evaluated interface energy release rate of (4.0±0.5) J/m^2 is higher than for our in-situ TEM experiment on Cu/BPSG, but agrees with the findings of Kriese et al. [30]. They found for a 400 nm thick Cu layer on SiO_2 an interface energy release rate of about 4 J/m^2.

The evaluated interface energy release rates of the in-situ TEM bending beams for Material Stack 2, which are (1.4±0.7) J/m^2 and (1±0.5) J/m^2, do not fit well with the results of the 4PB experiments (4±0.5) J/m^2. They seem to be in better agreement to the results of Matoy et al. [14], who found, utilizing a micro-bending beam approach, for a 50 nm thick Cu layer on SiO_X, an interface energy release rate of 0.65 J/m^2. The difference between the in-situ TEM submicron-sized bending beam results and the 4PB tests can be explained by the findings of Kriese et al. [30]. They revealed that the evaluated interface fracture energy is depends on the thickness of the Cu layer. The reason for that is that in a thicker Cu layer more plastic deformation can be accumulated than in a thinner one. Hence, a higher energy is necessary to deform the sample, which increases the evaluated interface energy release rate. Their result for a 400 nm thick Cu layer on SiO_2 is about 4 J/m^2 and this is in good agreement with the findings of the 4PB experiments of Material Stack 1, the 300 nm Cu film on BPSG, with (4.0±0.5) J/m^2. For a 200 nm thick Cu layer Kriese et al. [30] measured an interface fracture energy of about 2.5 J/m^2. This means that the in-situ TEM bending beams with their 100 nm thickness, should lie in between the results of Matoy et al. [14], 0.65 J/m^2 for 50 nm Cu on SiO_X, and Kriese et al. [30], 2.5 J/m^2 for 200 nm Cu on SiO_2. As mentioned before, the results for the bending beams are (1±0.5) J/m^2 and (1.4±0.7) J/m^2.

Since for the rather weak Cu/BPSG interface a quantitative in-situ TEM test is possible, we tried to fracture the interface W(Ti)/BPSG. For Material Stack 3, the W(Ti) system on BPSG, 6 samples were tested inside the TEM and none of them failed along the interface. These samples did only deform plastically and did not fracture at all. The explanation for that is probably that the interface of Material Stack 3 is too strong. This is backed by the findings of Matoy et al. [14]. They tested W(Ti) and Cu on SiO_X using a micro-bending beam approach. They found that W(Ti)/SiO_X has an interface strength of 4.8 J/m^2 which is more than 7 times higher than the Cu/SiO_X interface with 0.65 J/m^2. Although the value of 4.8 J/m^2 for W(Ti) on SiO_X does not appear to be extremely high, the interface energy release rate for W(Ti) on BPSG may even exceed this value. In an earlier 4PB study we observed an interface energy release rate about 6 J/m^2 for W(Ti) on annealed BPSG [31]; this is the same interface as used for the in-situ TEM testing. These findings conclude that the W(Ti)/BPSG is significantly stronger than the Cu/BPSG or Cu/SiO_X interface.

The results obtained in this study show that the in-situ TEM submicron-sized bending beam approach is a method which can be used to determine the fracture energy of interfaces. The advantages of this method are that large volumes of material are not necessary to prepare samples and that the interfaces can be tested close to the size they have in devices.

Furthermore, the crack path becomes directly visible and it can be resolved if, for example, the crack runs through the layer or along the interface. One disadvantage is that the approach seems to be only ideal for weak interfaces, like Cu/BPSG. For stronger interfaces, like W(Ti)/BPSG, it is not suitable. When the in-situ TEM submicron-sized bending beam approach is utilized on weak interfaces, the results are comparable to findings from other methods like 4PB or superlayer nanoindentation, if appropriate considerations are taken into account. In the future, the in-situ TEM fracture approach provides the possibility to get localized chemical information of the interface via EDX or EELS in the TEM, before and after the experiment. This enables a correlation linkage between chemical and mechanical results of an interface.

Conclusion

It was possible to show that the results which were obtained using the micro-bending beam approach are suitable, if compared to other interface testing methods, e.g. 4PB testing. Certain difficulties arise for the in-situ TEM bending beam technique because of additional influences on the determination of the fracture energy of the interface. Some of these parameters were listed and discussed, like plastic deformation in the metallization and the oxide, and the determination of the lever length. But, the results are encouraging and provide realistic fracture energy values. This shows that the in-situ TEM bending beam approach is a method that can be used for targeted mechanical investigation of interfaces.

Acknowledgements

B.V. wants to thank R. Pippan for the discussions and T. Detzel and J. Fugger of Infineon Technologies Austria AG for their support. Part of this work was jointly funded by the Austrian Research Promotion Agency (FFG, Project No. 831163) and the Carinthian Economic Promotion Fund (KWF, contract KWF-1521|22741|34186).

Literature

[1] M.D. Uchic, D.M. Dimiduk, J.N. Florando, W.D. Nix, Science 305 (2004) 986.
[2] C. Motz, T. Schöberl, R. Pippan, Acta Mater. 53 (2005) 4269.
[3] J.R. Greer, W.C. Oliver, W.D. Nix, Acta Mater. 53 (2005) 1821.
[4] C.A. Volkert, E.T. Lilleodden, D. Kramer, J. Weissmüller, Appl. Phys. Lett. 89 (2006) 061920.
[5] S.H. Oh, M. Legros, D. Kiener, P. Gruber, G. Dehm, Acta Mater. 55 (2007) 5558.
[6] D. Kiener, W. Grosinger, G. Dehm, R. Pippan, Acta Mater. 56 (2008) 580.
[7] G. Dehm, Prog. Mater. Sci. 54 (2009) 664.
[8] G. Richter, K. Hillerich, D.S. Gianola, R. Mönig, O. Kraft, C.A. Volkert, Nano Lett. 9 (2009) 3048.
[9] O. Kraft, P.A. Gruber, R. Mönig, D. Weygand, Annu. Rev. Mater. Res. 40 (2010) 293.
[10] E. Demir, D. Raabe, F. Roters, Acta Mater. 58 (2010) 1876.
[11] A.T. Jennings, J.R. Greer, Philos. Mag. 91 (2011) 1108.
[12] S. Wurster, C. Motz, R. Pippan, Philos. Mag. 92 (2012) 1803.
[13] H. Hirakata, Y. Takahashi, D. Truong, T. Kitamura, Int. J. Fract. 145 (2007) 261.
[14] K. Matoy, T. Detzel, M. Müller, C. Motz, G. Dehm, Surf. Coat. Technol. 204 (2009) 878.
[15] J. Schaufler, C. Schmid, K. Durst, M. Göken, Thin Solid Films 522 (2012) 480.
[16] Y. Yan, T. Sumigawa, T. Kitamura, Mater. Sci. Eng. A 556 (2012) 147.
[17] S. Kamiya, H. Shimomura, M. Omiya, T. Suzuki, J. Mater. Res. 25 (2010) 1917.
[18] T. Sumigawa, T. Murakami, T. Shishido, T. Kitamura, Mater. Sci. Eng. A 527 (2010) 6518.
[19] Q. Ma, H. Fujimoto, P. Flinn, V. Jain, F. Adibi-Rizi, F. Moghadam, R.H. Dauskardt, in:, Mater. Res. Soc. Symp. - Proc., 1995.
[20] R. Shaviv, S. Roham, P. Woytowitz, Microelectron. Eng. 82 (2005) 99.
[21] B. Völker, W. Heinz, K. Matoy, R. Roth, J.M. Batke, T. Schöberl, C. Scheu, G. Dehm, Philos. Mag. (2014) DOI: 10.1080/14786435.2014.913108.
[22] J.J. Wortman, R.A. Evans, J. Appl. Phys. 36 (1965) 153.
[23] H. Tada, P.C. Paris, G.R. Irwin, The Stress Analysis of Cracks Handbook, Third Edition, ASME, Three Park Avenue New York, NY 10016-5990, 2000.
[24] J. Hutchinson, Z. Suo, Adv. Appl. Mech. 29 (1992) 191.
[25] M. Li, S.J. Zinkle, in:, Compr. Nucl. Mater., 2012, pp. 667–690.
[26] S. Spinner, J. Am. Ceram. Soc. 37 (1954) 229.
[27] A. Makishima, J.D. Mackenzie, J. Non-Cryst. Solids 12 (1973) 35.
[28] S. Inaba, S. Fujino, K. Morinaga, J. Am. Ceram. Soc. 82 (1999) 3501.
[29] K. Zheng, C. Wang, Y.-Q. Cheng, Y. Yue, X. Han, Z. Zhang, Z. Shan, S.X. Mao, M. Ye, Y. Yin, E. Ma, Nat. Commun. 1 (2010) 24.
[30] M.D. Kriese, N.R. Moody, W.W. Gerberich, Acta Mater. 46 (1998) 6623.
[31] B. Völker, W. Heinz, K. Matoy, R. Roth, J.M. Batke, T. Schöberl, M.J. Cordill, G. Dehm, Thin Solid Films (submitted).

Appendix

A. 4-Point-Bending Sample Production

Starting point of this description are the cut and pre-notched wafer pieces. The geometry and dimensions of the pieces can be found in the Publications 1-4.

At first the cut wafer pieces have to be removed from the sawing foil. For a weak interface like Cu/BPSG, the samples have to be removed using toluene to remove the glue of the foil to prevent the metallization to peel off from the wafer. In contrast to that, if the interface is stronger, like in the W(Ti)/BPSG system, it is possible to remove the pieces mechanically from the foils without the use of toluene.

In the next step, the pre-notch has to be filled with a lacquer to prevent the epoxy, which is used to glue the sample (more of that later), of creeping into the pre-notch during curing of the epoxy. The lacquer used was Lacomit. After the lacquer was dried the surfaces which have to be glued together were cleaned with acetone and glued together. The counterpart which is glued on the pre-notched piece with the metallization on it was a piece of a pure Si wafer, which had the same size and no pre-notch. To glue the two pieces together the epoxy EPO-TEK 375 is used. It was cured in a vacuum furnace at about $1x10^{-5}$ mbar, at 100 °C for 8 hours. Next the samples were put in acetone for a few hours to remove the lacquer from the notch. At last the edges of the samples were grinded, for the ex-situ experiments the grinding was done manually and a 1200 grit paper was used. For the in-situ experiments the grinding and polishing of the samples was done automatically. At first sandpaper with a 320 grit and after that 800 grit was used. The polishing was done with a diamond paste in three steps starting with 9 µm, via 3 µm down to 1 µm diamond particle size. As a final step an OP-S solution was used to perform the last polishing step, to get a scratch free surface for the in-situ optical and SEM experiments.

B. 4-Point-Bending Results

The table below gives a complete list of all the investigated material systems, using the 4-point-bend method, and their results.

Layer Structure	Number of tested samples	Number of evaluable samples	Batch	Notch depth (µm)	Interface energy release rate ± standard deviation (J/m^2)
725µm Si/1.5µm as-deposited BPSG/10nm Ti/Airbreak/200nm W(20at%Ti)/500nm AlSiCu	16	4	ROTH	500	11.9±0.7
725µm Si/1.5µm as-deposited BPSG/10nm Ti/200nm W(20at%Ti)/500nm AlSiCu	7	0	ROTH	500	-
725µm Si/10nm Ti/Airbreak/200nm W(20at%Ti)/500nm AlSiCu	12	0	ROTH	500	-
725µm Si/1.5µm as-deposited BPSG/10nm Ti/200nm W(20at%Ti)/500nm AlSiCu	15	3	ROTH	500	11.7±0.4
725µm Si/1.5µm as-deposited BPSG/Ar-ion implantation/200nm W(20at%Ti)/500nm AlSiCu	20	4	ROTH	500	5
725µm Si/1.5µm as-deposited BPSG/200nm W(20at%Ti)/500nm AlSiCu	20	6	ROTH	500	4.9±0.2
725µm Si/1.5µm annealed BPSG/10nm Ti/300nm W(20at%Ti)/500nm AlSiCu	7	5	VE121618	500	4.9±0.5
725µm Si/1.5µm annealed BPSG/300nm W(20at%Ti)/500nm AlSiCu	8	2	VE121618	500	5
725µm Si/1.5µm annealed BPSG/300nm W(20at%Ti)/500nm Cu/500nm AlSiCu	6	0	VE121618	500	-

725µm Si/1.5µm annealed BPSG/Ar-ion implantation/300nm W(20at%Ti)/500nm Cu/500nm AlSiCu	10	0	VE121618	500	-
725µm Si/1.5µm annealed BPSG/10nm Ti/Airbreak/300nm W(20at%Ti)/500nm Cu/Cu plating NEXX (10µm Cu)	9	0	VE121618	500	-
725µm Si/1.5µm annealed BPSG/Ar-Implantation/300nm W(20at%Ti)/500nm Cu/Cu plating Nexx (10µm Cu)	6	0	VE121618	500	-
725µm Si/1.5µm annealed BPSG/10nm Ti/300nm W(20at%Ti)/500nm AlSiCu	17	12	VE204027	500	6.3±0.7
725µm Si/1.5µm annealed BPSG/10nm Ti/300nm W(20at%Ti)/500nm AlSiCu	20	16	VE204027	550	4.8±0.5
725µm Si/1.5µm annealed BPSG/10nm Ti/300nm W(20at%Ti)/500nm AlSiCu	20	14	VE204027	600	5.2±0.3
725µm Si/1.5µm annealed BPSG/10nm Ti/Airbreak/300nm W(20at%Ti)/500nm AlSiCu	20	10	VE204027	500	5±0.4
725µm Si/1.5µm annealed BPSG/10nm Ti/Airbreak/300nm W(20atTi)/500nm AlSiCu	15	9	VE204027	550	5.4±0.4
725µm Si/1.5µm annealed BPSG/300nm W(20at%Ti)/500nm AlSiCu	20	13	VE204027	500	5.9±0.3
725µm Si/1.5µm annealed BPSG/300nm W(20at%Ti)/500nm AlSiCu	15	10	VE204027	550	5.3±0.4
725µm Si/1,5µm annealed BPSG/Ar-ion implantation/300nm W(20at%Ti)/500nm AlSiCu	20	15	VE204027	500	5.2±0.4

725µm Si/1.5µm annealed BPSG/Ar-ion implantation/300nm Ti/500nm AlSiCu	20	3	VE233568	500	6.2±0.4
725µm Si/1.5µm annealed BPSG/Ar-ion implantation/300nm W(15at%Ti)/500nm AlSiCu	20	9	VE233568	500	6.1±0.6
725µm Si/1.5µm annealed BPSG/Ar-ion implantation/300nm W(20at%Ti)/500nm AlSiCu	20	2	VE233568	500	5.8
725µm Si/1.5µm annealed BPSG/Ar-ion implantation/300nm W(25at%Ti)/500nm AlSiCu	20	2	VE233568	500	6.3
725µm Si/1.5µm annealed BPSG/Ar-ion implantation/300nm Cu/500nm AlSiCu (with Al diffusion through Cu layer)	20	15	VE233568	500	3.7±0.3
725µm Si/1.5µm annealed BPSG/Ar-ion implantation/300nm Cu/500nm AlSiCu (without Al diffusion through Cu layer)	20	7	VE321098	500	4.0±0.5
725µm Si/1.5µm annealed BPSG/Ar-ion implantation/300nm TiN/500nm AlSiCu	45	1	VE233568	500	8.4
725µm Si/1.5µm annealed BPSG/Ar-ion implantation/300nm W/500nm AlSiCu (without final 400°C anneal)	20	8	VE307514	500	3.8±0.4
725µm Si/1.5µm annealed BPSG/Ar-ion implantation/300nm W/500nm AlSiCu	20	9	VE320678	500	3.1±0.5

C. 4-Point-Bending in Liquid N_2

To investigate the influence of an absence of plastic deformation on the interfacial adhesion of Cu on annealed borophpsphosilicate glass (BPSG) 4-point-bending (4PB) experiments in liquid N_2 were performed. In an earlier study by Kriese et al. [1] it could be shown that the interface energy release rate of Cu on SiO_2 is dependent on the thickness of the Cu layer. The reason for that is that in a thicker Cu layer more plastic deformation can be accommodated and hence, the measured interface energy release rate is higher. This leads to an increase in the calculated interface energy release rate. To see if it is possible to suppress the plastic deformation in Cu, 4-point-benidng (4PB) experiments on the Cu/BPSG system, in liquid N_2, were performed.

To be able to test at different temperatures the tests had to be performed on a Zwick universal testing machine and not on the usual Kammrath & Weiss bending module. Both experimental setups can be seen in Figure 1.

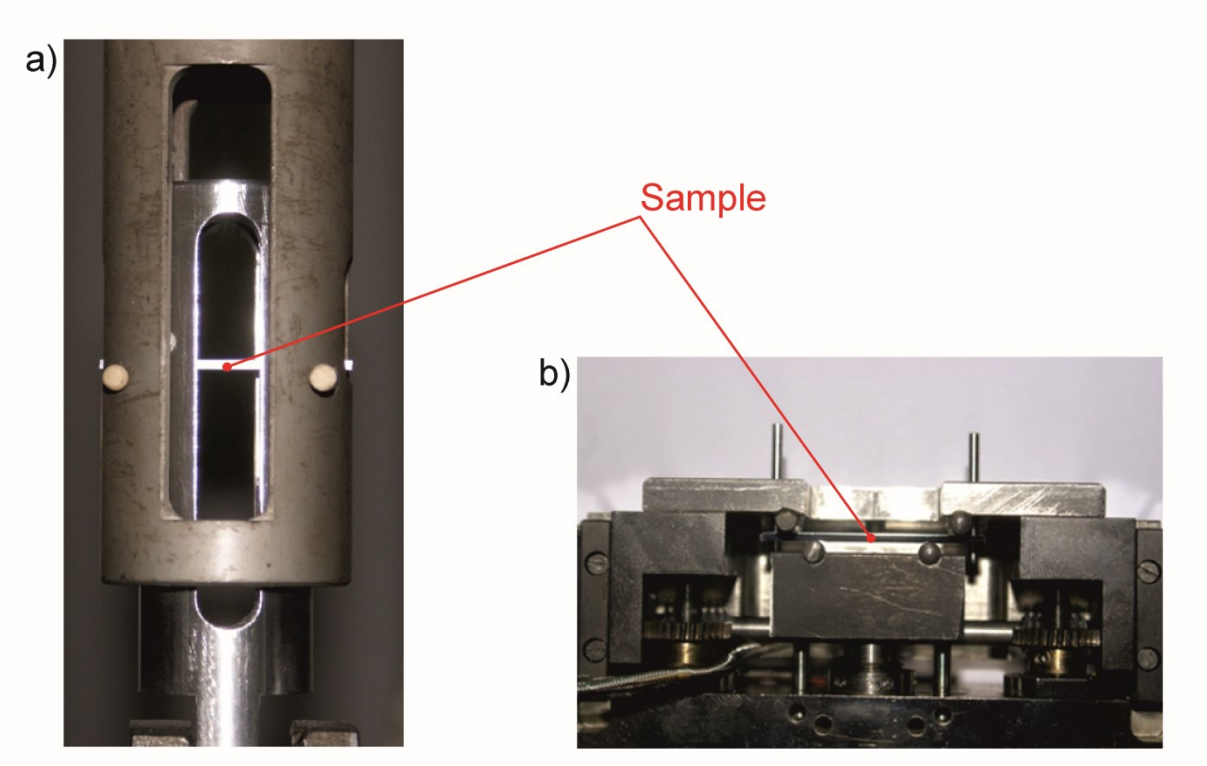

Figure 1 *Comparison of the two experimental setups for 4-point-bending. a) shows the experimental setup for the Zwick and b) depicts the Kammrath & Weiss bending module setup.*

To guaranty comparability of the Zwick experiments, with the measurements done on the Kammrath & Weiss bending module, room temperature tests were performed on the Zwick.

The latter gave similar interface energy release rates as the experiments on the Kammrath & Weiss, see Table 1.

Table 1 *The evaluated interface energy release rates for the experiments on different testing machines and at different temperatures, are given.*

	Interface energy release rate ± standard deviation (J/m^2)	
Temperature	Zwick	Kammrath & Weiss
Room temperature	4.6±0.5	4.0±0.5
Liquid N_2	not successful	not performed

After the room temperature experiments proved to be similar, the samples were tested in liquid N_2.

The liquid N_2 experiments were not successful. Hence, it could not be revealed if the testing at liquid N_2 had any effect on the interface energy release rate. Further investigation of this topic is necessary to get a representative result.

[1] M.D. Kriese, N.R. Moody, W.W. Gerberich, Acta Materialia 46 (1998) 6623.